RESISTANCE RISE IN ULTRATHIN
METALLIC WIRES AT LOW TEMPERATURES

By

Alice E. White

August 1982

Technical Report No. 18

Division of Applied Sciences

Harvard University   Cambridge, Massachusetts

AD A119594

DTIC FILE COPY

DTIC
SELECTED
SEP 2 7 1982
A

82 09 27 006

REPORT DOCUMENTATION PAGE	READ INSTRUCTIONS BEFORE COMPLETING FORM	
1. REPORT NUMBER Technical Report No. 18	2. GOVT ACCESSION NO. AD-A119 594	3. RECIPIENT'S CATALOG NUMBER
4. TITLE (and Subtitle) RESISTANCE RISE IN ULTRATHIN METALLIC WIRES AT LOW TEMPERATURES	5. TYPE OF REPORT & PERIOD COVERED Interim Report	
	6. PERFORMING ORG. REPORT NUMBER	
7. AUTHOR(s) Alice E. White	8. CONTRACT OR GRANT NUMBER(s) N00014-77-C-0085 NSF DMR79-04155 NSF DMR80-20247	
9. PERFORMING ORGANIZATION NAME AND ADDRESS Division of Applied Sciences Harvard University Cambridge, Mass. 02138	10. PROGRAM ELEMENT, PROJECT, TASK AREA & WORK UNIT NUMBERS	
11. CONTROLLING OFFICE NAME AND ADDRESS	12. REPORT DATE August 1982	
	13. NUMBER OF PAGES 164	
14. MONITORING AGENCY NAME & ADDRESS(if different from Controlling Office)	15. SECURITY CLASS. (of this report) Unclassified	
	15a. DECLASSIFICATION/DOWNGRADING SCHEDULE	

16. DISTRIBUTION STATEMENT (of this Report)

Reproduction in whole or in part is permitted for any purpose of the United States Government. Approved for public release; distribution unlimited.

17. DISTRIBUTION STATEMENT (of the abstract entered in Block 20, if different from Report)

18. SUPPLEMENTARY NOTES

19. KEY WORDS (Continue on reverse side if necessary and identify by block number)
Low Temperature Electrical Conduction in Metals
Electron-Electron Interactions
Electron Localization
Microstructure Fabrication

20. ABSTRACT (Continue on reverse side if necessary and identify by block number)
    We report new measurements of the low temperature resistance rise in ultrathin wires and films of copper, AuPd alloy, and nickel. The wires, which have cross-sectional dimensions as small as 220Å x 200Å, are fabricated using a versatile step-edge shadowing technique. The dimensions of the wires can be precisely determined by easily-controlled fabrication parameters such as thin film thickness and shadowing angle. In order to verify the dimensions and integrity of the wires, we have developed a convenient and reliable technique for thinning the substrate. This allows nondestructive examination of the structures by high resolution

20. ABSTRACT continued

transmission electron microscopy. We have used a similar technique to investigate grain sizes of thin metal films.

The theoretical models for the low temperature resistance rise in samples of reduced dimensionality are usually classed as based on one-electron "localization" or many-electron "interaction" effects. Our experimental results for copper, AuPd alloy, and nickel wires accurately confirm the proportionality to $T^{-1/2}$ predicted by the interaction model of Altshuler, Khmel'nitzkii, Larkin, and Lee. Moreover, we find that our results and the results of a careful reanalysis of the data already in the published literature give an absolute magnitude consistent within a factor of ~ 2 with the quantitative predictions of this model, using independently determined parameters. We therefore infer that interaction effects are at least as important as, and may dominate over, localization effects in all one-dimensional lithographically-produced samples reported to date.

Accession For

NTIS GRA&I

DTIC TAB

Unannounced

Justification

Distribution/

Availability Codes

and/or

Special

DTIC COPY INSPECTED 2

RESISTANCE RISE IN ULTRATHIN METALLIC WIRES
AT LOW TEMPERATURES

By

Alice E. White

Technical Report No. 18

August 1982

Division of Applied Sciences

Harvard University · Cambridge, Massachusetts

ABSTRACT

We report new measurements of the low temperature resistance rise in ultrathin wires and films of copper, AuPd alloy, and nickel. The wires, which have cross-sectional dimensions as small as 220Å x 200Å, are fabricated using a versatile step-edge shadowing technique. The dimensions of the wires can be precisely determined by easily-controlled fabrication parameters such as thin film thickness and shadowing angle. In order to verify the dimensions and integrity of the wires, we have developed a convenient and reliable technique for thinning the substrate. This allows nondestructive examination of the structures by high resolution transmission electron microscopy. We have used a similar technique to investigate grain sizes of thin metal films.

The theoretical models for the low temperature resistance rise in samples of reduced dimensionality are usually classed as based on one-electron "localization" or many-electron "interaction" effects. Our experimental results for copper, AuPd alloy, and nickel wires accurately confirm the proportionality to $T^{-1/2}$ predicted by the interaction model of Altshuler, Khmel'nitzkii, Larkin, and Lee. Moreover, we find that our results and the results of a careful reanalysis of the data already in the published literature give an absolute magnitude consistent within a factor of ~2 with the quantitative predictions of this model, using independently determined parameters. We therefore infer that interaction effects are at least as important as, and may dominate over, localization effects in all one-dimensional lithographically-produced samples reported to date.

TABLE OF CONTENTS

LIST OF FIGURES

LIST OF TABLES

1000 A

Frontpiece: Edge-on view of a high-period spinorewave surface relief structure that was relatively ion-etched into silica. The fuzzy appearance is due to a thin coating of carbon.

CHAPTER ONE: INTRODUCTION

In 1977, David Thouless sparked the interest of experimentalists by predicting that, under certain circumstances, localization of electrons would cause an effectively one-dimensional conductor to exhibit an increasing resistance at low temperatures (as opposed to the expected temperature-independent residual resistance). At absolute zero, the conditions for observation of this effect were that the length of the conductor be much greater than its cross-sectional dimension and that its resistance be greater than roughly $10,000\,\Omega$. For an ordinary #36 gauge copper wire 270km long, his theory indicated that the rising resistance would begin to be observable at $\sim 10^{-7}\,^{\circ}K$, well out of the reach of current cryogenic techniques. However, he suggested that, in a wire with cross-sectional dimensions of 500Å x 500Å and a length greater than $12\,\mu m$, the effect might be seen at about $1^{\circ}K$. Until recently, these dimensions were beyond the range of conventional fabrication techniques, but the revolution in submicrometer technology in the past few years has made the hundred angstrom size scale accessible. This is dramatically illustrated in Figs. 1.1, 1.2, and 1.3, which show, in successively more magnified views, the scale of some man-made submicrometer structures relative to a human hair, to the wavelength of visible light, and to a virus.

The theoretical understanding of the effect Thouless described has also progressed a great deal since his provocative paper. A more generalized scaling theory of localization was developed by Abrahams, Anderson, Licciardello, and Ramakrishnan in 1979 that contained
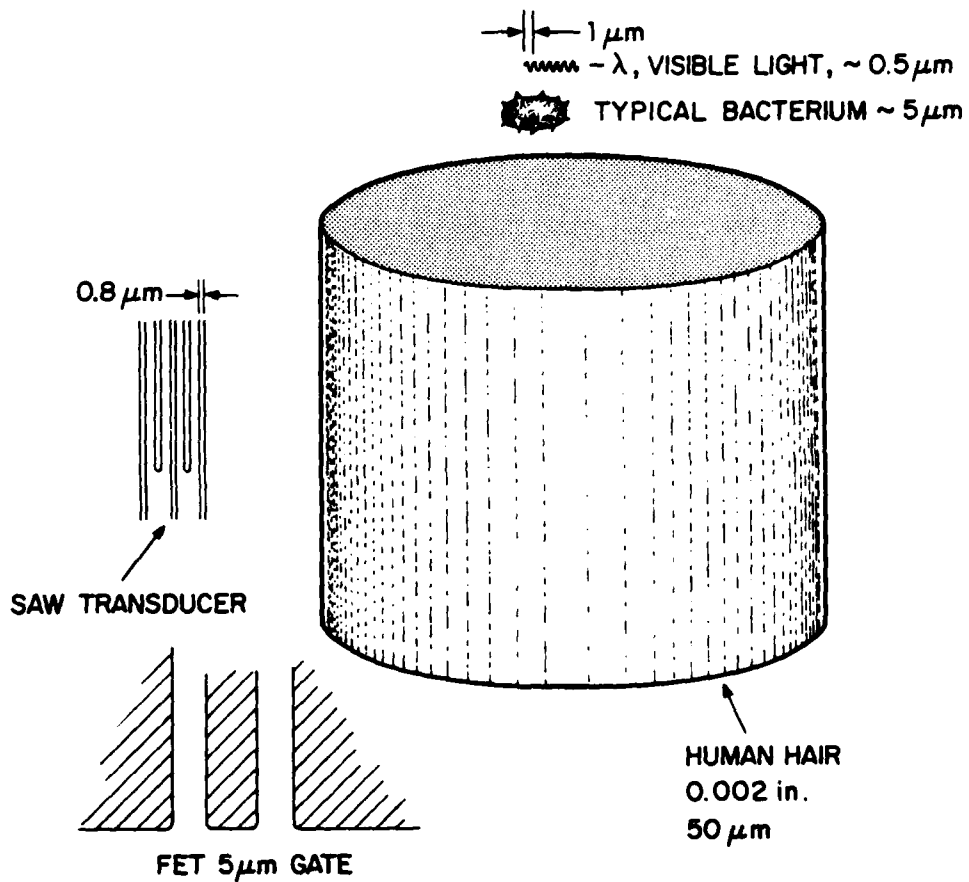
Fig. 1.1: Comparison of the size of a human hair to the wavelength of
visible light, to a bacterium (drawn with considerable
artistic license), and to two micrometer-scale devices.

10 ×
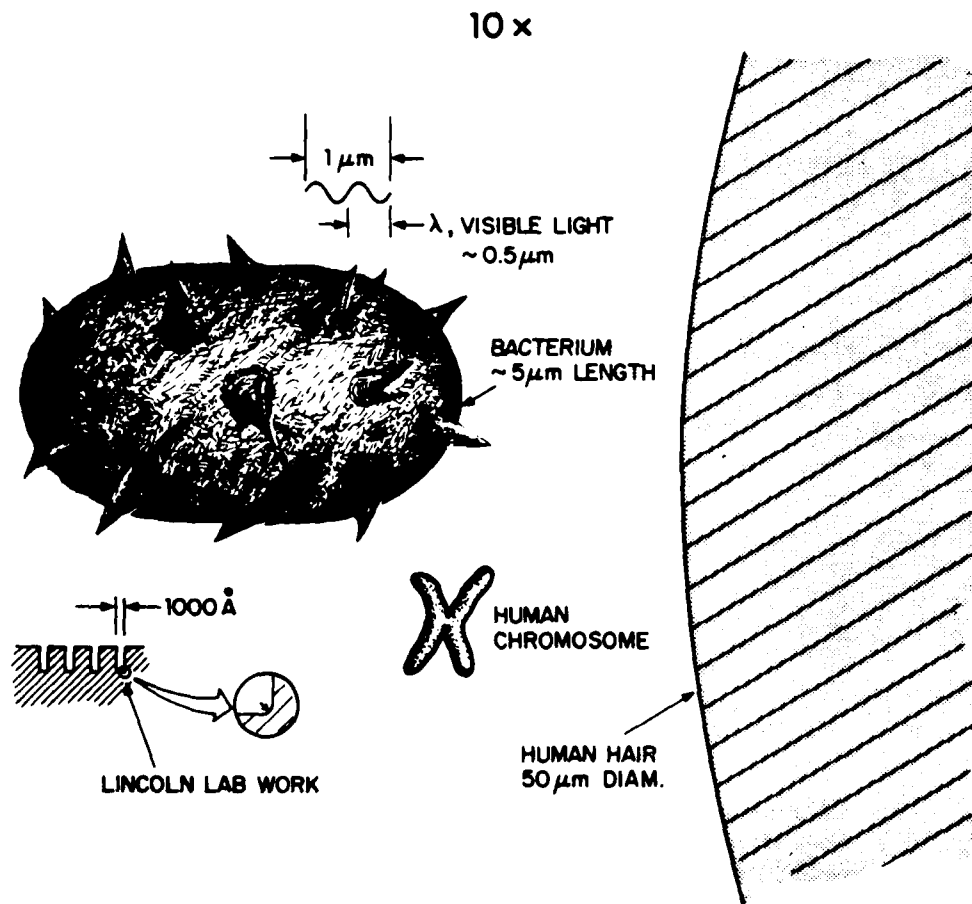
Fig. 1.2: Moving down in scale (tenfold magnification from Fig. 1.1), the bacterium appears huge next to a human chromosome and a surface relief structure fabricated at MIT's Lincoln Laboratory.
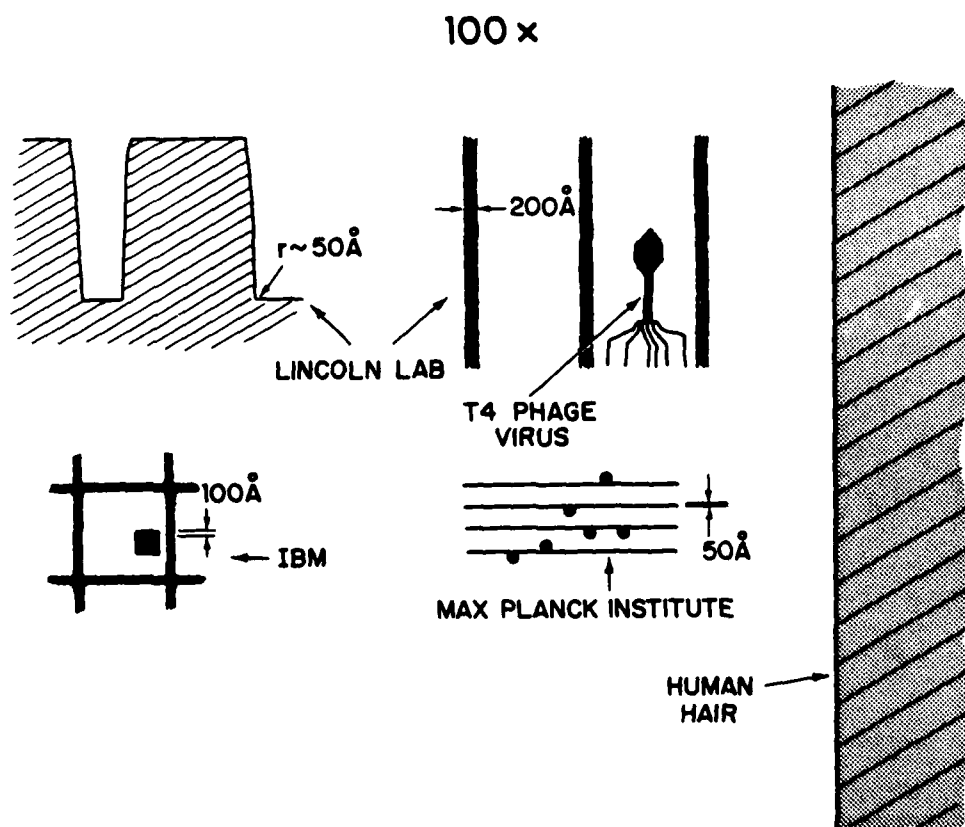
Fig. 1.3: Moving still further down in scale (hundredfold magnification from Fig. 1.1), some state-of-the-art microstructures from three labs are compared with a T4 Phage virus. The 200Å linewidth grating was fabricated using X-ray lithography by the group at Lincoln Laboratory; the 100Å wide lines of AuPd were made on a carbon foil with a scanning transmission electron beam microscope (STEM) by a group at IBM; and the 50Å lines were written in an insulin monolayer on a carbon foil also using a STEM at the Max Planck Institute (for details, see Smith, 1980, and references therein). Within the last five years, microstructure dimensions have shrunk through the realm of the smallest living things and are approaching the scale of single organic molecules.

quantitative predictions for the behavior of one-, two-, and three-dimensional disordered systems, where the length scale is set by the electron inelastic diffusion length. The localization models assumed non-interacting electrons, but Altshuler and Aronov (1979) and later Altshuler, Aronov, and Lee (1980a) and Altshuler, Khmel'nitzkii, Larkin, and Lee (1980b) showed that Coulomb interactions between the electrons in disordered systems would lead to similar effects in each of the three dimensions. In this case, the length scale is set by the quantity $(D\hbar/k_{B}T)^{1/2}$, where D is the electronic diffusion constant. The problem of electrical conduction in disordered systems is still attracting a great deal of theoretical attention, so much so that P. W. Anderson remarked that it is a "growth industry" at the 16th International Low Temperature Conference (1981).

Since 1977, considerable progress has been made in understanding the conduction process in disordered two- and three-dimensional systems. In two dimensions, resistance measurements cannot easily distinguish between the two competing models because they predict virtually the same behavior for the temperature-dependent conductivity; however, the relative importance of the two effects can be sorted out by application of a magnetic field. A useful system for studying the properties of a two-dimensional electron gas (Fowler, Fang, Howard, and Stiles, 1966) is the inversion layer in a silicon metal-oxide-semiconductor field-effect transistor (Si MOSFET). This structure has the advantage that it is possible to vary the density of the electron gas in a single sample by adjusting the gate voltage. Several groups (Bishop, Tsui, and Dynes,

1980; Uren, Davies, and Pepper, 1980; Wheeler, 1981, to list a few)
have observed non-ohmic behavior in Si MOSFETs and have interpreted it
in terms of the relative importance of electron localization and
electron-electron interaction effects in various regimes. Furthermore,
much effort has been made to produce and characterize another
two-dimensional system, extremely thin, evaporated or sputtered metal
films. For example, Dynes, Garno, and Rowell (1978) studied thin
(25-120Å) quench-condensed films of several different metals; Dolan and
Osheroff (1979) studied thin films of gold-palladium (AuPd) alloy; Van
den dries, Van Haesendonck, Bruynseraede, and Deutscher (1981) studied
thin (50-500Å) films of copper; and Markiewicz and Harris (1981)
studied thin (monolayer to 100Å) films of platinum (Pt). The results of
the experiments in two dimensions are reviewed by Dynes (1982).

The interplay of localization and interaction effects has also been
studied extensively in three-dimensional systems, where there is
predicted to be a well-defined metal-to-insulator transition (Mott,
1974; Abrahams et al., 1979). Dodson, McMillan, Mochel, and Dynes
(1981) investigated disordered germanium-gold (GeAu) alloys as a
function of composition and suggested that interaction effects as well
as localization effects are important in this system. Similar
conclusions were reached by Dynes and Garno (1981), who performed
tunnelling measurements on granular aluminum samples. They found a
large singularity in the electronic density of states near the
metal-insulator transition as expected from the interaction model. In
addition, measurements of the dc conductivity and far-infrared

transmission of three-dimensional samples of phosphorus-doped silicon by Rosenbaum, Andres, Thomas, and Lee (1981) have shown evidence for a cusp in $\sigma(T)$ as $T \to 0$. This observation can be explained by the Coulomb interaction model.

In the one-dimensional case which is of interest in this work, magnetic effects are smaller and less helpful; thus, one must put greater weight on the absolute magnitude of the effect and its dependence on material parameters and on temperature and sample size. The one-dimensional regime does have the advantage that the effect scales linearly with the characteristic length rather than only logarithmically as in the two-dimensional case.

Several groups (Giordano, Gilson, and Prober, 1979; Chaudhari and Habermeier, 1980; Masden and Giordano, 1981) observed a resistance rise at low temperatures in their one-dimensional samples and attempted to interpret their data in terms of the localization model. However, there remained several unanswered questions. The first measurements (Giordano, Gilson, and Prober, 1979) were made on AuPd alloy wires with poorly-known cross-sectional dimensions and it was not clear to what extent the resistance rise depended on the complex structure of the material, since bulk AuPd also exhibits a low temperature resistance rise (Edwards, Chen, and Legvold, 1970) In the later measurements (Chaudhari and Habermeier, 1980) on tungsten-rhenium (WRe) wires, the presence of a superconducting transition in the alloy complicated the interpretation of the data. Furthermore, the dependences of the resistance rise on temperature and resistivity and the magnitude of the

rise in these samples were not easily explained within the localization
theory, using current models of inelastic scattering processes in
one-dimensional samples.

When we began this work, we felt that what was needed was careful
measurements on a relatively clean, well-characterized system. To this
end, we developed a versatile technique for fabricating ultrathin wires
by evaporating a thin metal film at a shallow angle onto a step edge.
One advantage of this technique is that the dimensions and shapes of the
wires are easily controlled. We then made resistance measurements on
ultrathin wires of two pure metals, copper and nickel, and an alloy,
AuPd, the last for comparison with earlier work. Our results on the
copper wires, in particular, and also on the nickel and AuPd wires were
in such good agreement with the predictions of the interaction model,
that we decided to reanalyze the data in the literature. This improved
analysis made it clear that interaction effects are at least as
important as, and may dominate over, localization effects in
one-dimensional lithographically-produced metallic samples.

In Chapter Two, we give an overview of the theoretical situation
with emphasis on the one-dimensional case. An outline of the
calculations leading to quantitative predictions are discussed for both
the localization model and the interaction model. In Chapter Three, we
describe the technique that we used to fabricate the ultrathin wires and
also a technique for thinning the substrate so we could inspect the
wires in a high resolution transmission electron microscope. The low
temperature techniques and the electronic circuitry that were needed to

make the resistance measurements ar explained in Chapter Four. Then,
in Chapter Five, we present the results of our measurements on copper,
AuPd, and nickel wires, and also the results of a reanalysis of the data
already in the literature, and discuss their interpretation in terms of
the two models. Suggestions for future work are mentioned in the
summary in Chapter Six.

CHAPTER TWO: THEORETICAL SITUATION

One of the most exciting lessons in an elementary solid state
physics course is the unraveling of the mystery of how conduction
electrons actually make their way through a lattice of metal atoms.
There are two parts to the answer: (1) because of the periodic nature
of the lattice, the electrons can travel as plane waves (Bloch
functions), and (2) electrons only rarely scatter off other electrons as
a consequence of the Pauli exclusion principle (Kittel, 1976). The
simple free electron model is amazingly useful for understanding many of
the physical properties of metals and its application is justified by
the Fermi Liquid theory (for a discussion of this, see Ashcroft and
Mermin, p. 345f). For example, the experimental observation that the
current versus voltage characteristic of a normal metal conductor is
linear (Ohm's Law) can be derived within the framework of this model.
In addition, the temperature dependence of the resistance of such a
conductor can be qualitatively explained. At high temperatures, it is
primarily due to collisions of the conduction electrons with lattice
phonons. As the temperature is lowered, the phonons are frozen out,
and, at very low temperatures, the resistance is caused by scattering of
the electron waves by lattice defects. This residual resistance is
usually a temperature-independent quantity. The quantitative
temperature dependence of the resistance is difficult to treat
theoretically because it depends on the details of the electron-phonon,
electron-electron, and electron-impurity interactions.

The simple Bloch-function free-electron model breaks down in disordered solids such as thin metallic films and amorphous semiconductors. Over the past two decades, there has been an increasing interest in developing a model of conduction in these randomly disordered systems. In 1958, Anderson pointed out that one consequence of disorder is that the electron plane wave states are broken up and the electrons are spatially localized. As a result, electronic conduction proceeds via thermally-activated hopping from one localized state to another. At high temperatures, the localization should not be apparent because thermal phonons cause the electrons to hop, but, as the temperature approaches zero, the conductivity should approach zero exponentially.

In general, electron localization is treated within an independent electron theory. Recently, however, Altshuler and Aronov (1979) have shown that it is important to consider the effects of electron-electron interactions in disordered systems. They find that these many-body effects lead to a change in the electron density of states near the Fermi level which can be directly observed in the transport properties of these systems. The predictions of the interaction model for the temperature dependence of the resistance, independent of the effects of localization, are often strikingly similar to the predictions of the localization model.

In section 2.1, we discuss some of the scaling models of electron localization with emphasis on the predictions for one-dimensional systems. Then, in section 2.2, we discuss the interaction model, also

concentrating on the behavior predicted for one-dimensional conductors.
Finally, in section 2.3, we give our point of view on the theoretical
situation for one dimension.

2.1 Electron Localization Model

Since the introduction of the concept of electron localization in
disordered systems by Anderson (1958), it has received a lot of
theoretical attention and has been studied in one, two, and three
dimensions. The localized state is characterized by a localization
length, L_{loc}, which is a measure of the exponential decay of the
electron wave function. Following the work of Mott and Twose (1961) and
Landauer (1970), it was accepted that in a one-dimensional chain of
atoms, any amount of disorder would cause the electrons to be localized.
Thouless felt that this was a more general result and, in 1977, he
extended it to include a conductor of realistic cross-sectional
dimensions. What he predicted was that a conductor having a length much
greater than its cross-sectional dimension and a resistance greater than
a certain critical value would behave one-dimensionally at low enough
temperatures. Furthermore, he anticipated that the effects of
localization would be observable as a minimum in the resistance versus
temperature characteristic of the conductor at low temperatures. The
details of Thouless's argument are presented in section 2.1-1. This is
followed by a discussion of a more general scaling theory proposed by
Abrahams, Anderson, Licciardello, and Ramakrishnan (1979) in section

2.1-2, and a summary of the quantitative predictions of the theories in section 2.1-3.

2.1-1 Electron Localization in One Dimension

In order to derive the conditions for electron localization in a wire, Thouless (1977) used a scaling approach. He initially considered a block of conductor with length L, cross-sectional area A, resistance R, and a non-zero conductivity σ at T=0. The energy level spacing is given by

$$\frac{dE}{dN} \approx \frac{1}{N(0)\Omega}$$

where N(0) is the density of electron levels per unit volume per unit energy at the Fermi energy and Ω is the volume of the block. If two such blocks are joined end to end, the energy levels of the combined system are a linear combination of the energy levels of each subsystem, and the nature of the total wave function depends on the coupling matrix element, v(L). If the coupling is weak (v(L) $\ll$ dE/dN), the wave functions for the combined system closely resemble the wavefunctions for the single blocks and the electron is exponentially localized with a length that is not greater than the length of the block. On the other hand, if the coupling is strong (v(L) $\gg$ dE/dN), the wavefunctions of the combined system are complex combinations of those for a single block and the states of the electrons are extended throughout the system.

In order to relate these conditions to physically observable

quantities, Thouless argued that a good estimate for v(L) is the

broadening of an individual energy level, $\triangle E$, caused by putting the two

blocks together. Using the uncertainty principle, he showed that $\triangle E$ is

of order $\hbar/t$, where t is the time it takes an electron to diffuse to the

end of the block. This time is just equal to L^2/D, where D is the

electron diffusion constant. Then, $\triangle E$ can be related to the

conductivity of the block with the Einstein relation (Thouless, 1977),

$$\sigma = \frac{1}{2} e^2 DN(0)$$

via:

$$\Delta E \approx \frac{\hbar}{t} = \frac{\hbar D}{L^2} = \frac{\hbar}{L^2} \frac{2\sigma}{e^2} \frac{dE}{dn} .$$

Finally, substituting $1/\rho = L/(RA)$ for σ gives

$$\Delta E = \frac{\hbar}{e^2} \frac{2}{R} \frac{dE}{dN} . \tag{2-1}$$

At this point, it is clear that the condition for localization of the

electron states translates into a condition on the resistance of the

block, since, from eqn. (2-1), $v(L) \approx \Delta E \ll dE/dN$ implies that

$$R \gg \frac{2\hbar}{e^2} \, . \tag{2-2}$$

In other words, if the resistance of a localization length of wire exceeds the Thouless resistance, $R_T = 2\hbar/e^2 \approx 10k\Omega$, the electrons in the wire are in localized states. The size of a localized state is then given by the length of wire with $R \approx 2\hbar/e^2$, $L_{loc} = (2\hbar/e^2)(A/\rho)$.

Thouless also outlined the conditions for observing the effects of localization. Essentially, the electron is unaware that it is in a localized state at high temperatures because it undergoes frequent inelastic collisions and changes states many times before having a chance to diffuse a distance on the order of the localization length. As a result, the effects of localization are not reflected in the resistance. However, when the inelastic scattering length, l_{in}, is approximately equal to or greater than the localization length, L_{loc}, localization should influence the conduction. In order to achieve this condition, one can lower the temperature of the wire to increase l_{in} and reduce the cross-sectional area of the wire or increase its residual resistance to effectively decrease L_{loc}. Including estimates for both the electron-phonon and the electron-electron scattering rates, Thouless predicted that the hallmark of localization in a one-dimensional wire would be a resistance rising at low temperatures as T^{-2} or even as $\exp(1/T)$. The length scale determining the dimensionality in this case is l_{in}. For a wire with cross-sectional dimensions of 500Å x 500Å, his

calculations showed that the minimum in the R vs. T curve should occur at ~ $1.2°$K.

Clearly, the predictions of Thouless's model depend strongly on the details of the inelastic scattering in the wire. These in turn depend on whether the material in the wire is clean or dirty ($k_F l \gg 1$ or $k_F l \ll 1$ respectively, where k_F is the Fermi wavevector and l is the electron mean free path for elastic scattering), what the effective dimension is, and, in particular, whether electron-electron or electron-phonon scattering dominates. In general, the inelastic scattering rate depends on the temperature as

$$\frac{1}{\tau_{in}} = \gamma T^p \qquad (2-3)$$

where γ is a temperature-independent coefficient that may depend on the cross-sectional area of the sample and τ_{in} is the time between inelastic scattering events. The expected temperature and area dependences of the various scattering rates are discussed by Giordano (1980). Essentially, p is expected to vary from 1 to 4 depending on what the effective dimensionality of the wire is to the phonons.

When the early experiments on one-dimensional wires seemed to show a very small resistance rise with a weak $T^{-1/2}$ temperature dependence (implying a T^{-1} dependence for the inelastic scattering time, as we will show), additional mechanisms were proposed to account for the observations. Thouless (1980) redid his calculation for the case when the effects of localization are weak and suggested that electrons

scattering from the two-level-tunneling modes (Cochrane, Harris, Ström-Olson, and Zuckerman, 1975; Tsuei, 1978) believed to be present in metallic glasses and having $\tilde{\tau}_{in} \approx T^{-1}$ (in all materials), might provide an explanation for the observed temperature dependence. However, an estimate of the magnitude of the scattering rate expected from this mechanism by Black, Gyorffy, and Jäckle (1979) was two orders of magnitude too small to explain the data.

Recent calculations by Abrahams, Anderson, Lee, and Ramakrishnan (1981) have shown that the T^{-2} dependence generally expected for the electron-electron inelastic scattering time must be revised for disordered systems. They find that $\tilde{\tau}_{ee} \propto T^{-d/2}$, where d is the dimensionality of the system. It is not clear, however, what length scale determines the dimensionality of the system and in what systems this mechanism is dominant, but the two-dimensional form of this result seems to agree with the inelastic scattering times measured in ordinary MOSFETs (Uren, Davies, Kaveh, and Pepper, 1980) and in narrow-channel MOSFETs (Skocpol, Jackel, Hu, Howard, and Fetter, 1982).

2.1-2 General Scaling Theory of Localization

Thouless's scaling approach for one-dimension was generalized to d dimensions by Abrahams, Anderson, Licciardello, and Ramakrishnan (1979). They considered a hypercube of size L^d and argued that the dimensionless conductance,

$$g(L) = \frac{\Delta E(L)}{dE/dN} = \frac{G(L)}{e^2/2\hbar} \tag{2-4}$$

with

$$G(L) = cL^{d-2} \tag{2-5}$$

is the only scaling variable relevant to the problem. By analogy to the procedure followed by Thouless in one dimension, if b^d cubes of side bL are combined, the new $(\Delta E)^\prime/(dE/dN)^\prime$ at the scale bL is

$$g(bL) = f(b, g(L))$$

or, differentiating,

$$\frac{d \ln(g)}{d \ln(L)} = \beta(g) . \tag{2-6}$$

The important point about their scaling equation is that once g is known for a particular system, the g's for larger versions of the system are determined by eqn. (2-6) if $\beta(g)$ is known.

The behavior of β in the asymptotic limits was also explored by Abrahams et al. (1979). They found that for $g \rightarrow \infty$ (extended states), $\beta(g) \rightarrow d-2$ and for $g \rightarrow 0$ (localized states), $\beta(g) \rightarrow -\infty$. This can be

shown by calculating the derivative, $d\ln(g)/d\ln(L)$, in these limits using g as defined in eqns. (2-4) and (2-5). Smoothly connecting the two limits yielded new insight about the conduction problem. In one dimension, they found that the β function is always negative (it varies from $-\infty$ to -1 as $\ln(g)$ varies from $-\infty$ to $+\infty$), implying that all states are localized, as expected. In two dimensions, $\beta(g)$ is also always negative, varying from $-\infty$ to 0 as $\ln(g)$ varies from $-\infty$ to $+\infty$. For $d=3$, on the other hand, they showed, using perturbation theory, that there is a smooth cross-over from localized to extended states at a critical value of $g = g_c$, where $\beta = 0$. This is the mobility edge, defined by Mott (1966) as the point which separates localized and extended states.

The first correction to the form of β for large g has been calculated using perturbation theory and is found to be negative (Abrahams et al., 1979):

$$\beta(g) \approx (d-2) - \frac{a}{g}. \qquad (2-7)$$

Integrating eqn. (2-6) with the above expression for β gives, for the conductivities:

$$\sigma = \sigma_0 - a_1 L \qquad\qquad \text{(1-D)} \qquad \text{(2-8a)}$$

$$\sigma = \sigma_0 - a_2 \ln(L) \qquad\qquad \text{(2-D)} \qquad \text{(2-8b)}$$

$$\sigma = \sigma_0 + a_3/L \qquad\qquad \text{(3-D)} \qquad \text{(2-8c)}$$

where σ_0 represents the normal metallic conductivity in each of the three dimensions. From eqns. (2-8), it is apparent that the effect of localization in one and two dimensions is to reduce the conductivity or, equivalently, increase the resistance. In a more rigorous version of the scaling theory in one dimension, Anderson, Thouless, Abrahams, and Fisher (1980), associate the value of a_1, the coefficient of the linear term in eqn. (2-8a) with the inverse localization length, $(L_{loc})^{-1} = \rho/(AR_T)$. Following his own suggestion (Thouless, 1977) that the relevant length scale is the inelastic length, $\sqrt{D\tilde{\tau}_{in}}$, Thouless (1980) arrived at this expression for the relative resistance rise due to localization effects in a one-dimensional sample (where the dimensionality is determined by l_{in}):

$$\frac{\Delta R}{R} = (4D\tau_{in})^{1/2} \; \frac{\rho}{AR_T} \qquad (2-9)$$

with $R_T = 36{,}500\Omega$ this time. The resistance rise per decade of temperature in two dimensions has been calculated using perturbation theory by Anderson et al. (1979) and using scattering formalism by Anderson (1981) and is found to be:

$$\frac{\Delta R}{R} = \frac{e^2\alpha p}{2\pi^2\hbar} R \; \ln(10) \qquad (2-10)$$

where $R_\square$ is the sheet resistance, p is the exponent of the temperature in the formula (eqn. 2-3) for the inelastic scattering time, and α is a constant which is expected to be 1.

2.1-3 Quantitative Predictions

The relative change in the resistance due to the effects of localization in one dimension was given in eqn. (2-9). From the scaling arguments, it is plausible that the effects of electron localization on other physical properties of a conductor are determined by whether or not the relevant scaling length of the problem changes. For example, consider the behavior of a sample in a magnetic field. The radius of the smallest Landau orbit is (Altshuler, Khmel'nitzkii, Larkin, and Lee, 1980b):

$$l_H = \left(\frac{4\hbar c}{eH} \right)^{1/2}. \tag{2-11}$$

When l_H is less than l_{in} (at fairly high magnetic fields), it becomes the important scaling length and the conductivities given in eqns. (2-8) become field-dependent:

$$\sigma(H) = \sigma_0 - a_1 \left(\frac{4\hbar c}{eH} \right)^{1/2} \tag{1-D}$$

$$\sigma(H) = \sigma_0' + \frac{a_2}{2} \ln(eH) \tag{2-D}$$

$$\sigma(H) = \sigma_0 + a_3 \left(\frac{eH}{4\hbar c} \right)^{1/2}. \tag{3-D}$$

For similar reasons, electron localization effects are predicted to be observable in the frequency-dependent conductivity of a disordered system. In this case, the relevant scaling length can be taken to be the distance traveled by an electron during one period of the applied electromagnetic field (Santhanam, 1981):

$$l_\omega = \left(\frac{2\pi D}{\omega} \right)^{1/2}.$$

Substituting this for L in eqns. (2-8) gives:

$$\sigma(\omega) = \sigma_0 - a_1 \left(\frac{2\pi D}{\omega} \right)^{1/2} \qquad (1\text{-}D)$$

$$\sigma(\omega) = \sigma_0 + \frac{a_2'}{2} \ln(\omega) \qquad (2\text{-}D)$$

$$\sigma(\omega) = \sigma_0 + a_3 \left(\frac{\omega}{2\pi D} \right)^{1/2}. \qquad (3\text{-}D)$$

The frequency range where one might hope to observe these effects is in the far-infrared (Shapiro and Abraham, 1981).

On the other hand, the scaling models do not explicitly predict any changes in the electron density, n, or the electron density of states, $N(0)$, due to the effects of localization. As a result, the physical properties of the system which depend only on one of these quantities would not be expected to change when localization becomes important. Fukuyama (1980) and later Altshuler et al. (1980b) showed that this was rigorously true for the Hall coefficient, R_H, which only depends on n:

$$R_H = \frac{1}{nec} \rightarrow \frac{\delta R_H}{R_H} = 0.$$

Similarly, the specific heat for the free electron gas (Ashcroft and Mermin, 1976),

$$C_{el} = (\frac{\pi}{3})^{2/3} (\frac{k_B}{\hbar})^2 m n^{1/3} T$$

is not predicted to change either. Finally, we would not expect to learn much about localization from tunneling experiments, since they are used to probe the density of states near the Fermi surface.

2.2 Electron-Electron Interaction Model

The theoretical development of the localization picture (section 2.1) ignores the Coulomb interactions among the electrons. However, it is well known that these interactions can cause metal-insulator transitions. For example, the ground state in a low-density free-electron gas can be shown to be a Wigner crystal (Wigner, 1938) because the potential energy dominates the kinetic energy in this situation. Also, when Mott (1949) incorporated the effects of electron-electron interactions into his calculations, he found that the conductivity of a system does not go continuously to zero as the interatomic spacing is increased, but instead drops to zero at a specific nearest-neighbor distance (the Mott metal-insulator transition). It has been accepted for a long time that, in a pure metal, Coulomb interactions lead to an electron-electron scattering rate of

$$\frac{1}{\tau_{ee}} \propto (\frac{4\pi e^2}{k_o^2})^2 (k_B T)^2$$

(Ashcroft and Mermin, 1976) where k_0 is the Thomas-Fermi wavevector defined by $k_0^2 = 4\pi e^2 N(0)$ for $T \ll T_F$. Only recently, though, has the calculation been done for a disordered metal. In 1979, Altshuler and Aronov showed that when electron-electron interactions are taken into account in a three-dimensional disordered system, they lead to changes in the behavior of the thermodynamic and transport properties. Altshuler, Aronov, and Lee (1980a) repeated the calculation for two dimensions, and Altshuler, Khmel´nitzkii, Larkin, and Lee (1980b) calculated the influence of Coulomb interactions on the Hall effect and magnetoresistance in two dimensions and on the temperature dependence of the conductivity in one dimension.

The calculations in these papers are very technical, involving a perturbation to lowest order in the dynamically-screened Coulomb interaction in the presence of static impurity scattering. In section 2.2-1, we outline a simpler, nonperturbative calculation that arrives at similar conclusions. This argument was given by Lee (1981) and published independently by Maldague (1981) and by Abrahams, Anderson, Lee, and Ramakrishnan (1981). Then, in section 2.2-2, we discuss the quantitative predictions of the interaction model. Finally, in section 2.2-3, we present our way of thinking about the theoretical situation in one dimension.

2.2-1 Non-Perturbative Calculation

In the following, the calculation of Abrahams et al. (1981,

sec. II) of the influence of electron-electron interactions on the

single particle density of states of a disordered system is reviewed.

Their assumptions are that $k_F l \gg 1$ (the metallic limit, according to

Ioffe and Regel, 1960) and that the ions can be represented by a uniform

distribution of positive charge with the same average density as the

electronic charge. Then, in the Hartree-Fock theory (Ashcroft and

Mermin, 1976), the potential due to the ions approximately cancels the

potential due to the electrons (the "direct" term), so the energy of the

electron in the mth state is just given by:

$$E_m = \varepsilon_m + \Sigma_m \qquad (2\text{-}12)$$

where $\varepsilon_m = \hbar^2 k_m^2/(2m)$ and Σ_m is the so-called exchange term which

includes the effects of interactions. Using the Hartree-Fock theory,

Σ_m can be written as:

$$\Sigma_m = -\sum_n \int d\vec{r} d\vec{r}\,' \phi_m^*(\vec{r}) \phi_n^*(\vec{r}\,') \phi_m(\vec{r}\,') \phi_n(\vec{r}) v(\vec{r} - \vec{r}\,')$$

$$(2\text{-}13)$$

where $v(\vec{r})$ is the static interaction potential and the sum is over all

occupied states. Because of the disorder, the electron eigenfunctions

are no longer Bloch waves, but the ϕ's are chosen to be the exact (and

as yet unknown) eigenstates of noninteracting electrons in a disordered potential.

In order to calculate the single electron density of states, it is necessary to determine the shift in Σ_m due to the addition of an electron at energy $\mathcal{E}$ near the Fermi energy, $\mathcal{E}_F$. On the average, this correction is equal to

$$\tilde{\Sigma}(\varepsilon) = \frac{1}{N(0)} \sum_m \delta(\varepsilon-\varepsilon_m) <\Sigma_m>_{av}$$

(2-14)

where the brackets mean an average over impurities. Substituting eqn. (2-13) for Σ_m then gives

$$\tilde{\Sigma}(\varepsilon) = -\int_{-\infty}^{0} d\varepsilon' F(\varepsilon,\varepsilon';\vec{r},\vec{r}') v(\vec{r}-\vec{r}')$$

(2-15)

where

$$F(\varepsilon,\varepsilon';\vec{r},\vec{r}') = \sum_{m,n} \delta(\varepsilon-\varepsilon_m)\delta(\varepsilon'-\varepsilon_n) \int d\vec{r} d\vec{r}' <\phi_m^*(\vec{r})\phi_n^*(\vec{r}')\phi_m(\vec{r}')\phi_n(\vec{r})> \quad (2-16)$$

Averaging the four wavefunctions in eqn. (2-16) is an intractable problem, since the ϕ's are not known for the disordered system. However, as Abrahams et al. (1981) point out, the quantity in eqn. (2-16) is the same as the one that is found in a density-density

correlation function, $A(q,\omega)$:

$$A(q,\omega) = \int_{-\infty}^{\infty} dt\, d\vec{r}\, d\vec{r}\,' e^{i\omega t}\, e^{i\vec{q}\cdot(\vec{r}-\vec{r}\,')} < [\rho(\vec{r},t)\rho(\vec{r},0)] >.$$

(2-17)

If it is assumed that the density fluctuation decays by diffusion, it can be shown that

$$A(q,\omega) = N(0)\ \mathrm{Im}\left\{ \frac{Dq^2}{-i\omega + Dq^2} \right\}$$

(2-18)

(Forster, 1975).

Eqn. (2-18) can be related to the expression in eqn. (2-16) by expanding the density operator, ρ , in terms of the ϕ's. At T=0 and for $\omega > 0$, eqn. (2-17) becomes:

$$A(q,\omega) = \sum_{m,n} \int d\vec{r}\, d\vec{r}\,' e^{i\vec{q}\cdot(\vec{r}-\vec{r}\,')} < \phi_m(\vec{r})\phi_n^*(\vec{r})\phi_m^*(\vec{r}\,')\phi_n(\vec{r}\,') > \delta(\varepsilon_n - \varepsilon_m - \omega).$$

(2-19)

where the sum is over all states with n occupied and m unoccupied. Since this is a sum over the free electron eigenvalues, it can be rewritten as

$$A(q,\omega) = \int_0^\infty d\varepsilon \int_{-\infty}^0 d\varepsilon' F(\varepsilon,\varepsilon';\vec{r},\vec{r}')e^{i\vec{q}\cdot(\vec{r}-\vec{r}')}\delta(\varepsilon-\varepsilon'-\omega).$$

$$(2-20)$$

Then, recognizing that F only depends on $\varepsilon - \varepsilon'$ and $\vec{r}-\vec{r}'$ allows eqn. (2-20) to be rewritten as

$$A(q,\omega) = \omega \int F(\omega,\vec{r})e^{i\vec{q}\cdot\vec{r}}d\vec{r}.$$

$$(2-21)$$

Finally, by analogy with eqn. (2-18), they obtain:

$$\int F(\omega,\vec{r})e^{i\vec{q}\cdot\vec{r}}d\vec{r} = N(0)\left[\frac{Dq^2}{\omega^2 + (Dq^2)^2}\right].$$

$$(2-22)$$

The shift in $\sum_m$ is then calculated using eqns. (2-15) and (2-22):

$$\tilde{\Sigma}(\varepsilon) = -N(0)\int_{-\infty}^0 d\varepsilon' \int d\vec{q}\left[\frac{Dq^2}{(\varepsilon-\varepsilon')^2 + (Dq^2)^2}\right]v(\vec{q})$$

$$(2-23)$$

where $v(\vec{q})$ is defined by:

$$v(\vec{q}) = \int v(\vec{r})e^{i\vec{q}\cdot\vec{r}}d\vec{r}.$$

Since the exchange correction depends on the energy, the density of
states will be changed by an amount equal to

$$\delta N(\epsilon) = \frac{\partial \tilde{\Sigma}(\epsilon)}{\partial \epsilon} \tag{2-24}$$

$$= -N(0) \int_{-\infty}^{0} d\epsilon' \int d\vec{q} \; \frac{Dq^2 2(\epsilon-\epsilon')v(\vec{q})}{[(\epsilon-\epsilon')^2 + (Dq^2)^2]^2} \; .$$

Choosing v(q) to be the statically-screened Coulomb interaction (rather
than the more complicated, dynamically-screened interaction in the
original derivation) defined by

$$v(q) = \frac{e^2}{k_0^2 + q^2} \tag{2-25}$$

with $k_0 = 4\pi e^2 N(0)$, and letting $q \to 0$, gives

$$v(0) = \frac{1}{N(0)}. \tag{2-26}$$

With this substitution, counting powers of q in the integral in
eqn. (2-24) finally yields the following forms for $N(\mathcal{E})$ in each of the
three dimensions ($\mathcal{E}\mathcal{T} \ll 1$):

$$N(\epsilon) \sim N(0) + \frac{\alpha_3 N(0) |\epsilon\tau|^{\frac{1}{2}}}{(\epsilon_F \tau)^2} \qquad \text{(3-D)} \qquad \text{(2-27a)}$$

$$N(\epsilon) \sim N(0) + \frac{\alpha_2 N(0)}{(\epsilon_F \tau)\pi} \ln(|\epsilon|\tau) \qquad \text{(2-D)} \qquad \text{(2-27b)}$$

$$N(\epsilon) \sim N(0) + \frac{\alpha_1 N(0)}{|\epsilon\tau|^{\frac{1}{2}}} \qquad \text{(1-D)} \qquad \text{(2-27c)}$$

where the α's are numerical factors and τ is the elastic scattering time. The reason that these expressions are independent of the interaction constant, e^2, can be traced back to the choice of v(q) at q=0 in eqn. (2-26).

In order to determine the length scale setting the dimensionality in this model, Abrahams et al. (1981) referred to eqn. (2-24) and noted that, in the q integration, ϵ serves as a cut-off of the singularity in the denominator. Therefore, the region with $q < q_0$ (where $q_0 = (\epsilon/D\hbar)^{1/2}$) has little effect on the integration, establishing a length scale of

$$1 = \left(\frac{D\hbar}{\epsilon} \right)^{1/2}.$$

$$\text{(2-28)}$$

When $k_B T > \epsilon$, it is substituted for ϵ in eqns. (2-27) and (2-28).

2.2-2   Quantitative Predictions

The temperature dependence of the conductivity of a disordered system can be computed within the interaction model using the Einstein relation, $\sigma = e^2 DN(\mathcal{E})/2$ and eqns. (2-27) for $N(\mathcal{E})$. In three dimensions, there is a singularity in the density of states at the Fermi energy which leads to a conductivity that increases with increasing temperature until $k_B T \tau /\hbar \approx 1$:

$$\sigma = \sigma_0 + \frac{\alpha_3 \sigma_0 \sqrt{k_B T}}{(\varepsilon_F \tau)^2} \qquad (\frac{k_B T \tau}{\hbar} \ll 1)$$

(2-29)

contrary to the usual behavior in a metal. In two dimensions, the total correction to the conductivity due to the electron-electron interactions is:

$$\delta\sigma = \frac{e^2}{4\pi^2 \hbar} (2-2F) \; \ln(\frac{k_B T \tau}{\hbar})$$

(2-30)

(Altshuler, Aronov, and Lee, 1980a). Here, F is a screening constant that is expected to approach 1 for short-range interactions and vanish for long screening lengths. Finally, in one dimension, the dip in the density of states gives a decrease in the conductivity:

$$\sigma = \sigma_0 - \frac{1}{A} \frac{e^2}{\hbar\pi} \left(\frac{\hbar D}{2k_B T} \right)^{1/2} (2-F).$$

(2-31)

(Altshuler, Khmel'nitzkii, Larkin, and Lee, 1980b). It is interesting to note that, in both one and two dimensions, the predictions for $\sigma(T)$ from the interaction model have the same functional form as the predictions of the localization model if $(D \mathcal{C}_{in})^{1/2}$ is replaced by $(\hbar D/k_B T)^{1/2}$. This also implies that if $(D \mathcal{C}_{in})^{1/2} \gg (D\hbar/k_B T)^{1/2}$, interaction effects will cause changes in the conductivity before localization effects become important.

The change in the single particle density of states due to interactions also influences the other properties of disordered systems. In particular, in the free electron model, the electronic specific heat depends directly on the density of states via

$$C_{el} = \frac{\pi^2}{3} k_B^2 T \, N(0).$$

Prediction of the correction to C_{el} is not straightforward, however, because of the distinction between the single particle density of states and the density of states measured by specific heat experiments. Taking this into account in two dimensions, Altshuler et al. (1980a) show that

$$\frac{\delta C_{el}}{C_{el}} = (\pi \varepsilon_F \tau / \hbar)^{-1} (1 - 2F) \ln(\frac{k_B T \tau}{\hbar}).$$

Using eqns. (2-27) and the form of C_{el}, we might guess for the other dimensions:

$$C_{el} \sim T^{3/2} \qquad \text{(3-D)}$$

$$C_{el} \sim T^{-1/2}. \qquad \text{(2-D)}$$

Application of a magnetic field is not expected to affect the density of states to the order calculated by Abrahams et al. (1981). Although Altshuler and Aronov (1979) predict a negative magnetoresistance in three dimensions, Altshuler et al. (1980b) find no magnetoresistance in two dimensions. On the other hand, the Hall effect should show a change (Altshuler et al., 1980b). To see this, consider the Hall constant in the free electron model:

$$R_H = \frac{1}{nec.}$$

The change in the density of states leads to a change in the conductivity which translates into a change in the electron density:

$$\frac{\delta N}{N} \quad \alpha \quad \frac{\delta\sigma}{\sigma} \quad = \quad \frac{\delta n}{n}.$$

But,

$$\frac{\delta R_H}{R_H} \quad = \quad -\frac{\delta n}{n}$$

so

$$\frac{\delta R_H}{R_H} \quad \alpha \quad \frac{\delta\sigma}{\sigma}.$$

In general, the constant of proportionality should depend on the dimensionality of the system and, for two dimensions, Altshuler et al. (1980b) find

$$\frac{\delta R_H}{R_H} \quad = \quad -2\frac{\delta\sigma}{\sigma}.$$

A naive estimate for the frequency dependence of the conductivity within the interaction model can be made by substituting $h\omega$ for $\mathcal{E}$ in eqns. (2-27) and calculating $\sigma(\omega)$ with the Einstein relation (Santhanam, 1981). This gives the following forms for the change in the conductivity in each of the three dimensions:

$$\delta\sigma \quad \alpha \quad (\hbar\omega)^{1/2} \qquad\qquad \text{(3-D)}$$

$$\delta\sigma \quad \alpha \quad \ln(\hbar\omega) \qquad\qquad \text{(2-D)}$$

$$\delta\sigma \quad \alpha \quad 1/(\hbar\omega)^{1/2} \qquad\qquad \text{(1-D)}$$

However, because the statically-screened interaction potential was used instead of the dynamically-screened one, the simplified method is not adequate for calculating the detailed frequency dependence. Altshuler and Aronov (1979) do this rigorously in three dimensions and find:

$$\frac{\delta\sigma(\omega)}{\sigma} = \frac{4\sqrt{2}}{45\pi^2} \frac{\lambda\omega^{1/2}}{N(\varepsilon_F)D^{3/2}} [(2 + 4\sqrt{2}) + i(1 - 4\sqrt{2})]$$

where λ is the "effective electron interaction constant".

Tunneling measurements on disordered systems should provide the most direct information about the interaction model since they probe the single electron density of states close to the Fermi energy. If one tunnels into a disordered metal from a clean metal, the conductance of the junction is just

$$G = \frac{dI}{dV} \, \alpha \, e|T|^2 \, N_1(\varepsilon_{F1}) N_2(\varepsilon_{F2} + eV)$$

(Tinkham, 1975) where N_1 and N_2 are the densities of states for the clean and disordered metal respectively, T is the tunneling matrix element, and V is the voltage applied across the junction. Substituting eV for $\mathcal{E}$ in eqns. (2-27) then gives an estimate for how interactions might affect the tunneling conductance:

$$\frac{\Delta G}{G} \, \alpha \, \sqrt{eV} \qquad\qquad (3\text{-}D)$$

$$\frac{\Delta G}{G} \, \alpha \, \ln(eV) \qquad\qquad (2\text{-}D)$$

$$\frac{\Delta G}{G} \, \alpha \, \frac{1}{\sqrt{eV}}. \qquad\qquad (1\text{-}D)$$

These quantitative predictions for the interaction model should be compared to the results for the localization model in section 2.2-3. The form of the temperature-dependent conductivity and the frequency-dependent conductivity are similar in the two models. However, application of a small magnetic field is predicted to have a much greater influence on localization effects than on interaction

effects in two and three dimensions. The Hall constant is not predicted

to change in the localization theory, but is expected to vary in the

interaction theory. Also, tunneling measurements should be able to

distinguish between the two models.

2.3 Summary for One Dimension

In either the localization or the interaction theory, as long as

the resistance increase is small, it can be written as

$$\frac{\delta R}{R} \approx \frac{\Lambda}{L_Q}.$$

The length Λ has a different meaning in each of the two models, while

the length $L_Q = (A/\rho)(4\hbar/e^2)$ is the length of conductor having the

characteristic quantum resistance, $R_Q = 4\hbar/e^2 \approx 16,400\,\Omega$. Using the

free electron model, L_Q can be expressed in more microscopic terms as

$L_Q \approx k_F^2 A l$, so that it would be of the order of the mean free path, l,

in the case of a "wire" made up of a single chain of metal atoms, but is

proportionally larger for wires of realistic cross sections.

As we explained in section 2.1-1, the length Λ in the

localization model is essentially the inelastic diffusion length,

$(D \tau_{in})^{1/2}$, where τ_{in}, the inelastic scattering time, is the relaxation

time for energy exchange of the electron with its environment. τ_{in} is

usually determined by the electron-phonon coupling strength, which can vary markedly between metals and $\widetilde{G}_{in}$ is normally expected to vary as T^{-p}, where $p \approx 3$.

Although not derived this way in section 2.2-1, the result of Altshuler et al. (1980b) is equivalent to taking $\Lambda \approx \xi_N \approx (D\hbar/k_B T)^{1/2}$, where ξ_N is the "normal metal coherence length" which is a measure of the smallest wavepacket that can be constructed from electron waves having energies within $\sim k_B T$ of the Fermi surface. In contrast to the $\widetilde{G}_{in}$ of the localization model, this model involves no poorly-known mechanism-dependent parameters.

CHAPTER THREE: SAMPLE FABRICATION

Since metal wires with well-controlled cross-sectional dimensions which were less than 1000Å were required for this work, we decided to fabricate our samples using a step-edge shadowing technique. The idea of shadowing structures for contrast enhancement in a transmission electron microscope (TEM) has been in use for many years (Bradley, 1956). A similar technique was used to make wire-grating polarizers by shadowing ruled diffraction gratings (Bird and Parrish, 1960). More recently, D. C. Flanders (1979) developed a shadowing technique to make high aspect ratio, narrow linewidth metal structures for X-ray lithography masks. We used a variation on this technique to make simple high-resolution structures directly (Flanders and White, 1981).

3.1 Basic Shadowing Technique

An outline of the basic shadowing technique is shown in Fig. 3.1. All of the sample preparation was done in the submicrometer facility at MIT Lincoln Laboratory. Essentially, a square-wave surface relief pattern was etched into silicon dioxide (SiO_2) using reactive ion etching (RIE), and a thin metal film was evaporated at an oblique angle onto the step edges to form the wires. The master grating mask was fabricated using electron beam lithography. Conventional photolithography and a lift-off process were used initially to define, on the wafer, the chromium mask for the RIE. In the following

FABRICATION OF THIN WIRES BY SHADOWING
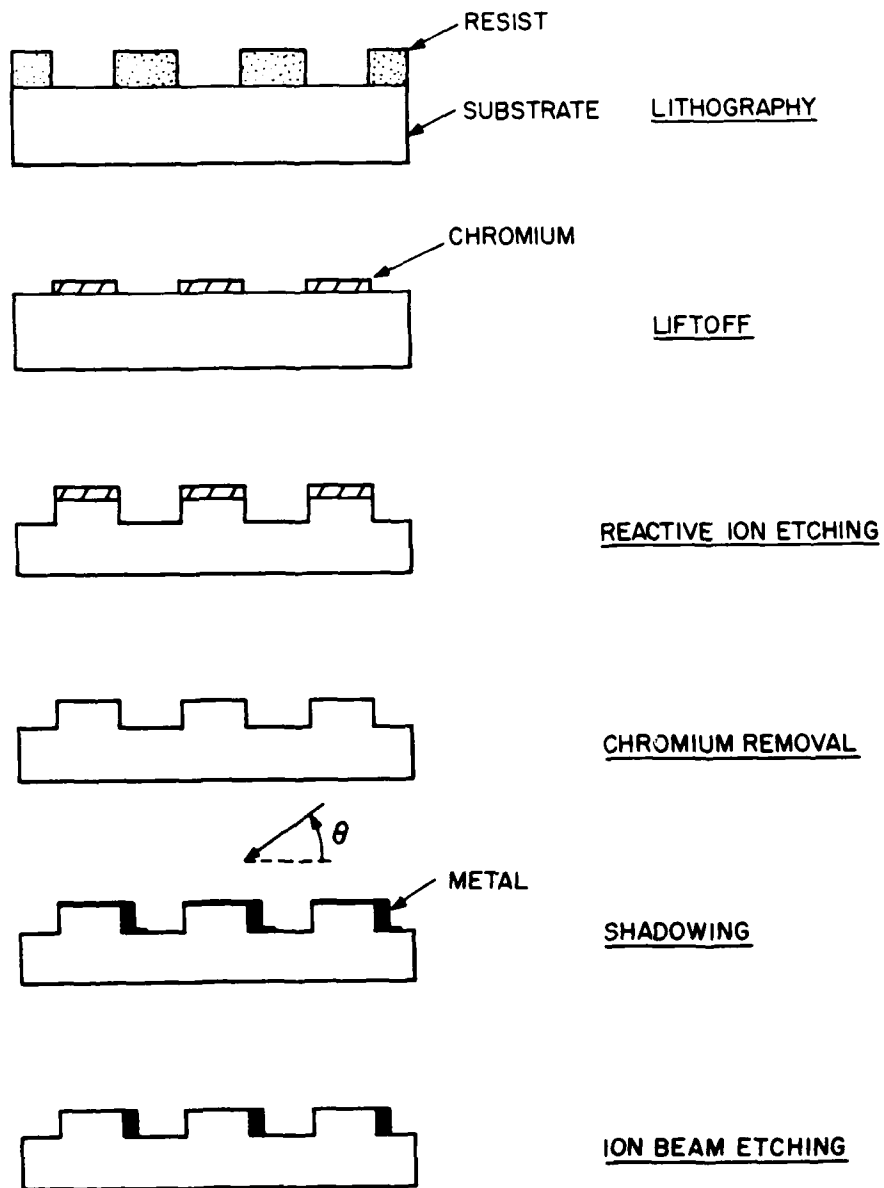
Fig. 3.1: Fabrication sequence for producing an ultrathin wire at a step edge with precisely controlled thickness and width. Using this technique, it is possible to make wires with cross-sectional dimensions less than 100Å.

paragraphs, these steps are described in detail.

3.1-1 Chromium Master Mask Fabrication

We decided to generate the master grating mask using electron beam lithography (EBL) rather than optical projection lithography because the former produced smoother edges on the grating lines. However, it was only possible to use EBL because the small area coverage did not require prohibitive exposure times. The grating design was digitized using MANN 3600 software and the resulting information was reconfigured for a ETEC Co. LEBES-D model scanning electron beam system (SEBL) using software developed by D. C. Shaver. Field stitching errors, which are a disadvantage of SEBL-generated patterns, were not a problem in this work since the wires were found to follow the relatively smooth bends in the steps due to these errors without loss of uniformity. The spacing of the grating was not crucial either, so we settled on a 4μm period as a good compromise between ease of fabrication with ultraviolet (uv) light and reasonable yield of continuous wires. The completed master mask was in 200Å of chromium on 25 mil thick glass.

3.1-2 Substrate Preparation

We started with single crystal, 1 1/2 inch diameter silicon wafers in the (100) orientation which were purchased from Monsanto Corp. They were 10 mils thick and were polished only on the top side. First, a 5000Å thick layer of SiO_2 was thermally grown on the smooth side of the wafer in a standard furnace. The oxide was chosen because it has

excellent characteristics for etching and also because it is an insulator at room temperature, unlike silicon. The thickness and quality of the oxide can be readily determined by inspection with the naked eye since the apparent color changes dramatically with ~100Å variations in oxide depth (Pliskin and Conrad, 1964).

Extreme care was necessary at all stages in the sample preparation to avoid contaminating the samples with organic materials (fingerprints, etc.) and dust. Organic contamination can lead to poor resist or metal film adhesion and dust particles are often much larger than the structures that were being made. Sometimes this meant knowing when not to put the samples through the cleaning procedure. However, if the wafers appeared dirty after the oxide had been grown, or if wafers were being re-used (not recommended in general), we used the cleaning procedure described in Appendix A.

3.1-3 Chromium RIE Mask Fabrication

Once a master mask and a clean, oxide-coated wafer were obtained, we were ready to fabricate the chromium RIE mask on the surface of the silicon. The grating pattern was transferred to a layer of photoresist on the silicon wafer using conventional contact lithography. The photoresist (Shipley AZ1350B) was spun onto the wafer at 3000 rpm producing a ~5000Å thick coating. Sometimes the resist did not stick well to the SiO_2, so usually we used a monolayer of an adhesion promoter, N,N-dimethyl-N-octadecyl-3-aminopropyltrimethoxysilyl chloride (DMOAP-- Kahn et al., 1973; Kahn, 1973), underneath the resist. This

was accomplished by simply dipping the wafer in a 0.1% by volume solution of DMOAP, rinsing it in deionized (DI) water, and baking it at $110^{\circ}C$ for 60 minutes. The resist was also baked for 20 minutes at $80^{\circ}C$.

Next, the master mask and the resist-coated wafer were held in intimate contact using a vacuum hold-down scheme. The wafer was placed on a piece of thin, flexible rubber, the mask was placed on top of the wafer so that it was aligned with the flat edge on the wafer, and another piece of rubber with a hole larger than the pattern to be exposed was placed on top of the mask. Then the air was evacuated from the space between the two pieces of rubber (which formed a tight seal around the mask-wafer combination), drawing the mask and the wafer into contact. As the last bit of air was removed, it was possible to see interference fringes moving outward and the best contact existed when the last fringe disappeared. Often, pieces of dust on the substrate or mask (which should also be carefully cleaned in the same manner as the wafer) produced regions of poor contact which were readily observable because of the prominent interference fringes radiating out from them. The black fringes cause areas of reduced exposure, so it was worth making an effort to remove the particles in crucial regions of the pattern. The wafers are flexible enough to bend around particles, though, so it was not necessary (and impossible anyhow) to remove all the particles. Exposure times depend on the spectrum and intensity of the uv light and the age of the resist. We used a Orion model 8160 uv lamp and exposure times varied between 10 and 20 seconds. The exposed resist was developed away by soaking with mild agitation in Shipley AZ

Developer for 45 seconds. It was crucial to remove even the last monolayer of resist, so the development was followed by a 15 second plasma etching in a mixture of 97% helium and 3% oxygen.

The grating pattern was transferred to chromium by a lift-off procedure (Fig. 3.2). A 200$\overset{o}{A}$ layer of chromium was evaporated at normal incidence onto the grating pattern in the resist, coating the tops and bottoms of the resist steps. Then the resist was dissolved in acetone, hopefully floating away the chromium on top of it and leaving behind a chromium pattern which was the negative of the original. Unfortunately, the true resist profile was usually rounded at the top and bottom due to over-development, improper exposure, or standing wave patterns in the resist. This meant that the chromium film was often partially connected and tended to tear rather than lift off. The jagged edges were faithfully reproduced in succeeding steps and resulted in discontinuous wires. This is clearly illustrated in Fig. 3.3 which is a scanning electron microscope (SEM) picture of a wire that failed to follow a jagged edge.

As a result, we switched to ion beam etching (IBE) for the pattern transfer to increase our yield. (We tried using a wet chemical etch here, but discovered that it left a residue of chromium pieces which were impossible to remove completely.) Photoresist is an adequate IBE mask, so all we had to do was shuffle the order of the steps around (see Fig. 3.4): first, the chromium was evaporated onto the wafer (eliminating any resist-SiO_2 adhesion problems); next, the grating was photolithographically reproduced in a layer of resist which was spun on
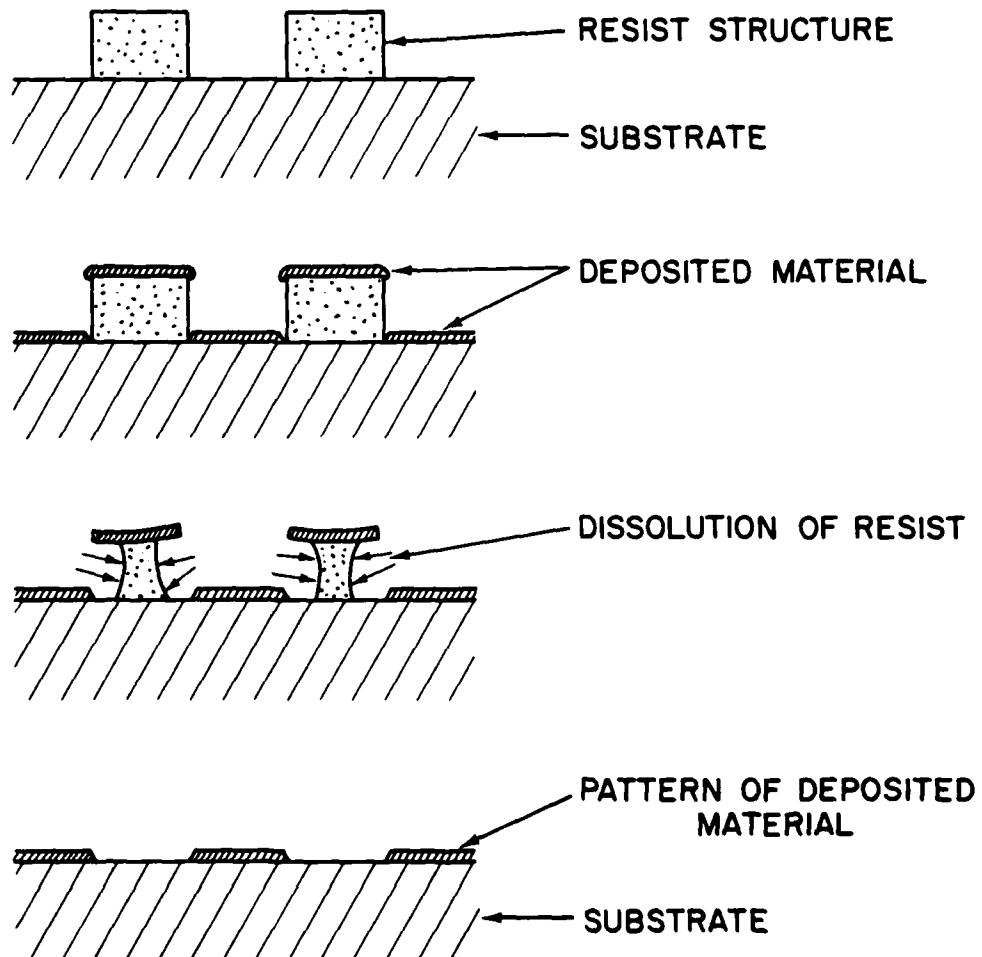
Fig. 3.2: Outline of the lift-off process used to make a chromium RIE mask on a silicon wafer (from Flanders, 1978).

30KV X56000 1U 048 31381
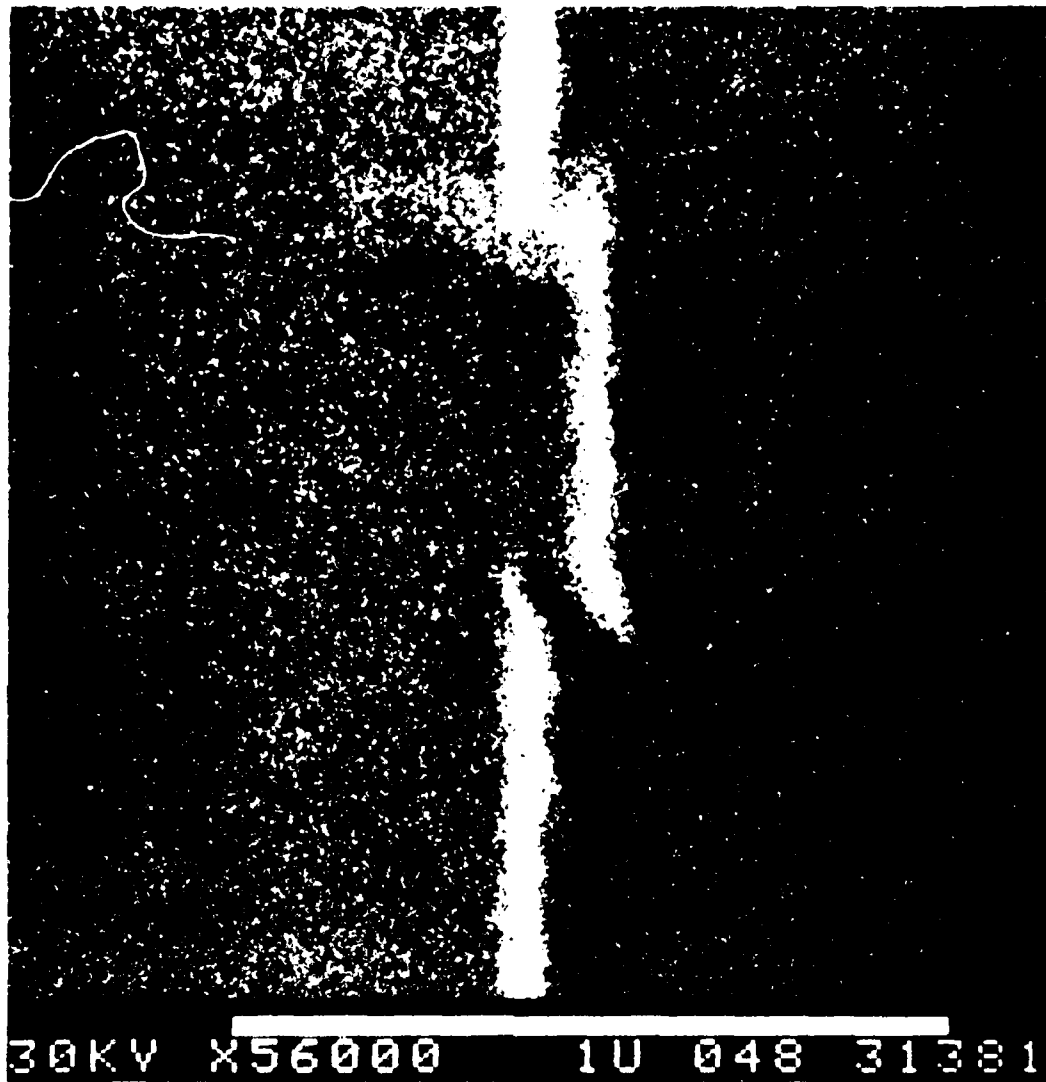
Fig. 3.3: SEM micrograph of a discontinuous 1000 Å wide nickel wire fabricated by the following technique. [...] an oxide edge was [...] used to [...] fabrication of chromium [...]. The bar at the bottom of the figure is 1 μm long.

ION BEAM ETCHING OF CHROMIUM MASK

CHROMIUM
SUBSTRATE   CHROMIUM EVAPORATION

RESIST

LITHOGRAPHY

ION BEAM ETCHING

RESIST DISSOLUTION

REACTIVE ION ETCHING
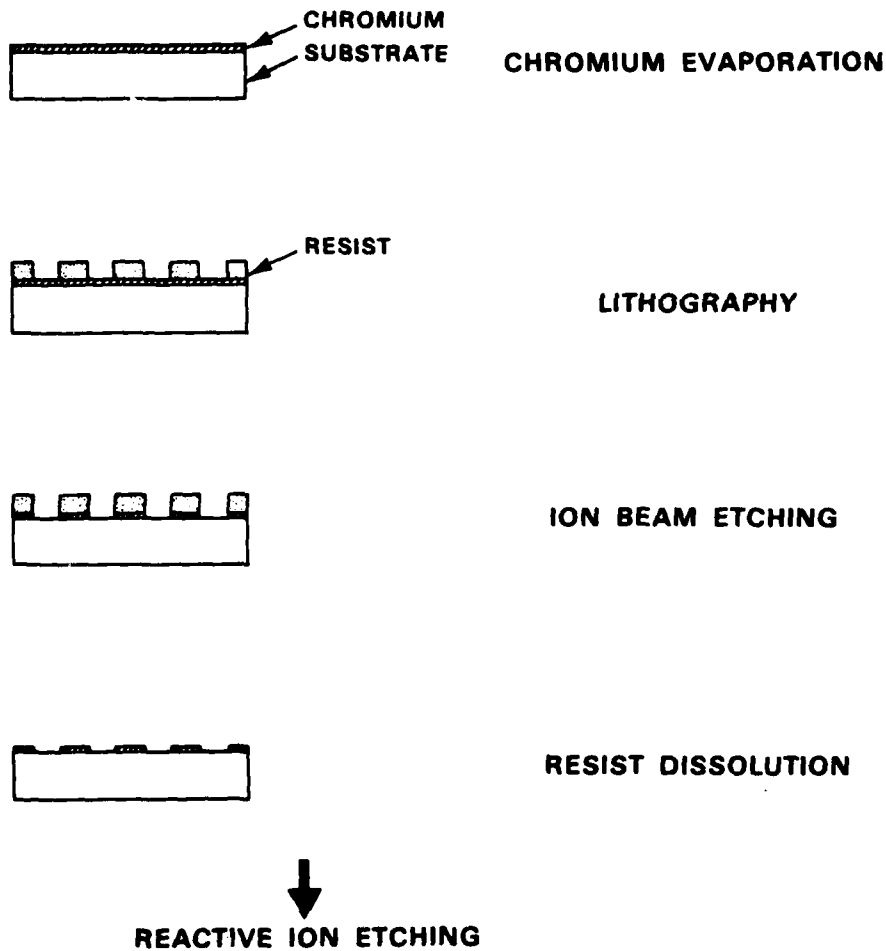
Fig. 3.4:   Substitution for the first two steps in the fabrication
sequence in Fig. 3.1 to avoid problems with lift-off. In
this procedure, the chromium RIE mask is made using IBE.

top of the chromium; then the exposed chromium was etched to the SiO_2 with IBE; finally, the remaining resist was removed with acetone. The etching was done in an argon ion beam (500V, 0.5 mA/cm^2) and was timed by etching to clear a glass monitor that was half-covered with a chromium film evaporated at the same time as the wafer.

3.1-4 Reactive Ion Etching

The reason for going to all the trouble to create the grating in chromium is that it served as an etch mask for reactive ion etching the surface relief structure into the SiO_2. RIE proved to be an ideal technique for this work since it is a directional etch which produces very smooth, vertical sidewalls in the SiO_2 (Lehmann and Widmer, 1978). Although the mechanism in RIE is not completely understood, it is believed that the reactive gas (which was CHF_3 at a pressure of 10^{-2} torr in this case) combines with the silicon blasted from the surface by the rf plasma, thereby preventing it from redepositing on the sidewalls. RIE rates have been well-characterized by the submicrometer group at Lincoln Labs. When the wafer had been reactive-ion-etched to the desired depth, the chromium mask was then removed in Kodak chromium etch (43 ml. of conc. perchloric acid, 164.5 gms of ceric ammonium nitrate, and DI water to make 1 liter).

3.1-5 Formation of Wires

Once the square wave pattern was etched into the SiO_2, the wires were fabricated by evaporating a metal film onto the wafer at a very

shallow angle, θ. This was accomplished in a standard electron beam (e-beam) evaporator with a stage that could be rotated with respect to the metal source. The evaporated metal film piled up on one edge of the steps, *forming the wires, and* the excess metal on the tops and bottoms of the steps (thickness = [film thickness] x [tan θ]) was removed with a short IBE at normal incidence.

The advantage of this technique is that the cross-sectional dimensions of the wires are precisely determined by readily-controlled fabrication parameters. The thickness of the wires is determined by the RIE depth and the width of the wires is determined by the thickness of the evaporated film (which was accurately measured by a calibrated Inficon model XTM quartz crystal digital thickness monitor) and the shadowing angle, θ. Because of the extremely smooth sidewalls which are produced in SiO_2 with RIE, it is possible to make simple structures with <100Å linewidths. The shadowing technique is well suited to fabricating arrays of parallel wires, and provided us with a reasonable yield of continuous wires on each wafer. This had the added benefit that the resistance of each sample was in a convenient range for measurement, ~100 to 10,000 ohms. Furthermore, the technique was easily adapted to fabricate single wire samples by using a rectangle pattern (instead of a grating pattern) to produce a single step edge which was then shadowed with metal.

Another advantage of this technique is that we were able to fabricate wires of different cross-sectional areas in the same evaporation. This was done by varying the RIE depth for each array on

the same wafer. Since it was otherwise difficult to obtain the same film resistivity from evaporation to evaporation, this provided a way of studying the area dependence of the effect independent of at least one variable. In addition, we always evaporated a thin film strip at normal incidence to serve as a reference.

3.1-6 Contact Pads

We experimented with several different schemes for making contact to the samples. At first, we did an additional lithographic step after the fabrication of the wires and formed the contact pads by lift-off. Since this step was potentially adding a layer of organic contamination between the wires and the contact pads, we switched to an evaporation through a stencil mask to form the two pads. Additional concern about native oxides prompted us to change to a four-contact arrangement for the stencil mask. Contact pads were evaporated onto the sample and the reference film at the same time.

A completed wafer is shown in Fig. 3.5 next to the brass stencil which was used to fabricate the contact pads. There are four arrays on each wafer with 100 parallel wires in each array. Although the wires are not visible, they are easily located by the diffraction pattern from the surface relief structure. The wires are 4mm long from end to end and stretch between the two outer (current) probes. The segment of the wires which was actually measured was that between the two inner (voltage) probes, and its length varied from ~520 to ~1020 μm depending on the specific pad arrangement that was used.

Fig. 3.5: Completed 1 1/2" wafer with four wire samples next to the brass stencil that was used to form the contact pads. The wires are too small to be visible, but they stretch between the two outer oblong contact pads on each sample. The two inner pads are voltage leads.

3.2 TEM Window Fabrication

It is clear from the graininess of the SEM micrograph in Fig. 3.3 that the SEM just does not have enough resolution to examine structures with <500Å linewidths. Additional resolution is sometimes obtained by coating structures with a thin layer of gold, but that would ruin our samples. In order to verify the dimensions and integrity of our wires, we needed to use a high resolution transmission electron microscope (TEM). Unfortunately, with a TEM there is a trade-off between total sample thickness and resolution. Therefore, we developed a convenient and reliable technique for thinning the substrate which allowed us to nondestructively examine samples in a TEM.

The steps involved in the fabrication of these TEM samples are outlined in Fig. 3.6. If the silicon wafer substrate was chosen to have the (100) orientation, then a potassium hydroxide (KOH) solution could be used to etch an array of four "window" patterns into the bottom side of the wafer. A plan view of this pattern is drawn schematically in Fig. 3.7. Each window consists of a frame surrounding a membrane, as shown in the cut-away view. The etching serves to simultaneously thin the silicon under the membrane to allow TEM observation and the silicon around each frame to allow separation of the individual windows from the wafer. Using the KOH solution, the pattern was etched to within ~10μm of a silicon nitride (Si_3N_4) layer which was deposited on the top side

FABRICATION OF TEM WINDOWS

SiO$_2$
Si$_3$N$_4$
Si
Si$_3$N$_4$

PATTERN BACK

ETCH ANISOTROPICALLY
IN KOH

FABRICATE STRUCTURES

REMOVE WINDOWS

ETCH ISOTROPICALLY
IN HF/ HNO$_3$
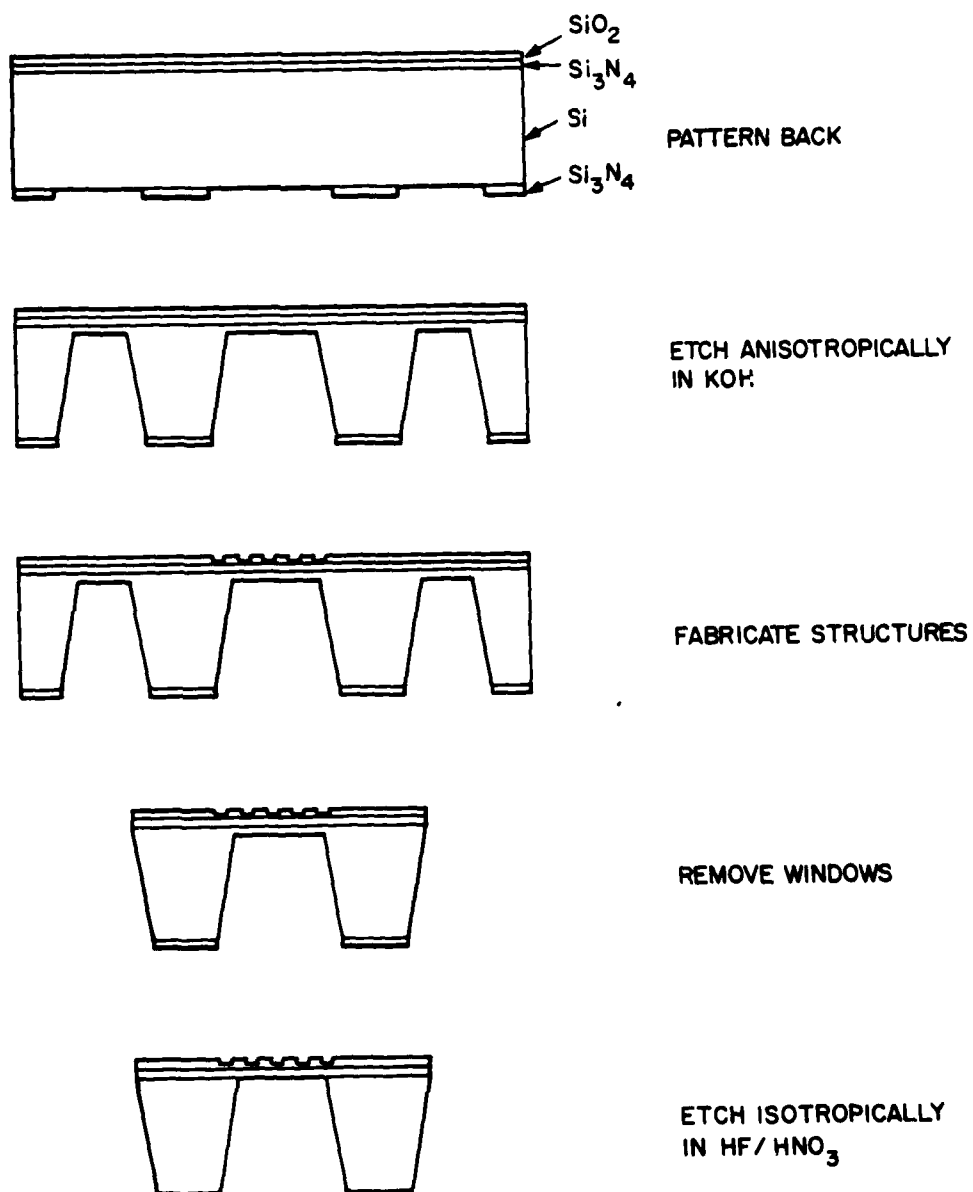
Fig. 3.6:   Fabrication sequence for a single TEM window, viewed from
the side. During the first three steps, the window is
still part of a wafer; then, it is removed and the etching
is completed.

THIN WIRE ARRAYS

FRONT SIDE

BACK SIDE

CONTACT PADS

THIN WIRES

ELECTRON TRANSPARENT
MEMBRANE

SILICON FRAME
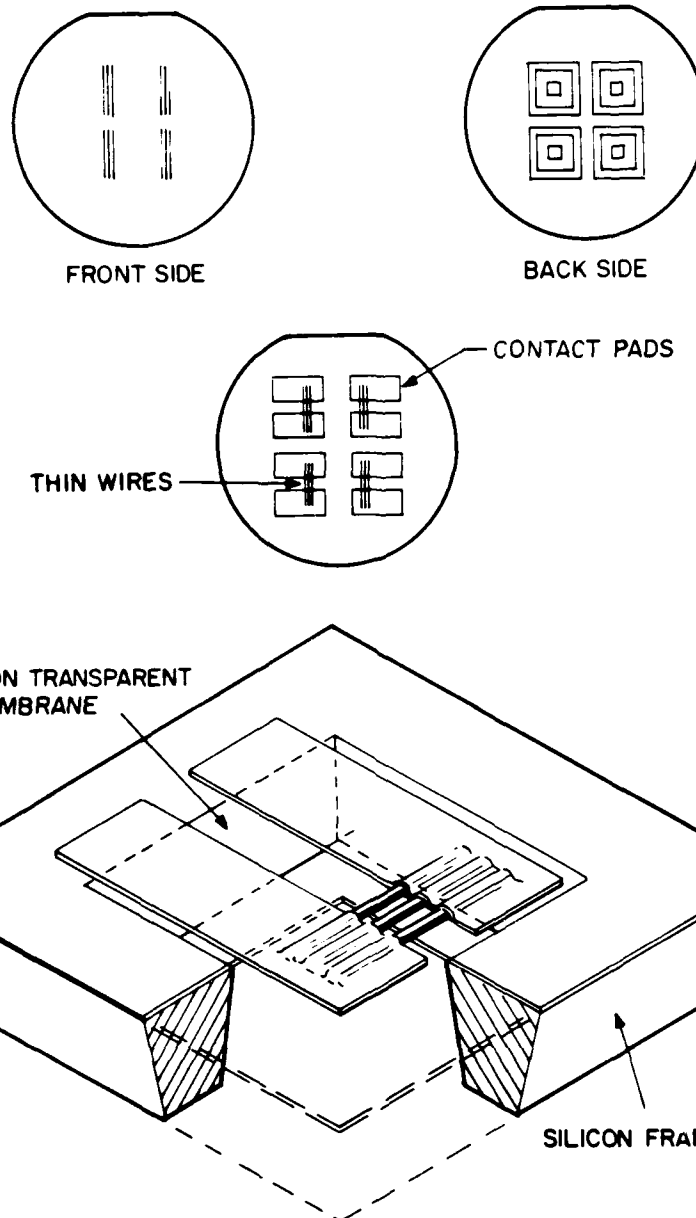
Fig. 3.7: Substrate configuration used in fabricating the TEM
windows. The four window patterns are anisotropically
etched into the back side of a silicon wafer and the
samples are fabricated on the front side so that the wires
fall directly over the window membranes. This alignment is
illustrated in the cut-away view of a completed TEM window,
showing the silicon frame, the SiO_2 membrane, and the wire
sample.

of the wafer. At this point, the substrate had sufficient strength to allow fabrication of structures on the top side but was thin enough to allow easy removal of a window for further thinning and examining in the TEM. The details of the fabrication are given in the following sections.

3.2-1 Substrate Patterning

Once a clean wafer in the (100) orientation was obtained, the next step in the fabrication of the TEM windows was to lay down and pattern the Si_3N_4 and SiO_2 layers. First, a 1000Å layer of Si_3N_4 was deposited on both sides of the wafer using low pressure chemical vapor deposition (LPCVD). Then a 4000Å layer of SiO_2 was deposited on the unpolished bottom side and a 1000Å layer of SiO_2 was deposited on the polished top side by regular chemical vapor deposition (CVD). The layers on the top side eventually served as the membrane, while the layers on the bottom side were needed for etch stops. Next, a pattern with four windows was transferred to a layer of photoresist (4 μm thick Shipley AZ1350J) on the bottom side of the wafer using the contact printing technique described in section 3.1-3. The mask was carefully placed so the straight edges of the windows were aligned with the <100> direction in the plane of the wafer. In order to expose the silicon around the window frames and under the membranes for thinning, the bottom side of the wafer was reactive-ion-etched in CF_4 gas. Both the Si_3N_4 and photoresist are RIE masks for silicon, and the SiO_2 layer was used as a precaution in case there were pinholes in the Si_3N_4 or in the resist.

3.2-2 Anisotropic Etching

An anisotropic etch was used to thin the silicon around the window frames and under the membranes. After the silicon to be thinned was exposed with RIE, the wafer was placed in a solution of 30 gms of KOH per 70 ml. of DI water at $80^{\circ}C$. KOH etches the $\{111\}$ planes of silicon 200 times slower than the $\{100\}$ planes. This produces nice smooth facets at well-defined angles for the membrane frames. Although Si_3N_4 is an etch stop for KOH, SiO_2 is not, so we used a vacuum holder to protect the top side of the wafer from the etchant. This is shown in Fig. 3.8(a). The wafer was placed, top side down, on top of two viton O-rings (from Irving B. Moore Corp.) which were found to resist the etch for several hours. One tube from the center of the holder kept the membrane areas at atmospheric pressure (any suction would have destroyed them), while the other tube was connected to a vacuum which formed a seal between the wafer and the O-rings (Fig. 3.8(b)). We found that the KOH slowly attacked conventional soda lime glass, so we had the holders made of Pyrex.

The KOH etching proceeded very slowly and fairly uniformly, taking approximately three hours. We removed the wafer when the silicon around the window frames and under the membranes was thinned to the point that it looked red in transmission with a fiber light. At this stage, the silicon in these areas was only about $10\,\mu m$ thick and the windows could be easily removed with a pair of tweezers. However, the partially bottom-etched wafer was strong enough to allow microstructure

(a) KOH ETCHING HOLDER

TOP VIEW

SIDE VIEW

(b) ETCHING IN KOH

VACUUM LINE

VACUUM

AIR

SILICON
WAFER

KOH
SOLUTION

PYREX BEAKER
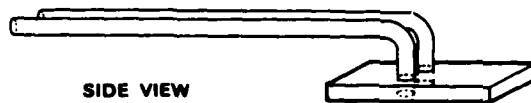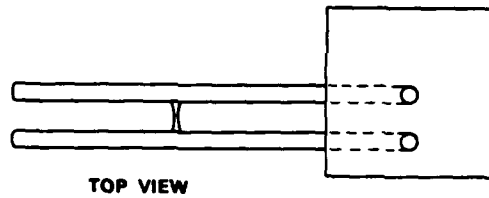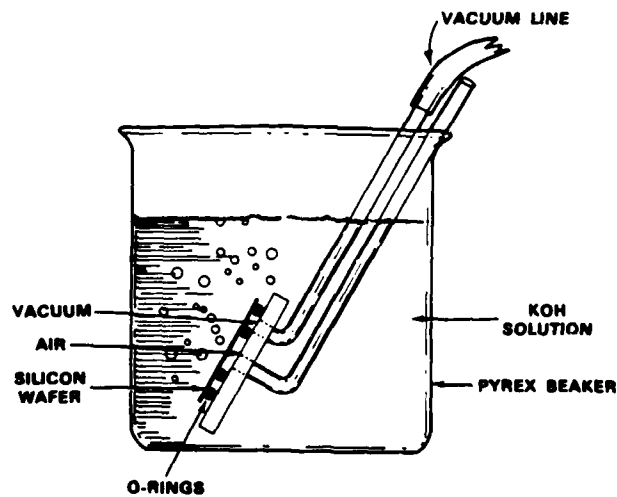
O-RINGS

Fig. 3.8:   (a) Pyrex etching holder for a silicon wafer to use in the
anisotropic etching step in the fabrication of TEM windows.
(b) Schematic of the KOH etching of TEM windows, showing
the etching holder, the double O-ring seal, and the vacuum
arrangement.

fabrication on the top side. Fig. 3.9 is a photograph of the bottom side of a partially bottom-etched wafer with four windows.

3.2-3 Microstructure Fabrication

Next, four wire arrays were fabricated on the top side of the wafer using the basic shadowing technique described in section 3.1. To accomplish the lithography, it was necessary to design a new chuck for the photoresist spinner since the standard chuck exerted too much suction on the membranes. Another double O-ring scheme was used, so the center of the wafer with the membranes was maintained at atmospheric pressure while the vacuum was applied at the perimeter. A photograph of this chuck is shown in Fig. 3.10.

3.2-4 Isotropic Etching

When the sample fabrication was completed, the windows were removed by gently poking several holes through the thin layer of silicon outside the frames with sharp tweezers. Then, the remaining silicon layer was removed from each window individually. This was done in a (96%) hydrofluoric/(4%) nitric acid (HF/HNO_3) etch using a specially designed holder. A cross-sectional view of the cylindrical etching holder is shown in Fig. 3.11. It was constructed entirely of an easily machinable plastic called Vespel, which resists the HF/HNO_3 etch. The window was placed on a custom-made gasket of RTV-21 silicone rubber. When the top of the holder was screwed down, a seal formed around the top side of the window, protecting the wires from the etchant. The HF/HNO_3 etch was
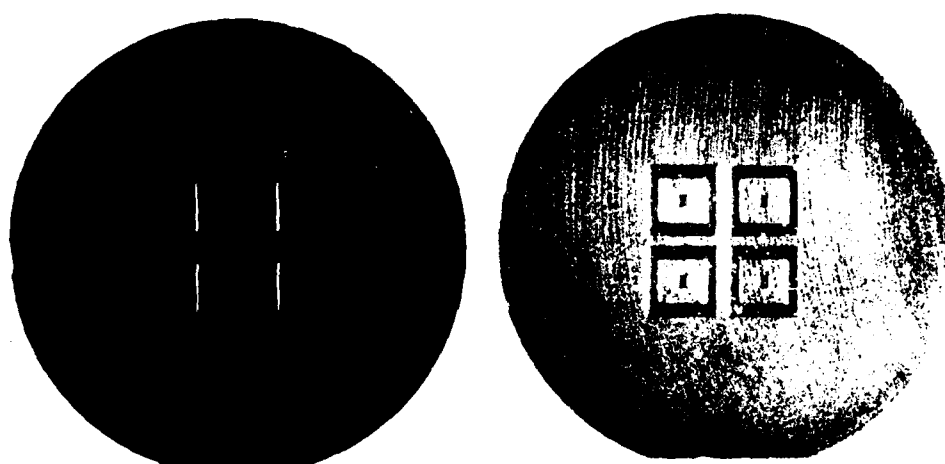
Fig. 3.9: Two views of a partially bottom-etched 1 1/2" wafer showing
the four window patterns on the bottom (right side) and the
four wire samples on the top (left side). Although the
actual wires are not visible, the rectangular areas where
the 4 μm period gratings are located can be seen in the
left view.
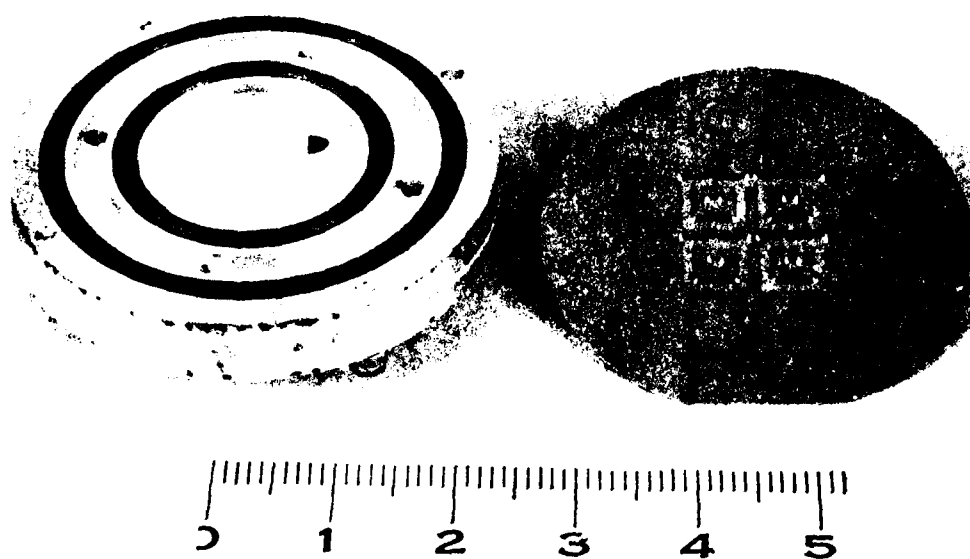
Fig. 3.10: Photoresist spinner chuck for a partially bottom-etched wafer, next to a centimeter rule. The double O-ring seal isolates the fragile membranes from the vacuum hold-down.

TEM WINDOW ETCHING HOLDER

VESPEL

RTV-21 GASKET

SAMPLE

HF / HNO$_3$ ETCHANT
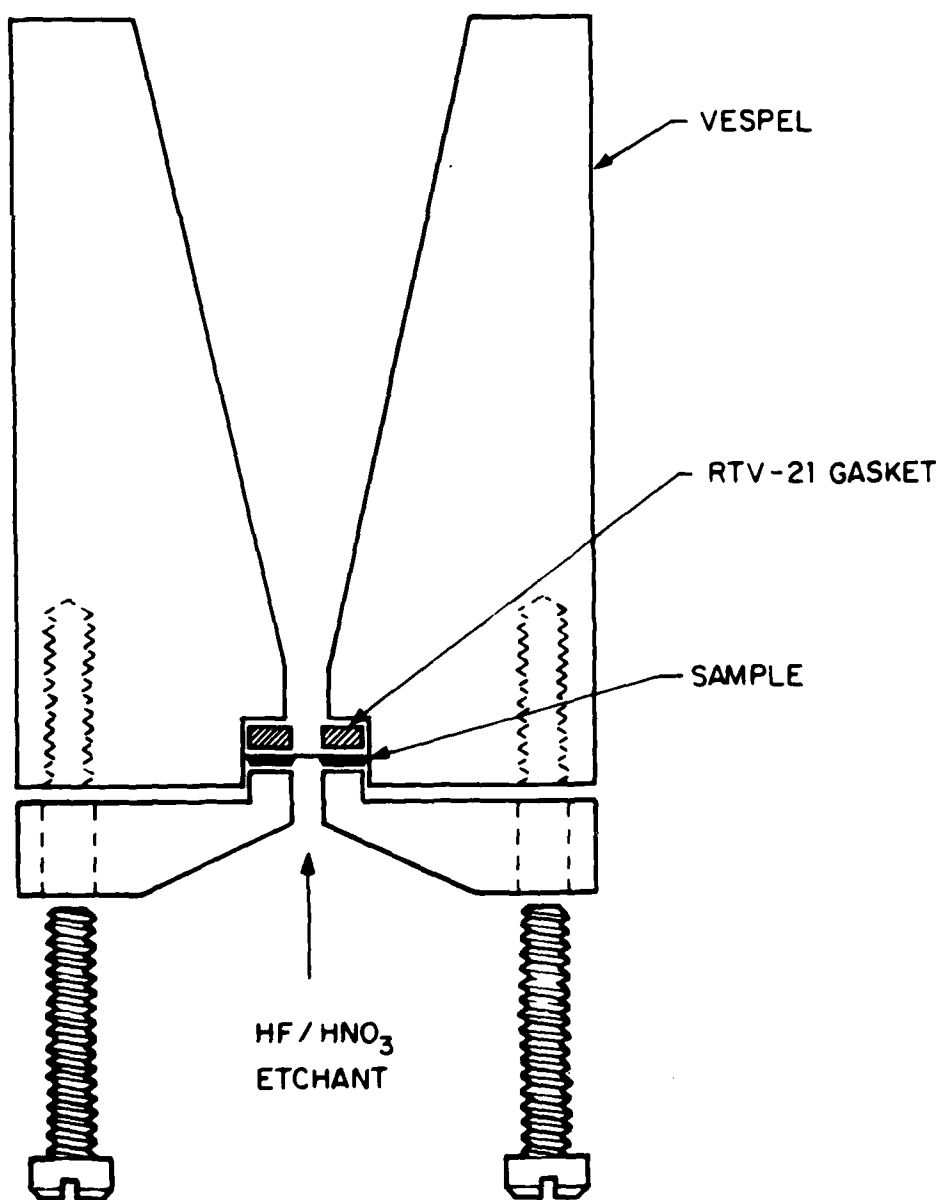
Fig. 3.11: Cross-sectional view of the holder for completing the etching of a TEM window. The window is placed inside the body of the holder on top of a custom-made silicone rubber gasket. When the top is screwed down, a seal forms around the membrane, protecting the microstructures on the top side. The etchant is squirted onto the bottom side of the wafer through the hole in the top of the holder, and the etching can be viewed through the back of the holder.

squirted onto the bottom side of the window using a Teflon eye dropper and the etching progress was visually monitored. As soon as the membrane became transparent, indicating that the silicon was completely gone, the etching was halted with the addition of water.

The actual etching holder is shown in Fig. 3.12 next to a centimeter rule. Even the screws are made of Vespel. Fig. 3.13 shows both sides of a completed TEM window. The silicon frame is 4mm on a side and the membrane itself is 3/4mm x 3/4mm. The membrane in the photograph is <2000Å thick. After the final etching, the windows were bonded to a specially machined brass piece with black wax (Fig. 3.14). This was compatible with the TEM and provided a convenient holder for handling the window during any subsequent processing.

3.2-5 TEM Observation

Using the shadowing technique, we produced parallel arrays of ultrathin metal wires for observation in the TEM. First, the wires were fabricated on a partially bottom-etched wafer and contact pads were deposited using either stencil or lift-off techniques. The masks were designed so that when they were aligned with the wafer flat, each wire array fell over a TEM membrane. When the samples were completed, the windows were removed and the remaining silicon was etched away. A cut-away diagram of a completed window is shown in Fig. 3.7.

Fig. 3.15 shows a TEM micrograph of such a sample. This is an array of 300Å x 300Å nickel wires on a ~4μm period square wave surface

Fig. 3.12: Photograph of an actual KOH etching holder next to a centimeter rule. The holder is made of Vespel plastic. Also shown are a gasket, a TEM window, and the Vespel screws.

Fig. 3.13: Top and bottom views of a completed TEM window. The silicon frame is 4mm on a side and the membrane, which is less than 2000Å thick, is 3/4mm on a side.
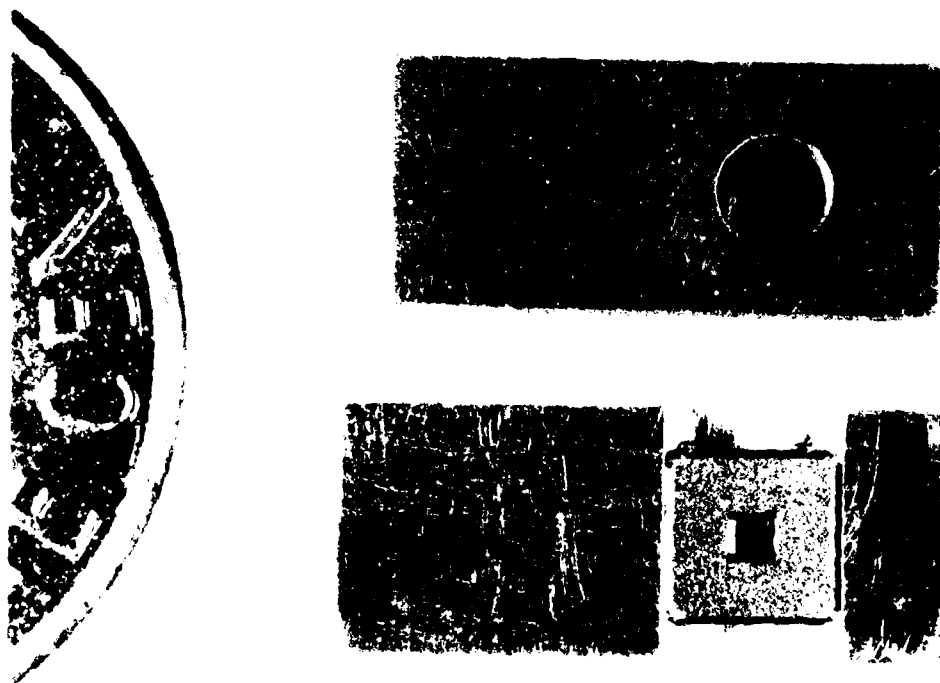
Fig. 3.14: Completed TEM windows mounted in brass holders for observing in the TEM.
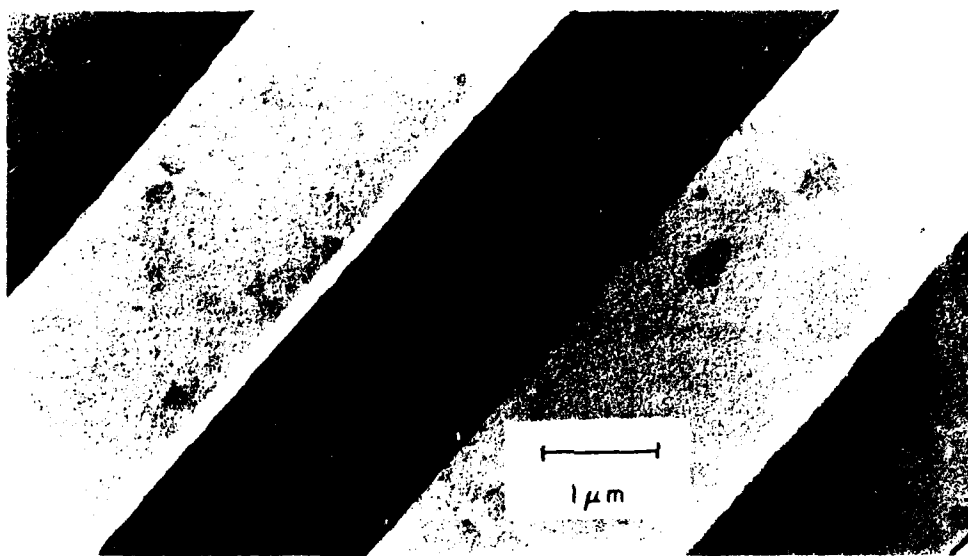
Fig. 3.15: TEM micrograph of a nickel wire array fabricated using the
shadowing technique. The 300Å x 300Å nickel wires are the
black lines following the step edges. The grating in SiO_2
has a 3.81 μm period and the tops of the steps appear
slightly darker than the bottoms because of the additional
thickness of SiO_2. The white bands running along the
opposite step edges from the wires are the "shadows" of the
steps resulting from the nickel evaporation.

relief structure. The wires are the dark lines running along the step edges. The mottled area, which appears slightly darker on the top of the step because of the additional thickness of SiO_2, is the imprint of the very thin layer of nickel which ended up on the horizontal surfaces of the wafer and was subsequently ion-beam-etched. A wire from the same array is shown in a more magnified view in Fig. 3.16. In this TEM micrograph, the top of the step is on the right, the wire follows the step edge, and the bottom of the step is on the left. The grain size in the nickel appears to be about 60Å. Using the TEM, we were able to verify the width of representative wires and found them to be extremely uniform over hundreds of microns of length.

3.3 Material Considerations

In making the choice of metal for the wires, we had decided early on to try a pure metal rather than an alloy in order to investigate whether or not the effect depended on some intrinsic property of alloys. At that point, resistance rises had only been observed in AuPd and WRe alloys. Since the size of the resistance rise was predicted to vary inversely with resistivity, we started searching for a relatively high resistivity metal. In addition, we decided not to study metals that had a superconducting transition close to $1.5^\circ K$ in order to eliminate complications due to superconducting fluctuations above the critical temperature.
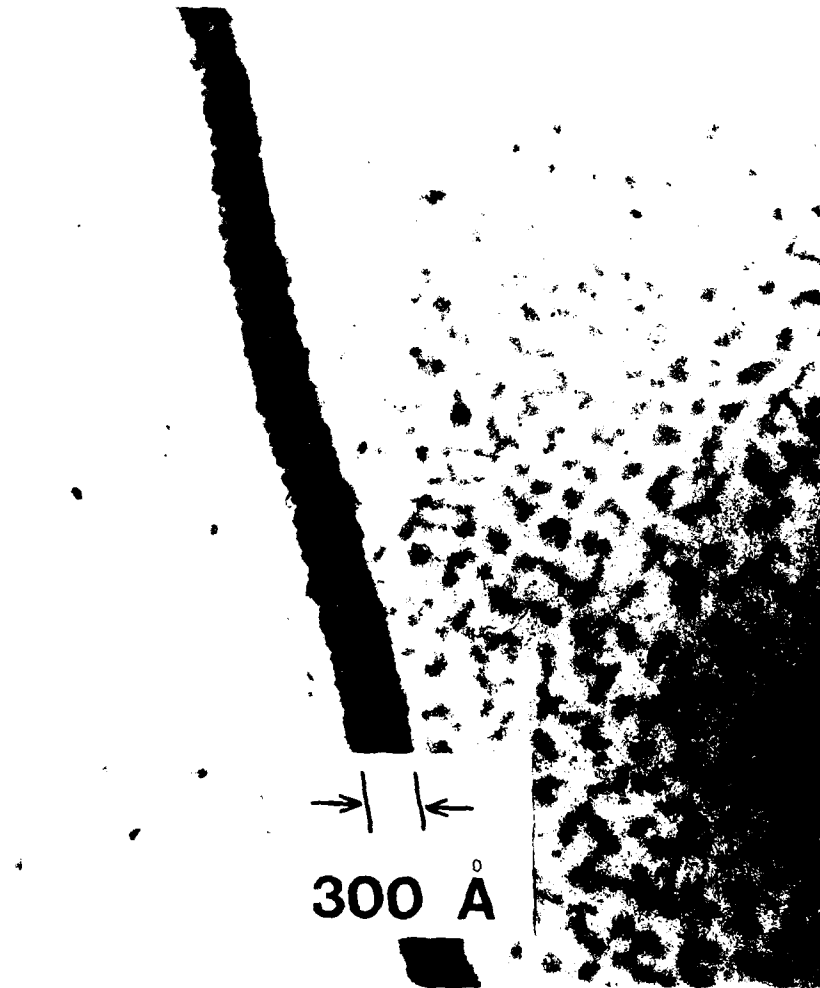
Fig. 3.16: Higher magnification TEM micrograph of a 300Å x 300Å nickel wire from the array shown in Fig. 3.15. The mottled appearance of the area surrounding the wire results from nonuniformities in the extraneous nickel layer on the tops and bottoms of the steps which were transferred into the SiO_2 during IBE.

The fabrication criteria for choosing the metal were three-fold:

1. It should adhere well to the SiO_2 substrate.

2. It should not readily oxidize, in order to avoid electrical contact problems.

3. It should have a small grain size ($<100\text{Å}$) since we planned to make wires with $<1000\text{Å}$ linewidths.

Unfortunately, it turns out that those metals which adhere well to oxide substrates are also the metals which readily oxidize (Williams and Backus, 1949), so there is a trade-off implied between the first two criteria. It was relatively easy to meet the third criterion since, in most metals, the grain size is greatly influenced by the evaporation environment: the substrate temperature, the residual gas pressure, and the rate of evaporation.

We were not able to vary the substrate temperature, but we were able to study the effect of residual gas pressure and evaporation rate on grain size using the TEM. TEM windows which were prepared in a manner similar to that described in section 3.2 proved to be ideal for studying grain size. The only difference in the fabrication of these windows was that the anisotropic bottom-etching in KOH was allowed to continue to completion at the Si_3N_4 layer (which is an excellent etch stop for KOH). This considerably simplified the process and we were

able to generate large numbers of blank membranes with very little

effort. These were stored and transported in a plastic container with a

tightly clamped cover (available from Fluoroware, Inc.) that had

convenient ~4mm x 4mm compartments. Shallow dimples were drilled in the

cover above each compartment so the membrane would never come in contact

with the plastic (it was protected on the back side by the silicon

frame). In this way, we had very little problem with breakage of these

fragile, <2000Å thick membranes.

When we wished to study a particular metal, a window was mounted in

a brass TEM holder and the holder was fastened in place in the

evaporator. In some cases, a piece of mylar was stretched over part of

the membrane as a mask. Because of diffraction-like effects, the

resulting film did not have a sharp edge. Instead, we were able to see

a continuous transition from zero thickness to total film thickness.

3.3-1 Aluminum

It is well known that the grain size and resistivity of aluminum

can be varied over several orders of magnitude by changing the partial

pressure of oxygen present in the evaporator during the evaporation and

by changing the evaporation rate (Deutscher et al., 1973). We

systematically studied the relationship between grain size, evaporation

rate and oxygen pressure in thin films of aluminum. Aluminum wets most

materials readily and tends to creep out of containers, so the aluminum

films were evaporated from tungsten wire baskets. Representative films

are shown in Fig. 3.17 and the data is summarized in Table 3.1. These films also exhibited different superconducting transition temperatures. In the end, we decided not to use aluminum for our wires because of the superconducting transition.

3.3-2 Tungsten and Tantalum

Tungsten seemed as if it might be another another promising candidate for the metal wires. Although tungsten reaches evaporation vapor pressure ($\sim 10^{-2}$ torr) at a very high temperature, $\sim 3230^{\circ}C$, it was possible to evaporate films without too much difficulty using the e-beam evaporator. The tungsten films were found to have an extremely small grain size and to adhere very well to SiO_2. We were able to attain reasonable resistivities for the tungsten films by evaporating at low pressures to inhibit oxide formation. However, these films exhibited a (strain-enhanced) superconducting transition at $\sim 3^{\circ}K$. In addition, we learned (painfully) that tungsten is attacked by the AZ developer. This meant that any exposed portions of the tungsten wires would disappear in subsequent photolithographic steps (for instance, contact pad definition).

After discovering that tantalum films had a small grain size also, we made very thin, uniform wires with tantalum as shown in Fig. 3.18. Like tungsten, tantalum only reaches evaporation vapor pressure at $\sim 3000^{\circ}C$, but we were able to produce good quality films using the e-beam evaporator. Again, because of the superconducting transition at $\sim 3^{\circ}K$ (which is lower than the nominal T_c of tantalum, probably because of
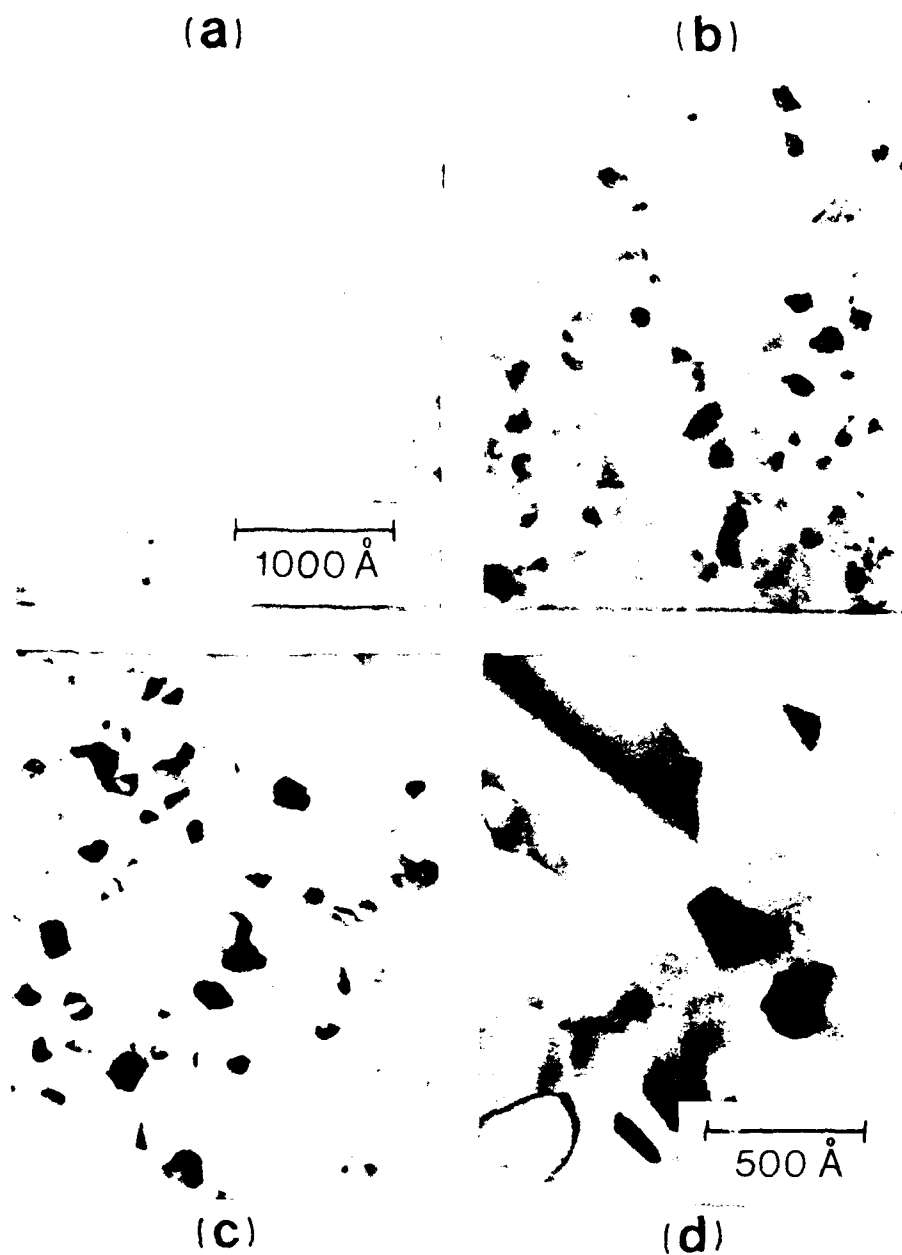
Fig. 3.17: TEM micrographs of three thin films of aluminum evaporated
at different rates and with different partial pressures.
The fabrication parameters are summarized in Table 3.1.
(d) is a magnified version of the film in (c).

Table 3.1: Grain Size and T_c for Aluminum Films

film	evap. rate (Å/sec)	pressure (torr)	T_c (°K)	grain size	ρ_{LT} (μohm-cm)
	25	1.6×10^{-5}	not meas.	600Å	
	2.7	7.5×10^{-6}	<1.45		
	2.1	2.0×10^{-5}	1.52-1.98		
(b)	2.0	9.4×10^{-6}	1.52-1.58	250Å	17
(a)	2.8	2.0×10^{-5}	1.8-1.9	200Å	58
(c)	19.4	2.0×10^{-5}	1.52-1.58	300Å	9
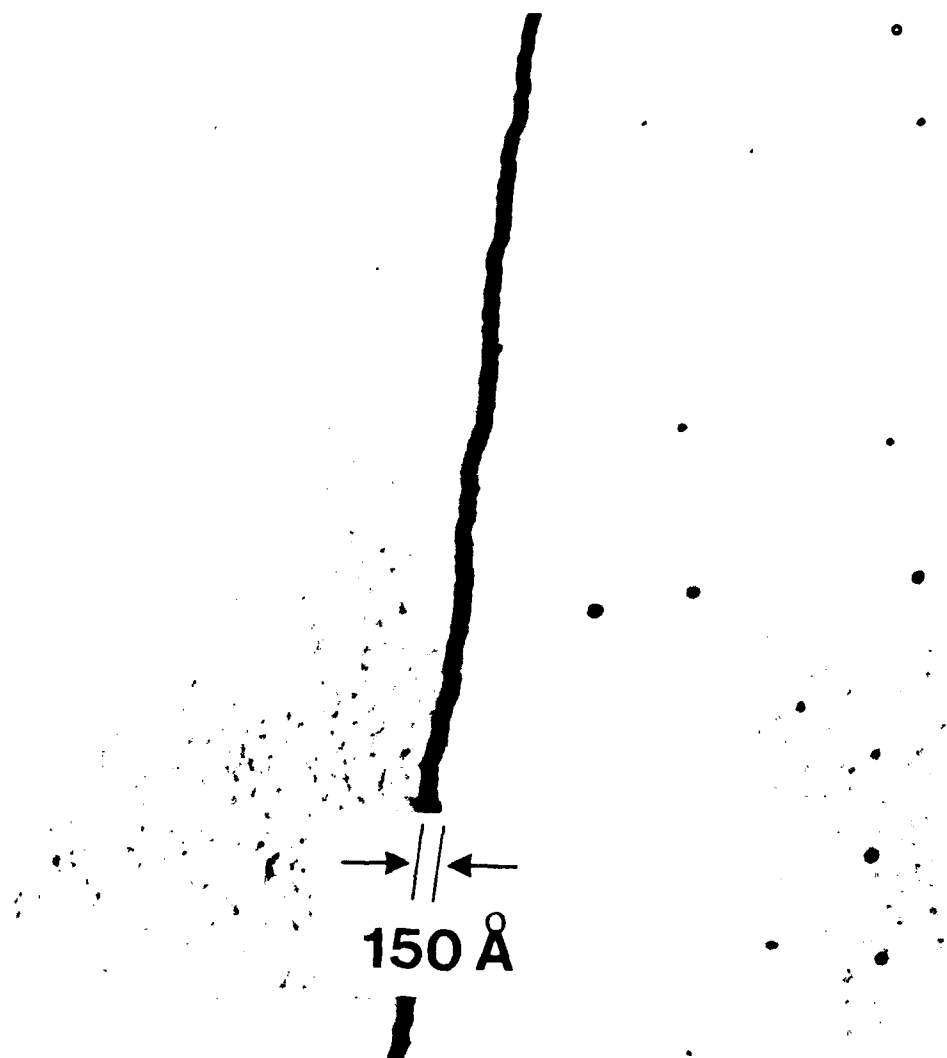
Fig. 3.18: TEM micrograph of a 150Å wide tantalum wire fabricated
using the shadowing technique. The small nonuniformities
in the SiO_2 at the bottom of the step are highlighted by
tantalum.

oxide formation and other impurities), these wires were not useful for
our experiment; however, they are potentially useful for studies of
one-dimensional superconductors.

3.3-3 Nickel

Next, nickel was investigated as it seemed to have properties that
represented a reasonable compromise between the competing
considerations. It was expected to have medium adhesion to SiO_2 and to
exhibit only medium oxide formation tendencies. The nickel was
evaporated from a graphite crucible in the e-beam evaporator and the
evaporations proceeded without difficulty. The resistivities of the
nickel films were not very sensitive to the residual gas pressure in the
evaporator, varying only by a factor of ~2. We found that the films
held up well under additional processing and repeated cycling to liquid
helium temperatures. Judging from TEM micrographs of the wires (see
Fig. 3.16), the grain size appeared to be <60Å.

The ferromagnetic properties of nickel insured that
superconductivity was not a problem, but the effect of a small magnetic
field on these samples was pronounced. A selection of some of the
resistance versus magnetic field data for the nickel samples is given in
Appendix B. Although the negative magnetoresistance we observed is a
hallmark of the localization theory, it was clear that the magnetic
field-induced resistance changes in the nickel samples were due to the
bulk ferromagnetic properties because they were orders of magnitude
larger that any zero field resistance change. Furthermore, we

discovered that we could "tune" the low temperature resistance rise in
these samples by varying a small (<10 kilogauss) applied magnetic field.
This implied that the remnant field in a nickel sample would also have
an effect on the size of the low temperature resistance rise at zero
magnetic field. Since the remnant field depended on the magnetic field
history in an unknown way, we decided to only analyze data from nickel
samples that had never been placed in a magnetic field and to search for
materials that would have more reproducible behavior.

3.3-4 Copper

At this point, we tried making wires with copper and had
considerable success. We used 99.9999% pure copper from United Mineral
and Chemical Corp. and evaporated it from a molybdenum crucible in the
e-beam evaporator. The resistivity of the copper films depended
strongly on the residual gas pressure in the evaporator which we
attributed to oxide formation, so we flushed the evaporator with
nitrogen gas and evaporated at low pressures ($\sim 10^{-7}$ torr) to minimize
this consideration. We do not know much about the thickness of the
copper oxide on the surface of the films, but we can infer from TEM
pictures that the oxide is only a small percentage of the material in
the film.

Because of the suggestion by Raffy et al. (1982) that thin copper
films were found to have cracks, we studied a copper film deposited on a
membrane in the manner described earlier. This allowed us to follow
continuously the growth process in this film without the necessity of

interrupting the evaporation. What we observed illustrated beautifully the general features of classic thin film growth. These are shown schematically in Fig. 3.19 and are discussed in detail by Chopra (1969) and Maissel and Glang (1970). Briefly, it has been found that on a variety of (usually amorphous) substrate materials with a variety of deposition techniques (evaporation, sputtering, etc.), thin film growth proceeds via distinct stages. First, small nuclei or islands which are randomly oriented and randomly distributed appear on the substrate. As the film thickness increases, the nuclei grow in size, sometimes favoring a particular crystallographic orientation. When the small islands grow close enough together, coalescence takes place so as to minimize the surface free energy. In this stage, there is a tendency for the larger, composite island to assume a single crystallographic orientation. As the islands continue to grow and merge, they form a "network" which is a more or less continuous film with oddly-shaped channels. Presumably these are the cracks to which Raffy et al. (1982) referred. At this stage, the crystalline orientations are frozen in and, in thicker films, the small nuclei in the channels tend to grow and fill in the holes. If the film reaches the network stage while the islands are still small (as is often the case when the substrate is held at a reduced temperature), the resulting film will tend to be small-grained polycrystalline or even amorphous; whereas, if the islands grow quite large before coalescing (as is the case at high substrate temperatures since the nucleation rate is slow and the surface mobility is high), the resulting film is usually large-grained polycrystalline.
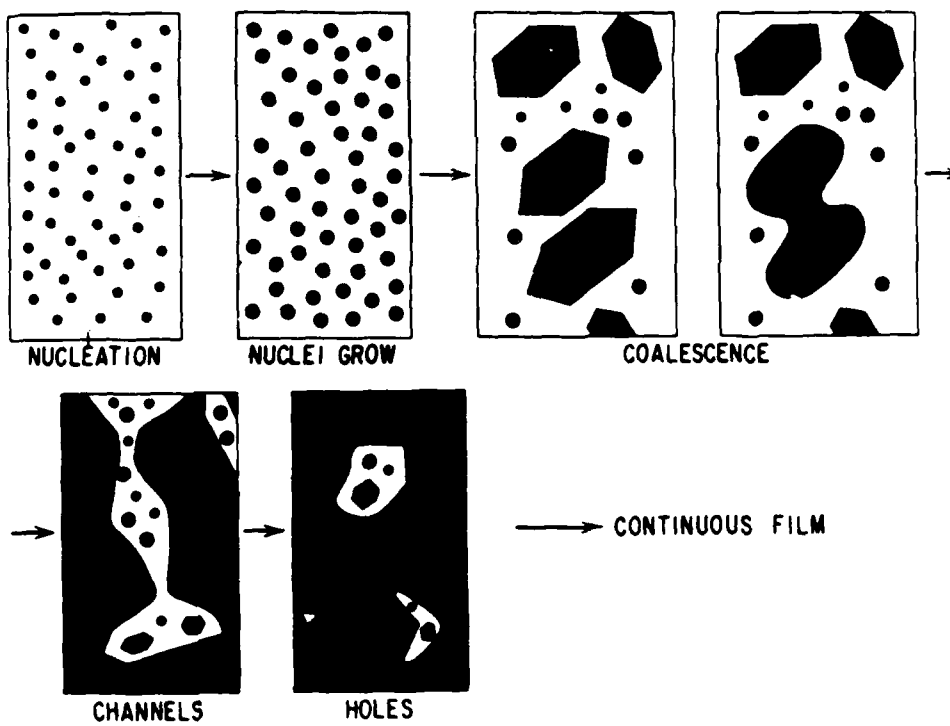
Fig. 3.19: Schematic of the stages of thin film nucleation and growth (from Maissel and Glang, 1970).

A TEM micrograph of the network stage (close to the edge) of our copper film is shown in Fig. 3.20(a). The islands are approximately 100-300Å in diameter and the channels are clearly discernible. In contrast, a micrograph from an area of the film which is the full 220Å deep (Fig. 3.20(b)) shows that the film is completely continuous and strikingly polycrystalline. The grain size appears to vary considerably from 40Å to 300Å. While studying this film in the TEM, we occasionally came across much larger grains, but they represented a small percentage of the overall coverage.

3.3-5 AuPd Alloy

We also studied films and wires of 60 at.% Au - 40 at.% Pd ($Au_{60}Pd_{40}$) alloy, following the idea of Dolan and Osheroff (1979) and Giordano, Gilson, and Prober (1979). AuPd alloy has several desirable material characteristics for this work. Specifically, it is expected to oxidize slowly and to have extremely small grain size. In addition, it has a high residual resistivity because it is an alloy. Our AuPd samples were evaporated from a resistance-heated alumina-coated boat into which were placed the pr̪er relative amounts of gold and palladium. After heating the metals to the boiling point and allowing adequate time for them to mix, the shutter was opened and the film was evaporated. Since gold reaches evaporation vapor pressures slightly before palladium as the temperature is raised ($1400°C$ versus $1460°C$), the film composition was probably close to that of the ingot but perhaps a little gold-rich. Considerable care was necessary in subsequent steps
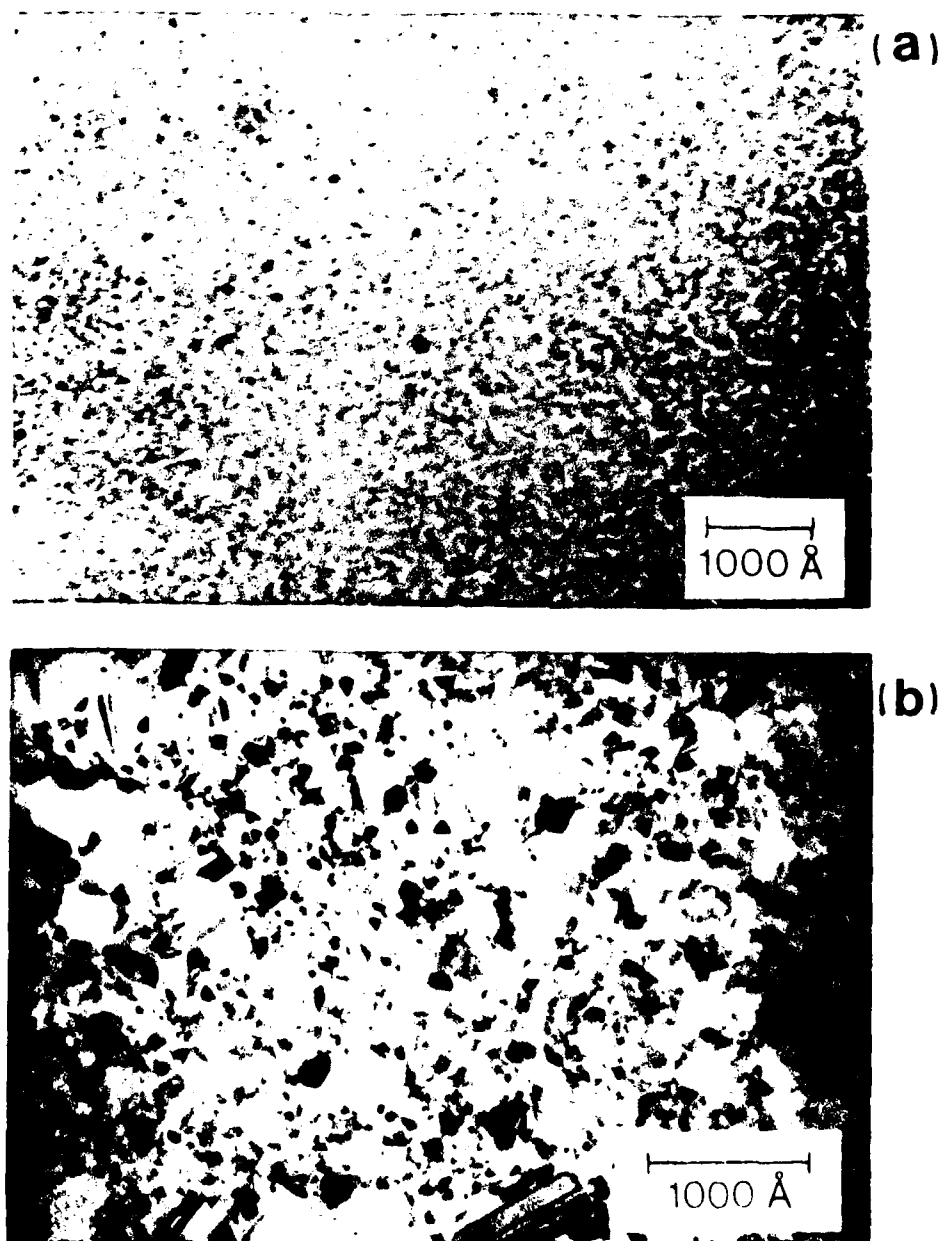
Fig. 3.20: TEM micrograph of a thin copper film showing (a) the channel stage at ~70Å and (b) the continuous polycrystalline film at 220Å.

in the fabrication since the AuPd alloy did not adhere well to the

substrate. Any ultrasonic agitation was disastrous for these samples

and the smaller wires only cycled to liquid helium temperature a few

times before becoming discontinuous. We were able to verify that the

films had small grain size ($\sim 60 \text{Å}$) using the TEM. A typical AuPd alloy

film is shown in Fig. 3.21.
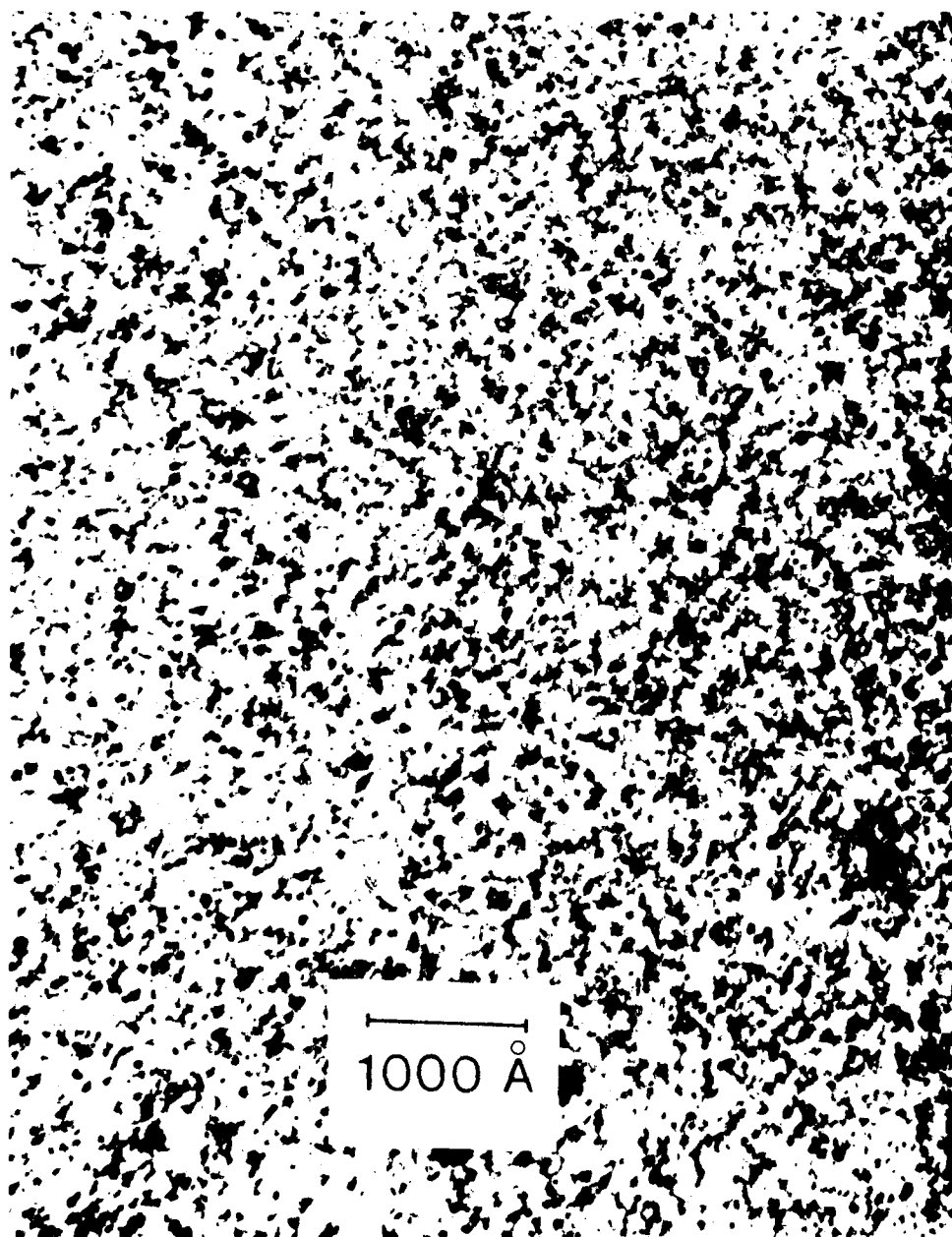
Fig. 3.21: TEM micrograph of a polycrystalline, ~500Å thick AuPd alloy film. The grain size appears to be less than 60Å.

CHAPTER FOUR: EXPERIMENTAL MEASUREMENT TECHNIQUES

Once the ultrathin wire samples had been fabricated, the next step in our experiment was to measure the resistance versus temperature characteristics of the samples at low temperatures. The cryogenic work was done in the laboratory at Harvard. In this chapter, we first discuss the techniques which we used to achieve low temperatures. Then, in the second section, we describe the measurement circuitry which we used to take the data.

4.1 Low Temperature Techniques

When we began this work, we were hoping to see rapidly rising resistances in our samples at low temperatures. Early predictions were that the resistance of a one-dimensional wire might increase as T^{-2} or even exponentially as T^{-1} (Thouless, 1977). Our first experiments were performed with a standard dipstick-style cryostat with the sample directly immersed in the liquid helium bath, but this limited the available temperatures from $4.2°K$ down to $\sim 1.5°K$. With the idea of extending our temperature range below $1.5°K$, we resurrected a charcoal-pumped helium-3 (^{3}He) cryostat that was de'igned and built by W. J. Skocpol. Before long, we discovered that this cryostat was even more useful for extending our temperature range above $4.2°K$, and we used it to take most of our data. Details of the design (including several improvements) and operation of the ^{3}He cryostat are given in section

4.1-1. Unfortunately, the ^{3}He cryostat was too bulky to fit into the narrow-tailed dewar for magnetic field studies. In section 4.1-2, we describe the more conventional cryostat that was used for these measurements. Finally, in section 4.1-3, we briefly discuss the thermometry that was used for our experiments.

4.1-1 Charcoal-Pumped ^{3}He Cryostat

Although the physical properties of ^{3}He and ^{4}He are for the most part very similar, the vapor pressure of ^{3}He at 1.0°K is approximately 2 orders of magnitude larger than that of ^{4}He at the same temperature (White, 1979). This means that if a pressure of 1 mtorr is achieved above a bath of ^{3}He, the temperature of the bath will be 0.65°K as opposed to 1.27°K in ^{4}He. However, ^{3}He is very expensive and only available in small quantities. For these reasons, a closed cycle ^{3}He refrigerator is usually used as a booster on a conventional cryostat to provide an additional stage of cooling between 1.5°K and, in our case, ~0.5°K. The theoretical limit of such a refrigerator is $\underline{c}$. 0.25°K.

The part of the ^{3}He cryostat that was actually immersed in the ^{4}He bath is cylindrical and is shown in cross section in Fig. 4.1. The upper chamber is filled with 200 psi of ^{3}He gas (at room temperature) and is lined with charcoal powder that is held in place with a screen. As the temperature of the charcoal is lowered through thermal contact with the ^{4}He bath, gases are adsorbed on its surface. In the refrigerator, this adsorption is used to exert a pumping force on a

CHARCOAL-PUMPED ^{3}He CRYOSTAT
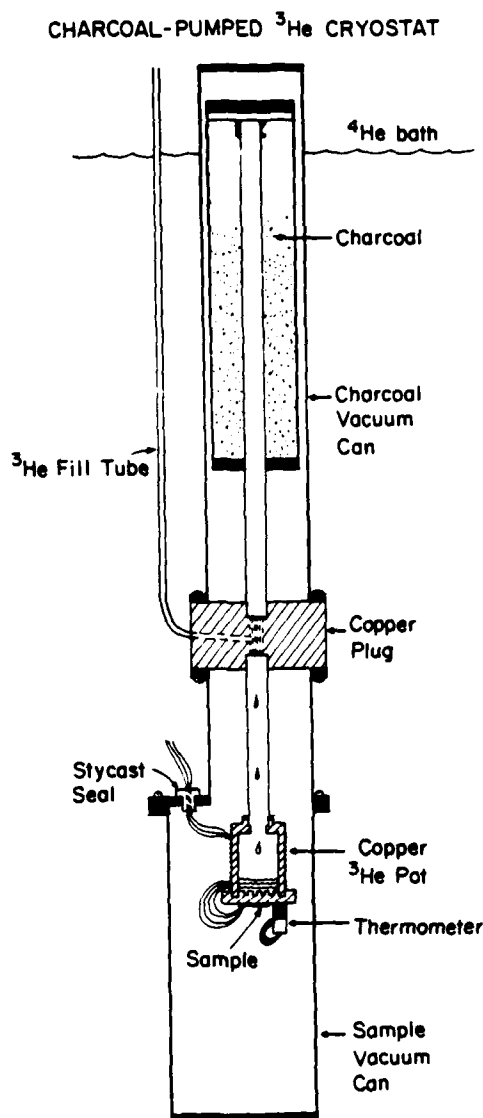
Fig. 4.1: Cross-sectional view of the part of the charcoal-pumped ^{3}He cryostat that is immersed in the ^{4}He bath. When the ^{3}He gas is driven off the surface of the charcoal powder in the upper chamber after the heater is turned on, it comes in contact with the copper plug (which is at the bath temperature), and condenses. The liquid ^{3}He drips down through holes in the plug into the copper sample pot. The sample is attached to the outside of the pot, which is also surrounded by a vacuum can.

small quantity of the liquid ^{3}He. The charcoal chamber is surrounded by a vacuum can and the bottom of the can is in thermal contact with an OFHC (oxygen-free high-conductivity) copper plug which is in turn in thermal contact with the ^{4}He bath. Holes drilled through the plug connect the upper chamber to a stainless steel tube that runs down into a small copper pot. Indentations in the bottom floor of the copper pot serve to increase the surface area and decrease the thermal mass of the copper for better cooling. For resistance measurements, a sample is mounted on the outside of the copper pot close to a germanium resistance thermometer. The entire lower portion of the cryostat is also enclosed in a vacuum can so the temperature of the pot can be raised above or lowered below the bath temperature. The section of the cryostat that contains the ^{3}He is sealed; in fact, the ^{3}He gas has never been replaced.

Three narrow stainless steel tubes (for low thermal conductivity) connect the cylindrical portion of the cryostat to a brass face plate which stays at room temperature. Two of these are pumping lines for the vacuum cans which can be evacuated individually. The third was used for adding ^{3}He gas and was sealed off with a pressure gauge attached. Electrical contacts to the outside world are made through a total of three Canon 10-pin connectors and two Canon 6-pin connectors, all vacuum tight. The lead wires, which are twisted pairs to reduce rf interference, come down through the bath and are soldered onto a central pinboard. From there, shorter, #36 gauge copper wires are brought into the sample chamber through a vacuum-tight, easily replaceable Stycast

2850 GT epoxy seal. These wires are wrapped many times around the copper pot and are thermally anchored with a coat of General Electric (GE) 7031 varnish. The samples were pressed against the underside of the pot with a thin layer of Apiezon N grease in between to improve thermal contact.

Three thermometers and the ^{3}He pressure gauge were used to monitor the operation of the cryostat. The germanium resistance thermometer which measured the sample temperature is encased in a copper sheath which is screwed into the copper pot close to the sample. To insure good thermal contact, the thermometer leads are wrapped tightly around the sheath and held in place with more GE varnish. A second thermometer, this time a carbon resistor, is thermally sunk to the outside of the charcoal can and was used to measure the temperature of the charcoal. The charcoal temperature is also reflected in the pressure of the ^{3}He gas, which can be read on the gauge at the top of the cryostat. A second carbon resistor is attached to the outside of the copper plug with GE varnish. In addition to monitoring the plug temperature, it served as a level detector for the ^{4}He bath.

Once liquid ^{4}He has been transferred into the dewar, the first step in cycling the cryostat to the lowest temperature is to heat the charcoal using a resistor. This drives the ^{3}He gas off the surface of the charcoal into the central tube. There, the gaseous ^{3}He comes into contact with the copper plug, which is at the bath temperature, and condenses (the normal boiling point of the ^{3}He is 3.19°K). Drops of liquid fall through the copper plug and collect in the copper pot. When

most of the gas has condensed, amounting to only a few milliliters of liquid, the charcoal heater is turned off. Since the charcoal is in contact with the plug, it then begins to cool and starts adsorbing ^{3}He gas, lowering the pressure over the ^{3}He bath. Almost immediately, the temperature of the pot drops to $\sim 0.5^\circ$K. Depending on the heat load, it can remain cold for up to an hour. When the pot warms up, this procedure can be repeated for as long as the ^{4}He bath covers the plug. The sample temperature can be stepped between 0.5°K and the bath temperature by heating the charcoal in small increments. This is very unstable, however, and boils off ^{4}He at a great rate. In order to raise the temperature of the sample above the bath temperature, a voltage is applied across a resistor attached to the ^{3}He pot. This proved to be very steady and much more convenient.

The cryostat operation was not always as smooth as just described. Some hints for its operation are given below:

1. In order to minimize heat leaks due gaseous thermal conduction, it is necessary to reduce the pressure in the sample can before precooling. The most convenient way to do this is to seal the can with an indium O-ring and pump it to low pressures (<60 mtorr), first with a roughing pump, then with a diffusion pump. Putting charcoal in the sample can does help reduce the pressure at ^{4}He temperatures because of its adsorbing action; however, at room temperature, it is hard to distinguish the slow outgassing of the charcoal from a leak in the vacuum seal.

2. Unless the cryostat is thoroughly precooled (overnight) with liquid nitrogen (LN_2), it takes several attempts to cycle to the lowest temperatures. The ^{3}He pressure gauge in our rig reads ~ 50 psi at LN_2 temperature.

3. The liquid ^{4}He bath pressure should be below 10mm
   (corresponding to 1.74°K) before the charcoal
   heater is turned on. Then, applying 7 volts
   across the heater (approximately 1 watt) until the
   charcoal thermometer resistance falls below 250 Ω
   usually results in a successful cooldown.

4. If the plug temperature begins to rise while the
   ^{3}He is condensing, it is an indication that the
   ^{4}He bath level has fallen below the plug. At this
   point, if the charcoal heater is not turned off
   immediately, the temperature of the plug and the
   pot will rise.

5. A small amount of ^{4}He exchange gas is needed in
   the charcoal vacuum can to improve the pumping
   speed. This also helps to eliminate the
   temperature oscillations which were often observed
   at the lowest temperatures. These peculiar
   oscillations, which exhibited about a 20 second
   period and a slowly increasing amplitude
   (20-50mK), can perhaps be attributed to additional
   ^{3}He liquid dripping into the pot.

Unfortunately, we had trouble making quantitative measurements
below 1°K using this configuration. The difficulty can be traced to a
combination of rapidly decreasing thermal conductivity in the grease
layer between the substrate and the copper ^{3}He pot and increasing
thermal boundary resistance in general. This problem was analyzed in
detail by Anderson and Peterson (1970), who suggested that the total
thermal bond resistance, R, could be written as a sum of the Kapitza
resistances of the interfaces (r_B) plus the bulk thermal resistance of
the Apiezon N grease:

$$R = 2(r_B) + 1/(KA)$$

where l is the thickness of the grease, A is the substrate area and K is

the thermal conductivity of the grease. Since the grease under the substrate was squeezed out as the sample was pressed onto the pot, 1 was very small, implying that the second term was negligible compared to the first in our situation. Anderson and Peterson found that $r_B \sim A(T^{-3}) + B(T^{-2})$, so the contribution that this term makes to the total thermal resistance increases very rapidly below $1°K$. In addition, Kaplan (1979) has shown that the acoustic mismatch between several superconducting metal films and a glass substrate also leads to a T^{-3} term plus a smaller T^{-2} term in the thermal boundary resistance. As a result, we attached greater weight to the data taken above $1°K$, and, in most cases, this was sufficient to extract a temperature dependence.

4.1-2 Measurements in a Magnetic Field

In order to study the behavior of our samples in a magnetic field, we used a standard cryostat with a meter-long stainless steel tube connecting the brass plate at the top and the copper block for mounting the samples at the bottom. During a run, the copper block had one side in the ^{4}He bath and the other in a vacuum can. The cryostat was designed to fit into a narrow-tailed dewar which was suspended between the two pole pieces of a conventional electromagnet. The samples were aligned on the block so the wires were perpendicular to the axis of the cryostat. It was possible to rotate the magnet around the dewar on a track so the field could be oriented parallel or perpendicular to the samples, where, for the wires, perpendicular meant normal to the plane of the wafer. The magnet, which was feedback-stabilized, was swept over

the range from 0 to 10 kilogauss. We used a Bell model 615 gaussmeter with a Hall-effect probe to measure the magnitude of the field. The temperature of the sample was measured with a nearby germanium resistance thermometer and verified by comparison with the helium vapor pressure. At these low fields, magnetoresistance in the germanium thermometer produced errors of at most several mK, which could be ignored.

These measurements proved to be difficult for a variety of reasons. To avoid having to thermally cycle a Stycast epoxy seal and also because of size limitations, the vacuum seal was at room temperature and the lead wires traveled down to the samples in the evacuated stainless steel tube. Although the wires were wound many times around the copper block in the sample chamber and thermally sunk with GE varnish, it was difficult to cool the leads, and therefore the sample, much below 2°K. We considered adding some exchange gas, but this would have made measurements above the bath temperature suspect. This limitation on temperature in turn limited the size of the resistance rise which we could hope to observe. Furthermore, the magnet introduced a lot of vibration, especially at the higher fields, causing the temperature to rise and making sensitive measurements impossible. As a result, we were only able to obtain qualitative data on the magnetic field dependence of the low temperature resistance rise in our wire samples; however, it was possible to measure the relatively large magnetoresistance effects in the nickel samples.

4.1-3 Thermometry

We used calibrated doped-germanium resistance thermometers in both cryostats to accurately measure the temperature of our samples. According to the manufacturers, the construction of these thermometers is such that the sensing elements are both thermally and electrically isolated from their cases. Therefore, the primary thermal input to the device is through the electrical leads. For this reason, we took a great deal of care to thermally sink the thermometer leads to the sample mounts by wrapping them many times and anchoring them with GE varnish.

In the ^{3}He cryostat, we started out with a Scientific Instruments model 5-^{3}He thermometer that had a resistance of 22.5Ω at 4.2°K, but was relatively flat at higher temperatures. John Graebner of Bell Laboratories kindly performed the calibration on this thermometer, which was loaned to us by D. D. Osheroff, also of Bell Laboratories. When we discovered that we needed good thermometry at temperatures above 4.2°K, we purchased a calibrated Lake Shore Cryotronics model GR-200A arsenic-doped germanium resistance thermometer. This had a reasonable resistance at 1.0°K (575Ω) and a drop of over 68Ω between 4.2°K and 20°K. For the magnet rig, we used a Cryocal model CR1000 doped-germanium resistance thermometer that had a resistance of 993Ω at liquid helium temperature and was calibrated from 1.5°K to 100°K. In both cases, we had confidence that the sample and thermometer were in good thermal contact because they both responded almost instantaneously to sudden temperature changes.

4.2 Measurement Circuitry

The resistance measurements of the wire arrays were complicated by several considerations. First, although the resistance of an individual array was in a convenient range (100 to 10,000Ω), the measuring current could not be chosen at will because the current effectively heated the sample. Since the measuring currents were therefore constrained to be less than 1μA, we required nanovolt sensitivity in order to observe resistance changes of 5 parts in 100,000. This led us to another consideration, namely that spurious nanovolt signals are numerous. They can arise from resistance changes in the copper lead wires as the liquid helium level falls in the dewar, from drift in the amplifiers, and from small changes in the resistance standards. We started out using a two-terminal Wheatstone bridge circuit for the measurements, since it enabled us to isolate small resistance changes from a large constant background resistance; however, we switched to a four-terminal arrangement to avoid some of the above-mentioned problems. In addition, we employed a phase-synchronous ac scheme rather than dc to get maximum sensitivity and to eliminate concern about thermal emfs, which can be microvolts in magnitude. The two-terminal bridge circuit is described in section 4.2-1 and the four-terminal circuit is described in section 4.2-2.

4.2-1 Two-Terminal AC Bridge Circuit

The first circuit that we used for our resistance measurements is shown in Fig. 4.2. Only the part inside the dashed line was actually at low temperatures. A small, variable ac voltage from the reference output of a PAR model 124 lock-in amplifier was applied through a 1M resistor, serving as an ac current source for the Wheatstone bridge setup. We used wire-wound resistor boxes for R_1, R_2, and R_3 nd varied R_3 (with $R_1 \approx R_2$) until the voltage between points A and B i he circuit was zero. At the null, the resistance of the sample ,) was simply equal to:

$$R_X = R_1 R_3 / R_2.$$

The same lock-in amplifier was used as the null detector. The output of the lock-in was carefully peaked by alternately varying the frequency of the detection circuit so as to maximize the signal amplitude and zeroing the $90°$-out-of-phase component until a stable output signal was achieved. In this way, we were able to resolve resistance changes of about 1 part in 10,000. Although we were careful to thoroughly warm up the electronics (including the resistance boxes) before making any measurements, this arrangement proved to be particularly susceptible to drift. Also, taking data was quite cumbersome, involving manually adjusting R_3, and writing down R_1, R_2, and R_3 for each temperature. Since we were also concerned about problems with the lead wires and possible temperature dependences in the moderately high resistance

TWO-TERMINAL AC BRIDGE CIRCUIT
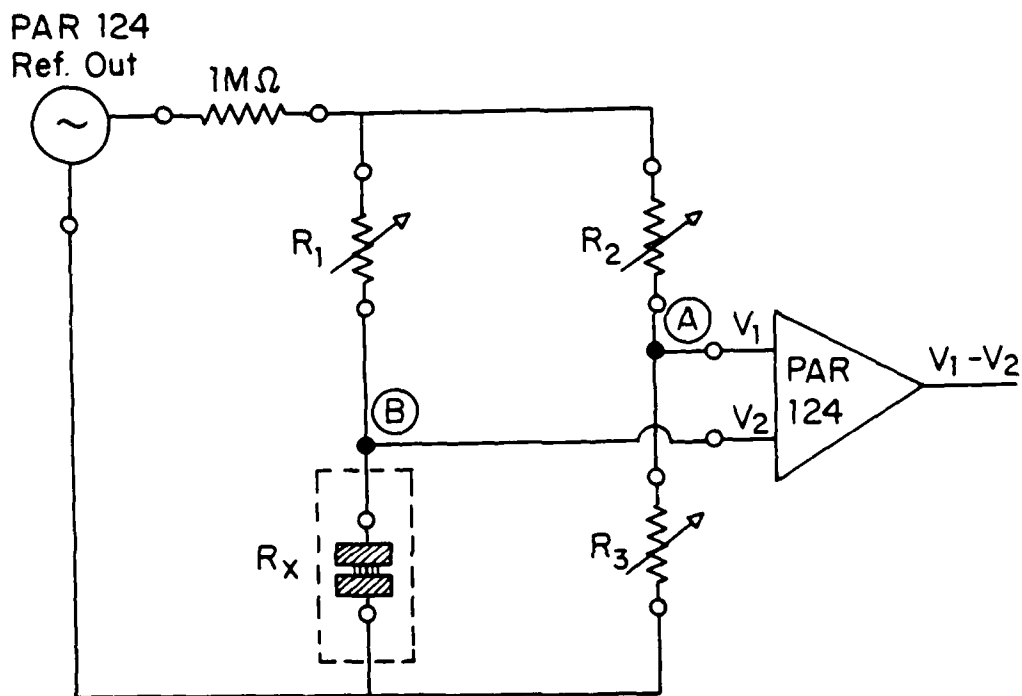
Fig. 4.2: Drawing of the two-terminal ac bridge circuit used to make the first experimental resistance measurements. The part inside the dashed line was immersed in ^{4}He.

contacts to the samples, we eventually switched to a four-terminal arrangement.

4.2-2 Four-Terminal AC Circuit

Fig. 4.3 shows a schematic of the four-terminal ac measuring circuit that was used in taking most of our data. Again, a small ac voltage from the reference output of a PAR 124 lock-in amplifier was dropped across a large resistor and the small ($<1\mu A$) ac current was applied to the current pads on the sample. The ac voltage that appeared between the voltage pads on the sample was then detected with the lock-in amplifier which had been peaked in the manner already described. The large, constant background signal was nulled out with the dc zero offset on the amplifier, thereby increasing the sensitivity. After an overnight warm-up, we found that the circuit was very stable over a couple of hours. The thermometer resistance was measured in a similar way, but without the use of the offset.

The measuring currents were calibrated every time the scale was changed using high precision resistors of known value. First, the sensitivity of the PAR output was adjusted so that the calibrator input signal yielded the proper full scale output signal. Then, the reference output voltage (i.e., the current) was adjusted until a four-terminal measurement of the calibrating resistor gave the correct value for the chosen current.

FOUR-TERMINAL AC CIRCUIT
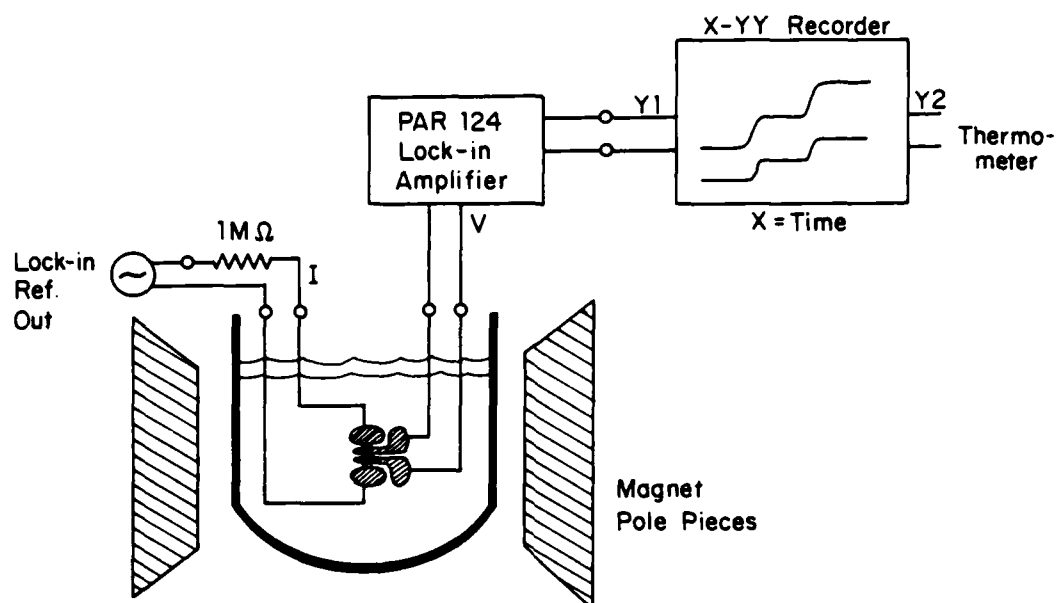
Fig. 4.3: Schematic of the four-terminal ac circuit used to make most of the experimental resistance measurements, showing typical X-YY recorder traces of the thermometer and sample voltages vs. time.

Except for the measurements in a magnetic field, all of the data
were taken in a Rayproof rf-shielded room. The dewar that we used was
surrounded by a Mu-metal shield to reduce the earth's magnetic field.
Each of our measuring circuits was frequently tested with an ordinary
resistor to insure that what we were observing were indeed changes in
the sample resistance. Joule heating effects were observed at higher
currents in the smaller samples, so we were careful to make the
measurements in a range where, to within the experimental error, the
resistance was independent of the measuring current. We also verified
that the sample resistance was independent of frequency at the low
frequencies we chose.

To ascertain that the sample and the thermometer were in good
thermal contact, we simultaneously recorded the outputs of the two
lock-in amplifiers (which were proportional to the voltages across the
sample and the thermometer, respectively) on a two pen X-YY recorder.
The X-axis usually registered time, but could be arranged to record
magnetic field amplitude. This meant that we could readily observe when
the sample and the thermometer had equilibrated after an increment in
temperature. The response of the sample to temperature changes was
rapid, but we always waited for more than one minute at each temperature
value to be absolutely certain of the data.

CHAPTER FIVE: RESULTS and DISCUSSION

We have made low temperature resistance measurements on ultrathin
wires and thin films of copper, 60 at.% gold – 40 at.% palladium
($Au_{60}Pd_{40}$) alloy, and nickel that were fabricated using the shadowing
technique. In addition, we have carefully reanalyzed the data on
similar samples already in the published literature (Giordano, Gilson,
and Prober, 1979; Chaudhari and Habermeier, 1980; Masden and Giordano,
1981). All of these results are found to be remarkably consistent
(within a factor of ~ 2) with the quantitative prediction of the
interaction model of Altshuler, Khmel'nitzkii, Larkin, and Lee, (1980b)
using independently determined material parameters. Accordingly, we
infer that interaction effects are at least as important as, and may
dominate over, localization effects in all one-dimensional
lithographically-produced samples reported to date.

In section 5.1, we present our best resistance versus temperature
data for a set of copper wire samples. The observed resistive behavior
of these wires can be explained as arising from three separate effects.
Since these are comparable in magnitude at low temperatures,
considerable care is necessary to obtain quantitatively meaningful
results. After the curve fitting procedure is described and the results
for copper are compared with the theory, the analysis is applied as much
as possible to our less complete data on AuPd alloy and nickel wires in
section 5.2, and to the data already in the published literature in
section 5.3. We close with a summary based on this comprehensive
analysis of all the available data on one-dimensional

lithographically-produced samples.

5.1 Analysis of Copper Data

In general, at high temperatures, the behavior of a typical
ultrathin wire sample is similar to that of a bulk sample. The
resistance of the sample drops rapidly as the sample is cooled through
liquid nitrogen temperatures and then begins to flatten out at $\sim15^{\circ}$K;
however, at lower temperatures, the resistance reaches a minimum value
and begins to rise again. The behavior of the sample resistance in this
temperature region is the focus of our analysis.

The data that is discussed in this section consist of resistance
(R) versus temperature (T) curves for a set of three copper wire samples
from the same wafer. The reactive ion etch (RIE) depths of the surface
relief structures for the three arrays were 800Å, 400Å, and 200Å
respectively, and the thickness of the copper film that was evaporated
to form the wires was 220Å. A broad, thin film evaporated at the same
time as the wires was also measured, but, below $\sim10^{\circ}$K, it showed no
temperature dependence within the experimental resolution. A summary of
the sample characteristics is given in Table 5.1.

Table 5.1:   Characteristics of Copper Samples

RIE depth	copper film depth	R_{RT} (Ω)	R_{LT} (Ω)	RRR	#	T_{min} ($^{\circ}K$)	ρ_{LT} (ohm-cm)
film	220Å	24.20	13.27	1.82	--	--	2.6×10^{-6}
200Å	220Å	447.0	302.7	1.48	100	9.81	2.6×10^{-6}
400Å	220Å	379.6	252.3	1.50	60	8.51	2.6×10^{-6}
800Å	220Å	121.2	80.93	1.50	93	7.77	2.6×10^{-6}

5.1-1 Three Contributions to the Observed Resistance

When we first began analyzing the R vs. T curves for the copper wires, we tried fitting the data to a $T^{-1/2}$ temperature dependence which was one of the predictions of the early theories (Altshuler et al., 1980b; Thouless, 1980). The fit was excellent at low temperatures, but there was a small deviation toward higher values of the resistance at higher temperatures. In trying to understand this slight deviation, we realized that the resistive behavior that we had observed actually included contributions from three different effects. This can be seen when the total resistance is written as a sum of three terms:

$$R = aT^{-1/2} + bT^m + R_0. \qquad (5-1)$$

The first term is simply the contribution to the total resistance from localization or interaction effects, and the coefficient, a, depends inversely on the cross-sectional area as discussed in Chapter Two. The second term represents the contribution from the ordinary resistance rise at higher temperatures in a bulk metallic sample; it is independent of area and is expected to increase with some power of T (Blatt, 1968). The final term is just the temperature-independent contribution from the bulk residual resistance. From eqn. (5-1) it is apparent that as the temperature is raised, the second term becomes increasingly more important and causes the deviation from a strictly $T^{-1/2}$ dependence.

The theoretical resistance of a wire sample is reconstructed graphically in Fig. 5.1, where m is chosen to be 3 and the curves are plotted relative to the inferred residual resistance. From this reconstruction, it is clear how the temperature of the minimum resistance point (T_{min}) and the magnitude of the measured resistance rise at low temperatures from that point ($\Delta R(T) = R(T) - R_{min}$) depend strongly on the relative magnitude of the two temperature-dependent terms. Moreover, the magnitude of the actual rise from the minimum is only a fraction (typically about half) of the total rise given by eqn. (2-31) because the resistance at the observed minimum is larger than the residual resistance. In order to isolate the desired effect (i.e., the first term in eqn. (5-1)), it is most convenient to analyze the data at low temperatures where the bT^3 term is negligible.

We also realized that, although the magnitude of the first term is expected to vary with the cross-sectional area of the wires, the magnitude of the second term should remain constant for a given material. This implies that it should be possible to fit the data for copper wires with different cross-sectional areas (but made in the same evaporation) by using the same bT^3 curve and scaling the $aT^{-1/2}$ curve depending on the relative areas of the wires. Fig. 5.2 illustrates that this is indeed the case. Here, resistance versus temperature curves for the three copper wire samples are plotted. The fits to the data at temperatures below the minimum vary with area, but the same bT^3 term fits the data adequately at temperatures above the minimum. More details of the curve fitting are provided in the next section.
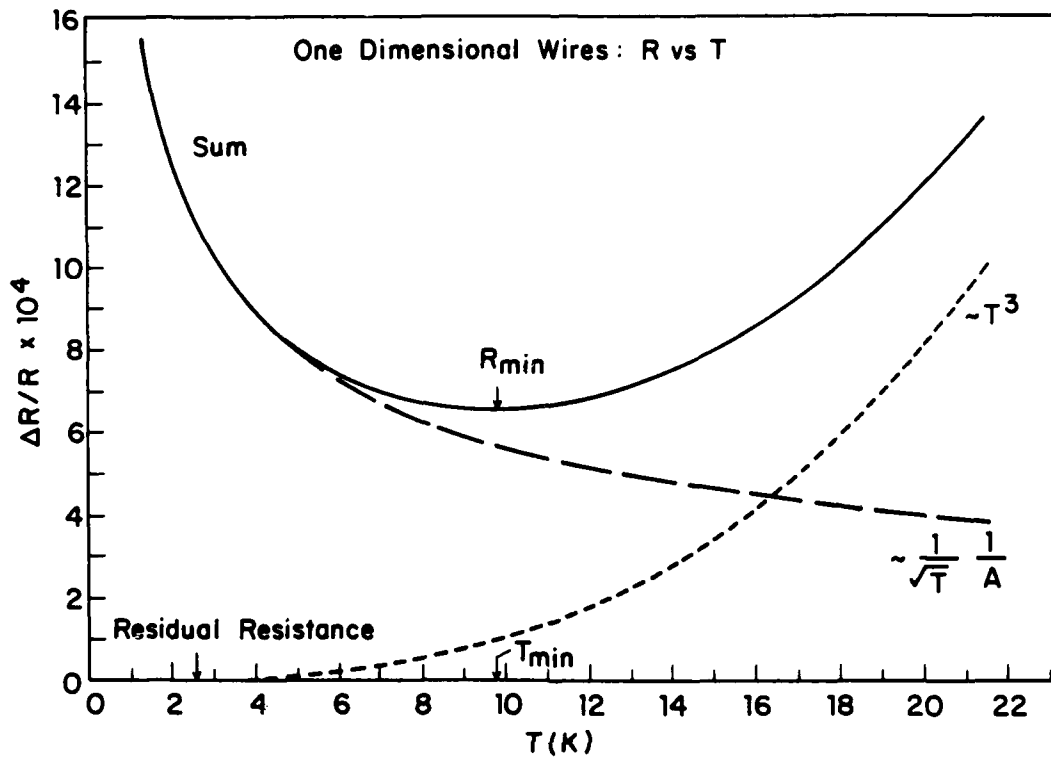
Fig. 5.1: Reconstruction of the experimentally-measured resistance variation in the ultrathin copper wires (heavy line) as a sum of a high temperature rise as T^3 characteristic of the bulk material (short dashes) and a low temperature rise as $A^{-1}T^{-1/2}$ characteristic of the one-dimensional interaction effect (long dashes).
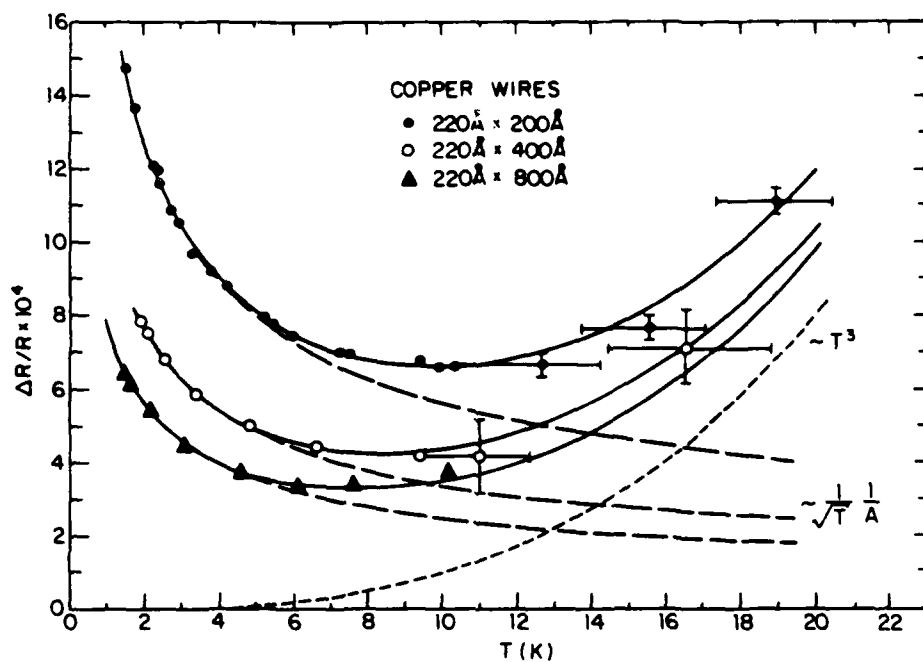
Fig. 5.2: Same plot as in Fig. 5.1 with the addition of the data for the three ultrathin copper wire samples. For temperatures above T_{min}, the points all fall on the same curve ($\sim T^3$), while for temperatures below the minimum, the fit depends on the cross-sectional area. The wide error bars at temperatures above the resistance minimum reflect data taken under transient conditions during cool-down. The data points at low temperatures were taken under steady-state conditions and are much more accurate.

5.1-2 Curve Fitting

The minimum in the R vs. T curve of a thin wire sample that is described by the function in eqn. (5-1) occurs when $\partial R/\partial T = 0$. Setting the derivative of eqn. (5.1) equal to zero and solving for T yields

$$T_{min} = \{ \frac{a}{2mb} \}^{\frac{1}{m+1/2}}.$$
$$(5-2)$$

Substituting this back into (5-1) gives, for the resistance at the minimum,

$$R_{min} = a(1 + \frac{1}{2m}) \frac{1}{T_{min}^{1/2}} + R_o$$
$$(5-3)$$

and, for the resistance rise at temperature T,

$$\Delta R = a\{ \frac{1}{T^{1/2}} + \frac{1}{2m}(\frac{T^m}{T_{min}^{m+1/2}}) - (1 + \frac{1}{2m}) \frac{1}{T_{min}^{1/2}}\}$$
$$(5-4)$$

where b is written in terms of T_{min} using eqn. (5-2). In order to fit the data to this expression, it is helpful to regroup the terms:

$$\Delta R = a\{(\frac{1}{T^{1/2}} + \frac{1}{T_{min}^{1/2}}) + \frac{1}{2m}(\frac{1}{T_{min}^{1/2}})([\frac{T}{T_{min}}]^m - 1)\} .$$
$$(5-5)$$

The first term in brackets is the simple fit for the low temperature resistance rise from the minimum and the second term in brackets can be

interpreted as the correction to the simple fit due to the normal

resistance rise at higher temperatures. In the major region of the fit,

$(T/T_{min})^m \ll 1$, so the correction term is nearly a negative constant:

$$\delta R = -a(\frac{1}{2m})\frac{1}{T_{min}^{\frac{1}{2}}} . \tag{5-6}$$

Then the value of ΔR extrapolated to $1/T = 0$ is:

$$\Delta R_{extrap.} = -a(\frac{1}{T_{min}^{\frac{1}{2}}})(1 + \frac{1}{2m}) . \tag{5-7}$$

The ratio of the correction term (which is just the difference between

the simple $T^{-1/2}$ fit and the data at $T = T_{min}$) to the extrapolated value

of ΔR can be used to fix the value of m:

$$\frac{\delta R}{\Delta R_{extrap.}} = \frac{1}{2m + 1} . \tag{5-8}$$

However, unless T_{min} is accurately determined using data on both sides

of the resistance minimum, this value for m is not much more than a

guess.

Although we had data over a large range of temperature for two of

our copper wire samples, only the low temperature data were taken with

great accuracy. Following this procedure, we were able to fit the data

for these samples over the entire temperature range from 1-20°K using

only the accurate low temperature points and the measured value of T_{min}

to determine the coefficients, a and b. First, the slope and intercept

for the lowest temperature points of the R vs. $T^{-1/2}$ curve for each wire

sample were determined using the method of least squares. Next, the

magnitudes of ΔR and $\Delta R_{extrap.}$ were obtained from this fit at

$T^{-1/2} = (T_{min})^{-1/2}$ and $T^{-1/2} = 0$, respectively. The ratio of these two

quantities then yielded a value of m approximately equal to 3. When

this procedure was repeated for the 220Å x 400Å area copper wire sample,

the m was computed to be approximately equal to 3, also. This agreement

gave us confidence in the applicability of the model. By adjusting the

T_{min} values slightly, we were able to fit the data for all three copper

samples with m = 3. These are the fits that are plotted in Fig. 5.2.

5.1-3 Comparison With Theory

To facilitate a quantitative comparison with experimental data and

to illuminate the physics, we have rewritten the result of Altshuler et

al. (1980b) as

$$\frac{\Delta R}{R} = \frac{(2-F)}{\sqrt{6}} \left(\frac{\rho}{\hbar/e^2}\right)^{1/2} \left(\frac{k_B}{\gamma_V^* T}\right)^{1/2} \frac{1}{A} \qquad (5-9)$$

This follows directly from eqn. (2-31) using

$$\rho = \left(\frac{ne^2\tau}{m}\right)^{-1}$$

$$D = \frac{1}{3} v_F^2 \tau$$

and

$$\gamma_V^* T = \frac{(\frac{\pi}{3})^{2/3} (\frac{k_B}{\hbar})^{1/2} m\, n^{1/3}\, T}{(1 + \lambda)}$$

which are free electron model results (Ashcroft and Mermin, 1976).

In eqn. (5-9), $\gamma_V^* T$ is the electronic specific heat per unit volume divided by the enhancement factor $(1 + \lambda)$ due to the electron-phonon interaction. Although the experimentally-determined specific heat includes this factor, it has been shown that the transport coefficients are unaffected by the many-body effects of the electron-phonon interaction (Prange and Kadanoff, 1964). The enhancement factor itself has been measured in a variety of ways which are summarized in a review article by Grimvall (1976). More recently, Jansen et al. (1980) have made very accurate determinations of λ for several metals, including copper and gold, using point contact spectroscopy.

Returning to eqn. (5-9), A is the cross-sectional area of an individual wire, ρ is the resistivity of the metal in the wires, and F is the screening parameter which is theoretically expected to lie between 0 and 1 (Altshuler, Aronov, and Lee, 1980a). Because there is some uncertainty as to the number of continuous wires in each array, we calculated the resistivity of the copper by substituting the measured resistance and the well-known dimensions of the thin film (evaporated at the same time as the wires) into the standard relation, $\rho = RA/L$. We also calculated the residual resistance ratios (RRRs) of the wires and the film. The RRR is defined as the ratio between the room temperature

resistance and the low temperature resistance of the sample (the latter

is effectively constant for this purpose) and is a measure of the purity

of the material. Since the RRRs of our samples were similar (~ 1.5 for

the wires, ~ 1.8 for the film), we inferred that all the samples were

composed of basically the same material. The difference in the RRRs is

probably due to the size-effect resistivity (observed in small samples

where surface scattering is comparable to impurity scattering) which is

more important in the wires than in the film (Fuchs, 1938; MacDonald

and Sarginson, 1950). However, it could also be due to slight

differences in the grain structure between the film and the wires.

In addition to summarizing the sample characteristics in Table 5.1,

we have also listed the number of continuous wires in each array. This

number was calculated using the value of ρ determined from the copper

film together with the measured array resistance and the known single

wire dimensions. We find good agreement between the inferred number of

wires and the expected number of wires (100) for two of the copper

samples, confirming our choice of ρ. Inspection of the third sample

(220Å x 400Å) under an optical microscope revealed a defect in the

grating. As a result, we attribute the relatively high resistance of

this sample to discontinuous wires, rather than to a higher resistivity.

In testing the fit of eqn. (5-9) to the experimental data,

considerable care is required to obtain quantitatively reliable results,

for reasons made clear in section 5.1-1. First, it is important to note

that the expression, $(\Delta R/R)\sqrt{T}$, really means the slope,

$d(\Delta R/R)/d(1/\sqrt{T})$, below the minimum. This subtle difference can cause

a fairly large underestimate of the size of the effect since the square root dependence of T is so slow. Furthermore, to isolate the desired effect from the normal resistance rise, in Fig. 5.3(a) we plot the data versus $T^{-1/2}$ and take the slope in the low temperature region where the T^3 term is negligible. Next, the slopes determined in this way are plotted against 1/A. This averages over sample-to-sample variations and effectively isolates the true one-dimensional effect from any background effects present in the wide film, which would not depend on 1/A. (The latter would simply appear as extra area-independent terms in eqn. (5-9).) In particular, spurious contributions to the total resistance from any Kondo effect resistance rise (Ashcroft and Mermin, 1976) due to magnetic impurities in the copper are eliminated. The results of following these procedures with the copper samples are shown in Fig. 5.3(b). In this way, we made an experimental determination of the coefficient of $T^{-1/2}A^{-1}$ in eqn. (5-9).

Although the fit of the data to a $T^{-1/2}$ temperature dependence is excellent, as demonstrated in Fig. 5.3(a), we have also plotted the data on a logarithmic scale in Fig. 5.4. This temperature dependence of the resistance rise was predicted for the two-dimensional case (Altshuler et al., 1980a). Comparing Fig. 5.3(a) and Fig. 5.4, it is clear that, for our copper wires, the temperature dependence is faster than logarithmic and the data agree better with the $T^{-1/2}$ dependence over a much wider range of temperature.

For the purpose of testing the theory, we have reduced the experimental data by the technique outlined above to the form of the
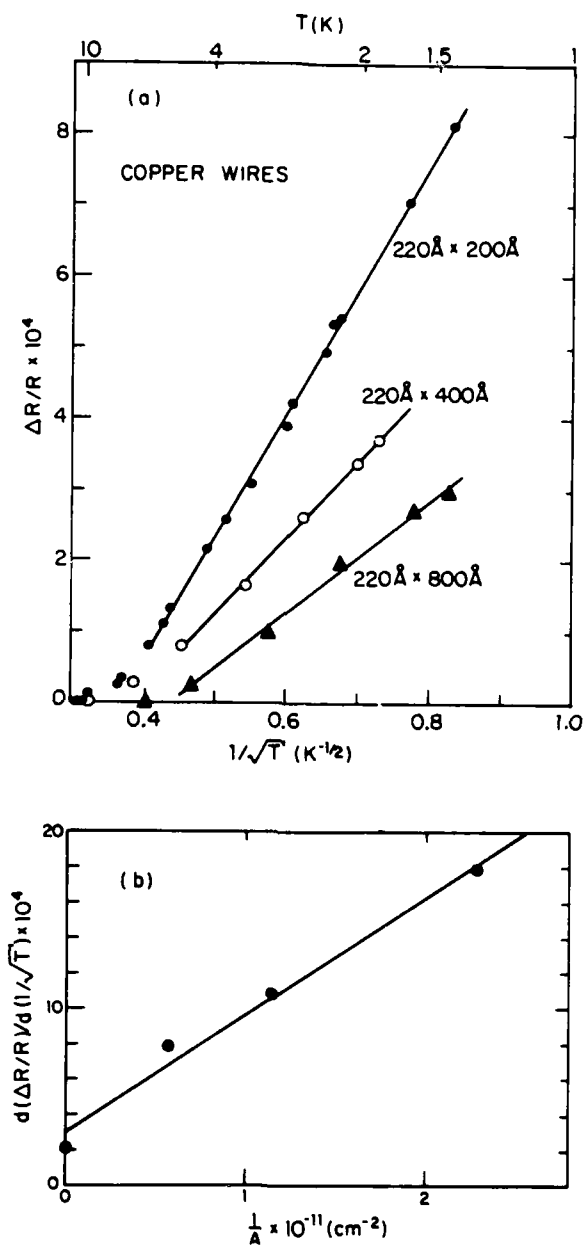
Fig. 5.3: (a) Same data as in Fig. 5.2, but plotted vs. $T^{-1/2}$ to isolate the interaction effect. Only the low temperature points, where the T^3 term is negligible, are fitted.
(b) Plot of slopes found in (a) vs. 1/A to separate the one-dimensional effect from any bulk effect also giving a resistance rise at low temperatures. The point at 1/A = 0 is an upper bound set by the experimental accuracy.
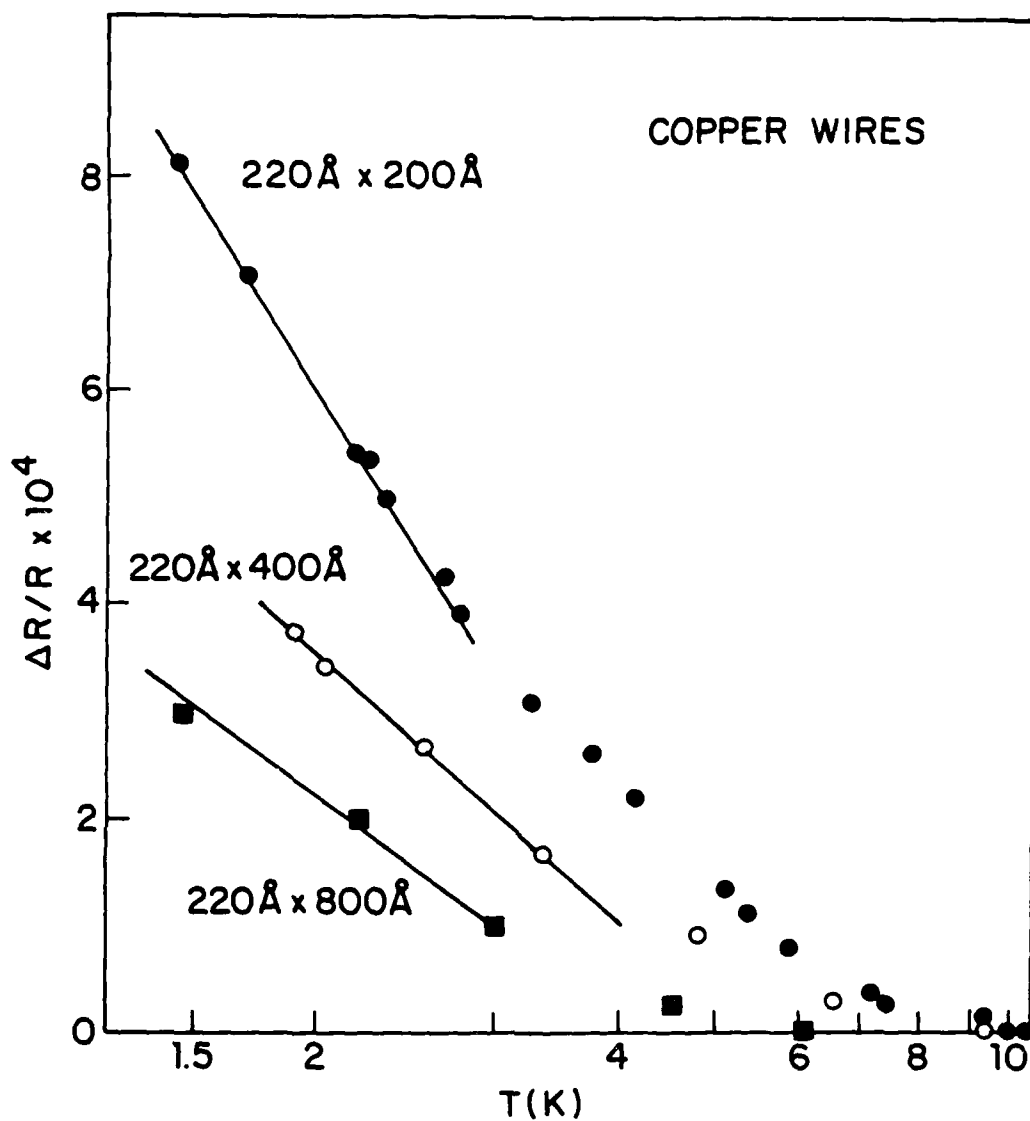
Fig. 5.4: Same data as in Fig. 5.1, plotted with a logarithmic temperature scale. Clearly, the data rises more steeply than ln T and agrees better with the $T^{-1/2}$ dependence over a wider range of temperature.

value of (2 - F) required in eqn. (5-9) to reproduce the observed
increase in resistance. The value of γ_v for copper has been found to
be insensitive to the structure of the copper (Bevk, 1973) so, using the
literature value of γ_v^* for pure copper (see Table 5.2) and the value
of ρ determined from the measured resistance and the known geometry as
previously described, we have arrived at a value of (2 - F) for the
copper samples equal to 1.6 ± 0.3. The agreement with the
theoretically-expected value of $F \approx 0.4$ (Patrick Lee, private
communication) is so impressive that we were encouraged to make similar
analyses of our less complete data on AuPd alloy and nickel wires, and
to re-examine the data in the literature from the same perspective.

5.2 Analysis of AuPd and Nickel Data

The set of AuPd alloy wire arrays that we have analyzed had RIE
depths of 250Å, 500Å, and 1000Å respectively, and 500Å of AuPd was
evaporated to form the wires. The broad, thin film that was evaporated
at the same time had an anomalously high resistance. We thought that
this might be attributable to problems with adhesion that developed
during the lift-off process which was used to form the film but, using
an optical microscope, we were only able to verify that the film was of
generally poor quality. The wire samples were not subjected to any
solvents after being formed, so, for our analysis, we made an estimate
of the AuPd resistivity using the dimensions and measured resistances of

Table 5.2: Electronic Specific Heat Parameters

The parameters γ_v^* used in reducing the experimental data were obtained from experimental values of γ for the elements quoted by Kittel[a]; by converting to unit volume (γ_v) and then dividing out the phonon enhancement factor $(1 + \lambda)$. The numerical values used are tabulated here. Values quoted in parentheses are estimated from values for other metals in the absence of knowledge of directly determined values.

Metal	$\gamma\left(\frac{mJ}{mol\text{-}K^2}\right)$	$\gamma_v\left(\frac{ergs}{ccK^2}\right)$	λ	$\gamma_v^*\left(\frac{ergs}{ccK^2}\right)$
Cu	0.695	980	0.15 ± 0.02[b]	852
Ni	7.02	7701	(0.7 ± 0.01)[c]	4530
Pt	6.8	7462	0.6 ± 0.1[d]	4664
AuPd	(0.73)[e]	714	(0.16)[f]	616
WRe	(1.9)[g]	2100	(0.9 ± 0.2)[h]	1106
Bi	0.008	3.75	(<0.0005)[i]	3.75

(a) C. Kittel, "Introduction to Solid State Physics", Wiley, New York, 4th ed., 1971, p. 254.
(b) A. G. M. Jansen, A. P. van Gelder, and P. Wyder, J. Phys. C13, 6073 (1980).
(c) Value from (d) for Pd, which is just below Ni in periodic table.
(d) G. S. Knapp and R. W. Jones, Phys. Rev. B6, 1761 (1972).
(e) Value for Au, by analogy with the work on AgPd alloys by H. Montgomery, G. P. Pells, and E. M. Wray, Proc. Roc. Soc. (London) A301, 261 (1967).
(f) Value for Au from ref. (b); see ref. (e).
(g) Weighted average of values for W and Re, which are adjacent in periodic table.
(h) Value from ref. (d) for Ta, which is adjacent to W in periodic table.
(i) Value from R. A. Herrod and R. G. Goodrich, Phys. Lett. 33A, 331 (1970) for Sb, which is just above Bi in periodic table.

the two largest cross-sectional area samples, assuming 100% yield of wires. The characteristics of the AuPd samples are summarized in Table 5.3.

Following the procedure described in section 5.1-3, in Fig. 5.5(a) we plot the AuPd wire data versus $T^{-1/2}$ and find excellent agreement at low temperatures. Since low temperature minima have been observed in the R vs. T curves of _bulk_ AuPd alloy samples (Edwards _et al._, 1970), it is particularly important in this case to separate the one-dimensional effects from any background effects by plotting the fitted $T^{-1/2}$ slopes from the low temperature region against 1/A (Fig. 5.5(b)). Determining the slope of this line using a least squares method then provides the experimental value for the coefficient of $T^{-1/2}A^{-1}$ in eqn. (5-9).

The point at 1/A = 0 in Fig. 5.5(b) represents a reasonable value for the slope corresponding to the resistance rise that was observed in the AuPd film. Some approximation is necessary for two reasons. First, as expected for two-dimensional systems, the temperature dependence of the resistance rise in the film is more closely logarithmic than $T^{-1/2}$ (Fig. 5.6). Thus, the slope of the $T^{-1/2}$ plot has less meaning for the film than for the wires. Second, since the film was of low quality, we cannot place much emphasis on the magnitude of its resistance rise. For the purpose of this analysis, the point at 1/A = 0 has a relatively small influence on the value of the fitted slope; nonetheless, we have incorporated this uncertainty into our error estimates.
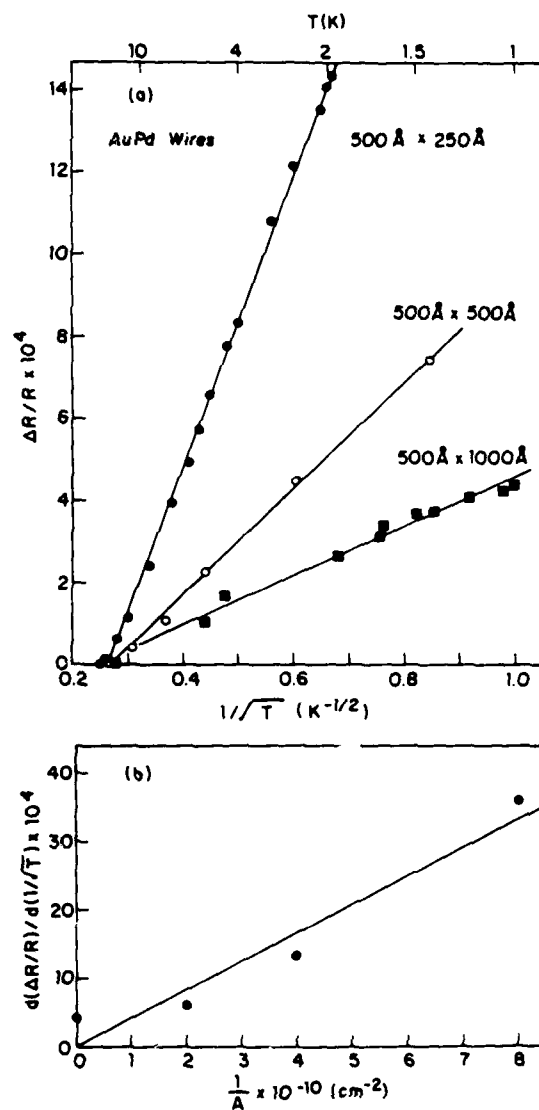
Fig. 5.5: (a) Data for AuPd wires plotted against $T^{-1/2}$ to isolate the one-dimensional effect. Only the low temperature points are fitted.
(b) Plot of slopes found in (a) vs. 1/A to separate the one-dimensional effect from the bulk effect which is known to give a resistance rise at low temperatures. The point at 1/A = 0 is an estimate of the effective slope of the resistance rise in the AuPd film, which had a ln T dependence (shown in the next figure). Since the film had an anomalously high resistivity, there is a large uncertainty in this point, but it does not have much effect on the fitted slope.
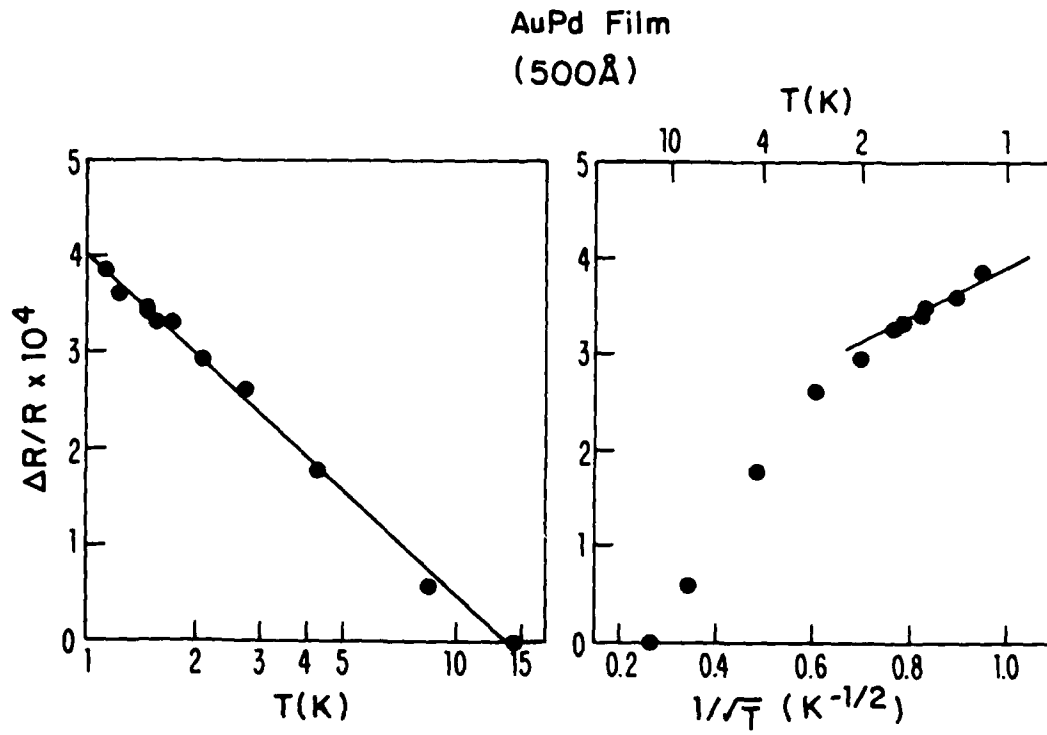
AuPd Film
(500Å)

Fig. 5.6: Data for the low temperature resistance rise in AuPd film
compared to $T^{-1/2}$ and ln T iependences. In contrast to the
wire data (Fig. 5.4), these data agree more closely with a
ln T dependence.

Table 5.3: Characteristics of AuPd and Ni Samples

Material	RIE depth	Film Depth	R_{RT} (Ω)	#	T_{min} ($^{\circ}K$)	ρ_{LT} (ohm-cm)
AuPd	film	500Å	869.8	--	14.3	400×10^{-6}
AuPd	250Å	500Å	12.50k	9	16.4	(27.6×10^{-6})
AuPd	500Å	500Å	1092	52	13.8	(27.6×10^{-6})
AuPd	1000Å	500Å	317.1	100	13.0	30.6×10^{-6}
AuPd	2000Å	500Å	127.8	100	not meas.	24.6×10^{-6}
Ni	film	400Å	151	--	--	6.0×10^{-6}
Ni	450Å	400Å	6321	5	13.0	6.0×10^{-6}

To complete the analysis on the AuPd wires, the value of $(2 - F)$ required to reproduce the observed effect has been calculated and is found to be 2.9 ± 1.2, also within the range of the theoretically-predicted value. The additional uncertainty comes from the choice of γ_v^*, which, to the best of our knowledge, has not been directly measured for the AuPd alloys. Therefore, we chose the value of γ_v for pure gold by analogy with the work on the silver-palladium (AgPd) alloys by Montgomery et al. (1967), where it was found that the γ_v of these alloys was equal to the γ_v of silver for palladium concentrations up to 50 at.%.

We next consider the data from a nickel wire sample. Although we had not yet developed the technique of making samples with different cross-sectional areas in the same evaporation when we were fabricating nickel wire arrays and, consequently, we had no complete sets of nickel samples, it seemed worthwhile to attempt an analysis of a single nickel wire array. The one which was chosen had wires that were 450Å thick and 400Å wide. A broad, thin film evaporated at the same time as the wires showed no low temperature resistance rise to within the experimental error. Using the fitted slope from the low temperature region of an R vs. $T^{-1/2}$ plot, the known cross-sectional area of an individual wire, and the value of ρ determined from the film, we computed a value of $(2 - F) = 2.9 (+1.6, -1.2)$. Within the estimated errors, which result from both the uncertainty in the value of γ_v^* for nickel and the uncertainty in determining the effect from a single sample, this also falls in the range of the theoretically-expected value $(2 - F \approx 1 \rightarrow 2)$.

What emerged, then, from a careful analysis of our measurements on three very different systems is substantial evidence in support of the predictions of the interaction model. At this point, it seemed appropriate to analyze the data published by other groups (Giordano et al., 1979; Chaudhari and Habermeier, 1980; Masden and Giordano, 1981). This is discussed briefly in the next section.

5.3 Reanalysis of Data in the Literature

The wire data which we have reanalyzed represents work from three other groups on four different systems: evaporated ("clean") $Au_{60}Pd_{40}$ alloy and sputtered ("dirty") $Au_{60}Pd_{40}$ alloy by Giordano, Gilson, and Prober (1979) at Yale, platinum (Pt) by Masden and Giordano (1981) at Purdue and amorphous tungsten-rhenium (WRe) alloy by Chaudhari and Habermeier (1980b) at IBM. We will also discuss the null results on bismuth (Bi) whisker samples by Overcash and coworkers (1980) at Clemson and the anomalous results on drawn platinum wires by Sacharoff, Westervelt, and Bevk (1982), also at Harvard. We have summarized the characteristics of all these samples in Table 5.4.

The data on dirty AuPd wires were transcribed from Figs. 8, 10, and 11 in the review paper by Giordano (1980) and that on clean AuPd wires from Figs. 4(b), 12, 13(b), and 14 in the same paper. These data were found to agree closely with the data presented earlier by Giordano et

Table 5.4: Additional Sample Characteristics

group	material	cross-sectional area (cm^2)	R_{LT}	$T_{min}(^\circ K)$	$\rho_{LT}(\mu ohm\text{-}cm)$
(a)	dirty AuPd	2.03×10^{-11}	360kΩ	>7	370 ± 90
		3.25×10^{-11}	200kΩ	7.4	
		8.28×10^{-11}	78kΩ	>7	
		3.61×10^{-11}	32kΩ	>7	
(a)	clean AuPd	9.61×10^{-12}	122kΩ	>10	100 ± 25
		1.76×10^{-11}	8kΩ	>10	
		1.94×10^{-11}	90kΩ	>10	
		3.48×10^{-11}	61kΩ	>8	
(b)	WRe	3.40×10^{-12}	---	>11	400 ± 40
(c)	Pt	2.89×10^{-12}	---	9-10	30 ± 6
		5.76×10^{-12}	---	8-9	
		6.76×10^{-12}	---	8-9	
(d)	Bi	1.96×10^{-10}	80.08kΩ	none obs.	140
(e)	Pt	3.14×10^{-10}	---	9	300

(a) N. Giordano, Phys. Rev. B22, 5635 (1980).
(b) P. Chaudhari and H.-U. Habermeier, Sol. St. Comm. 34, 687 (1980).
(c) J. T. Masden and N. Giordano, Physica 107B, 3 (1981).
(d) D. R. Overcash, B. A. Ratnam, M. ... Skove, and E. P. Stillwell, Phys. Rev. Lett. 44, 1348 (1980).
(e) A. C. Sacharoff, R. M. Westervelt, and J. Bevk, 1982b, submitted for publication.

al. (1979) in their Figs. 2 and 3. Since they reported measurements on

wires of different cross-sectional areas with roughly the same

resistivity (100 $\pm$ 25 μohm-cm for the clean AuPd, and 370 $\pm$ 90

μohm-cm for the dirty AuPd), we were able to follow the analysis

described in section 5.1-3 in detail. Using the fitted slope of a plot

of $d(\Delta R/R)/d(1/\sqrt{T})$ vs. $1/A$ which included a point at $1/A = 0$ for the

resistance rise in the film, we calculated $(2 - F) = 1.8 \pm 0.4$ for

their clean AuPd wires and $(2 - F) = 3.4$ (+0.7, -1.0) for t ∂ir dirty

AuPd wires. The quoted uncertainties stem from the uncertainty in the

quoted values of the resistivities, the uncertainty in the assignment of

γ_v^* (AuPd) = γ_v^*(gold), and the uncertainty in calculation of a slope,

$d(\Delta R/R)/(1/\sqrt{T})$, from a measured $\Delta R/R$ at 1.5°K relative to 12°K in

their Fig. 14. We also note that, in the case of the very high

resistivity AuPd samples, it is possible that a non-compact structure

may distort the relationship between the intrinsic resistivity and the

measured resistance.

The data on Pt wires were transcribed from Figs. 1 and 2 in the

paper by Masden and Giordano (1981). From their Fig. 1, it was apparent

that, for the samples made from a 200Å film, the agreement with a $T^{-1/2}$

temperature dependence was excellent from 1°K up to $\sim 6^\circ$K. This enabled

us to convert the vertical axis in Fig. 2 to a slope, $d(\Delta R/R)/(1/\sqrt{T})$,

by simply multiplying by a factor of $(1/\sqrt{1.5} - 1/\sqrt{4.2})^{-1}$. Then,

fitting the points for 200Å Pt films in the resulting plot of

$d(\Delta R/R)/d(1/\sqrt{T})$ vs. $1/A$ and using the quoted value $\rho = 30$ μohm-cm

and the value of γ_v^* from Table 5.2, we computed a value of $(2 - F) =$

2.34 (+0.5, -0.7). In this case, the uncertainties can be largely

attributed to the scatter in the data in Masden and Giordano's Fig. 2.

We also assumed a $\pm 20\%$ uncertainty in their value of ρ (by analogy

with their work on AuPd wires) and included the 17% uncertainty in the

measured value of the phonon enhancement factor, λ.

It was more difficult to carry out a rigorous analysis for the data

on the WRe alloy wires reported by Chaudhari and Habermeier (1980a)

because of complications associated with the broad superconducting

transition at $\sim 5°$K in these films. According to a later paper from

this group (Chaudhari and Habermeier, 1980b), they determined the

magnitude of the superconducting fluctuations, which were important in

these wires at temperatures as high as $12°$K, from measurements on a wide

film of similar composition. When large corrections for the

superconducting fluctuations were included, the data agreed very well

with the $T^{-1/2}$ temperature dependence from $12°$K to $4°$K as shown in their

Fig. 1(a). This enabled us to convert to a slope by multiplying the

vertical axis in their Fig. 2 by a factor of $(1/\sqrt{4.2} - 1/\sqrt{12})^{-1}$.

Taking the slope in this new plot of $d(\Delta R/R)/d(1/\sqrt{T})$ vs. 1/A for their

data only, and using the quoted value of $\rho = 400 \pm 40$ μohm-cm and the

value of γ_v^* from Table 5.2, we calculated a value of $(2 - F) = 4.8$

(+1.9, -2.0) for the WRe sample. We assigned large uncertainties to

this value of $(2 - F)$ based on the scatter in the data in Fig. 2 (for

example, leaving the high point at $1/A = 28 \times 10^{10}$ out of the fit

decreased the value of $(2 - F)$ by 20%) and the uncertainty in estimating

a value of γ_v^* for WRe. The latter was accomplished by taking a

weighted average of the measured γ_v values for W and Re based on the atomic percentage of each in the alloy and using the measured value of λ for tantalum, which is adjacent to W and Re in the periodic table.

Overcash, Ratnam, Skove, and Stillwell (1980) have reported measurements on single crystal whiskers of bismuth (Bi) and Bi-6 at.% Antimony (Sb). These samples, with diameters as small as 1100Å, exhibited metallic behavior which persisted down to their lowest temperature of 0.4°K. Furthermore, the resistance varied approximately linearly with temperature in the low temperature region. We can explain their failure to observe a resistance minimum in the whiskers by referring back to the competition between the first two terms in eqn. (5-1). In the case of the whiskers, the normal resistance rise with increasing temperature is dwarfing any rise with decreasing temperature due to interaction effects. For an example, consider their whisker with $\sqrt{A}$ = 1400Å, length (L) = 1.123mm, and R_0 = 80.08kΩ. Using eqn. (5-9) with the calculated value of ρ = 140 μohm-cm (from R, A, and L) and γ_v^* = 3.75 from Table 5.2, the theoretically-predicted value for a, the coefficient of the $T^{-1/2}$ term, is 190 ohms-$K^{-1/2}$. Referring to their Fig. 4, we can estimate a value for b, the coefficient of the T^3 term, from the slope of the R vs. T curve in the linear region (m = 1). This turns out to be approximately 610 ohms/K. Substituting these numbers into eqn. (5-2) gives a value of T_{min} = 0.3°K, which is below the temperature range of their apparatus.

Very recently, resistance measurements have also been performed on platinum filaments with diameters <2000Å (Sacharoff et al., 1982a).

These samples were made by drawing a 1/2mm diameter polycrystalline platinum wire in a silver matrix which was then chemically removed. Low temperature resistance rises in these wires are size dependent and are greater than 1% at 2°K in the smallest area samples. This is much larger than any rises which have been observed previously. It is difficult to analyze this data within the framework that we have presented because of the large uncertainty about the sample characteristics. SEM micrographs of the filaments indicate that they have a multi-stranded structure, perhaps due to elongation of individual grains in the original wire. If this is the case, a single sample may actually consist of many wires in parallel, substantially altering the effective cross-sectional area. Furthermore, annealing these samples at only 200°C substantially reduces their resistivities and also the size of their low temperature resistance rises. This, in combination with the high sample resistivities (up to $600\,\mu$ohm-cm), is evidence of gross structural disorder and it is not clear that the interaction theory can be expected to apply in such a system.

5.4 Conclusions

The results of our measurements on the low temperature resistance rise in ultrathin wires of copper, AuPd alloy, and nickel, in addition to the results of our reanalysis of all other published work on one-dimensional samples, are summarized in Fig. 5.7, where we have
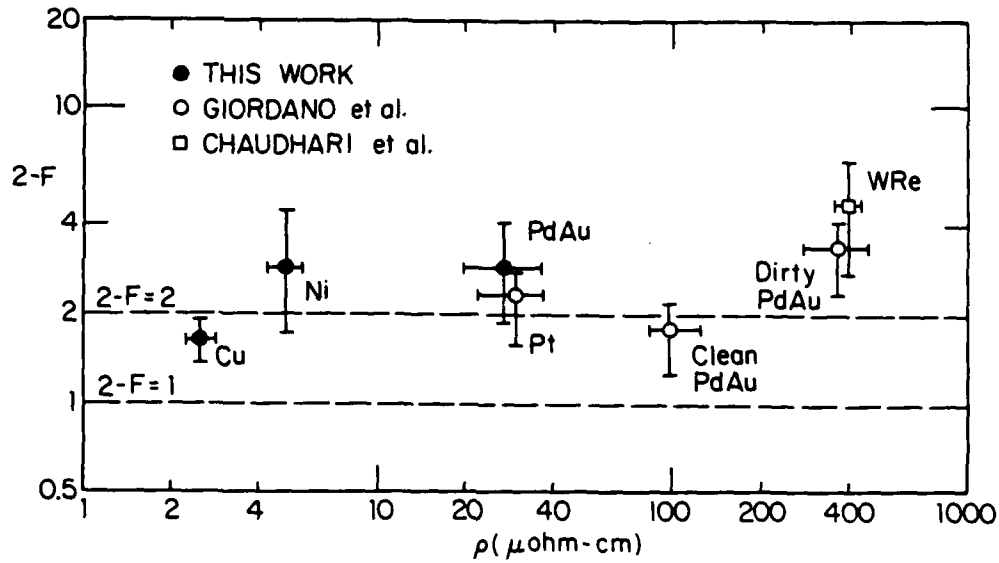
Fig. 5.7: Values of (2-F) required to fit the resistance rise data on
ultrathin wires of various metals and resistivities to the
interaction model, eqn. (5-9). (It is expected
theoretically that F should lie between 0 and 1.) The
error bars are somewhat subjective, especially for
materials for which directly measured values of γ_v are not
known to us.

plotted the values of (2 - F) obtained by reducing the experimental data using the techniques outlined in section 5.1-3. Because of the remark of Giordano (1981) that the observed effect appeared to scale as ρ instead of the theoretically-expected $\rho^{-1/2}$, we have presented the data versus ρ in a logarithmic plot. In this plot, the Giordano conjecture corresponds to a line with a slope of one-half. Such a slope is not consistent with the data over the broad range of ρ which our new results make available, although it is consistent with the data at the very high values of ρ where Giordano's results lie. As we mentioned before, it is possible that the measured resistances of the sputtered AuPd films do not accurately reflect their intrinsic resistivities. This further complicates the interpretation of the Giordano et al. (1979) data because the areas of their wires were determined by working backwards from their resistivities. Also, it may be significant that this apparent rise in the value of (2 - F) occurs where $k_F l$, the product of the Fermi wave vector (k_F) and the mean free path (1), approaches unity. At this point, the theoretical model of Altshuler et al. (1980b) is expected to fail as the conduction shifts to a hopping mechanism from the free electron approximation. Although the large uncertainties require caution in drawing general conclusions, we emphasize that the (2 - F) value found for copper (for which $\Delta R/R$ and γ_v^* have relatively small uncertainties) falls essentially where it would if the interaction effect were the only one present.

In order to force agreement between our results on copper wires and the localization model, we would have to invoke a scattering mechanism

such that the associated time had a 1/T temperature dependence and a magnitude of $\sim 10^{-11}$ sec. It has been suggested that the time associated with inelastic scattering of electrons from two-level-tunneling modes has this temperature dependence (Thouless, 1980), but there is no a priori reason to expect that this mechanism is present in these systems. Furthermore, the electron-tunneling-mode scattering time estimated by Black et al. (1979) using experimental data for the metallic glass, PdSiCu, is more than two orders of magnitude too large to explain the data.

It should be noted that Chaudhari, Broers, Chi, Laibowitz, Spiller, and Viggiano (1980) reached the opposite conclusion, namely that localization, not interaction, was the dominant mechanism. This inference was based on measurements of the differential resistance of phase-slip centers below the superconducting transition temperature of their WRe samples. This differential resistance provides an estimate of the charge-imbalance relaxation length, Λ_Q (Skocpol, Beasley, and Tinkham, 1974; Skocpol, Kadin, and Tinkham, 1978). From this, Chaudhari et al. (1980) inferred a value for the inelastic diffusion length, Λ_E, which was consistent with the value required to fit the resistance-increase data. Two remarks can be made: (1) Chaudhari et al. (1980) comment that their data in fact "agree quantitatively with the Coulomb interaction theory", so there is no disagreement with us on that point. (2) Their published phase-slip data were taken at rather high voltages (0.3 to 2 mV), where non-linear effects of heating and charge imbalance would be expected to significantly distort the data.

For example, strong gap depression near the site of the phase-slip
center would introduce a gap-gradient charge relaxation mechanism which
is not related to the inelastic relaxation rate that enters in Λ_E. We
speculate that the agreement between the phase-slip data and the
resistance-rise data noted by Chaudhari et al. (1980) could be explained
equally well by assuming that both are determined by a length related to
ζ_N as by a length related to Λ_E. In any case, caution is in order
in interpreting these observations, in view of the fact that not only
the WRe data but also the data on all other systems studied to date
apart from that of Sacharoff et al. (1982b), appear to be consistent
with the interaction model.

In conclusion, then, the Coulomb interaction model is found to give
an excellent fit to our best data (on copper). Moreover, it gives an
acceptable fit (within a factor of ~2) to the data obtained by three
groups on the low temperature resistance rise in wires made of five
metals with resistivities varying over more than two orders of magnitude
and widely varying electronic densities of states. This indicates that
the interaction model can account for the bulk of the observed effect in
these samples, while the localization model does not provide as natural
an explanation for the accurately determined magnitude and $T^{-1/2}$
temperature dependence of the data using current models of inelastic
scattering processes in one-dimensional samples (Abrahams et al., 1981).
In addition, we can explain the failure to see a low temperature
resistance minimum in bismuth whiskers and suggest an explanation for
the anomalously large low temperature resistance rise observed in drawn
platinum wires.

CHAPTER SIX: SUMMARY

We have made low temperature resistance measurements on ultrathin wires of copper, nickel, and AuPd alloy to study electronic conduction in disordered one-dimensional metals. Two models for conduction in these systems have been proposed. The electron localization model, first discussed by Anderson (1958) and extended to one dimension by Thouless (1977), is an independent electron theory. It predicts a rising resistance at low temperatures with a temperature dependence that is determined by the dominant inelastic scattering mechanism, which is not well known. Alternatively, the electron-electron interaction model of Altshuler, Khmel'nitzkii, Larkin, and Lee (1980b) is a many-body theory which involves no mechanism-dependent parameters. It also predicts a resistance rising at low temperatures, this time as $T^{-1/2}$.

The ultrathin wires that were used for this study had cross-sectional dimensions as small as 220Å x 200Å and were fabricated using a step-edge shadowing technique. The thickness of the wires was thus determined by the RIE depth, and the width of the wires was controlled by the depth of the evaporated metal film and the angle of evaporation. By anisotropically etching the silicon substrate under the wires, we were able to prepare the samples for observation in a high resolution TEM. Using the same procedure, we made blank SiO_2 membranes and evaporated thin metal films onto them in order to study the grain size and overall quality of the films in a TEM.

In general, we observe a minimum in the resistance vs. temperature curves, R(T), of our samples at $\sim 10^{\circ}$K. This can be understood as the sum of the contributions from three different effects: the normal, high temperature resistance rise due to the increasing density of phonons, the temperature-independent bulk residual resistance which is due to impurities or lattice defects, and a low temperature resistanc rise which depends on the cross-sectional area of the sample and is due to electron localization or electron-electron interaction effects. A detailed analysis of the low temperature resistance rise in our wire samples showed a $T^{-1/2}$ temperature dependence and an absolute magnitude for $\Delta R/R$ that were remarkably consistent with the predictions of the electron-electron interaction model. This led us to reexamine the data on similar samples in the published literature, which had been previously interpreted in terms of the most recent localization model of Thouless (1980). As a result, we concluded that the interaction model can account for all of the observed effect in our copper samples and for most of the observed effect in all one-dimensional lithographically-produced samples reported to date. However, especially in high resistivity samples where the interaction model is no longer valid, we cannot rule out the presence of localization effects.

Although we have shown that interaction effects are important in one-dimensional conductors, a detailed picture of the relation between interaction effects and localization effects is not yet possible. In particular, we do not know if these effects are simply additive or if the nature of the electron-electron interactions changes in the strongly

localized regime ($k_F l \ll 1$). Measurements of other physical quantities
might help to separate the contributions from the two effects in various
regimes. For example, tunneling experiments on clean one-dimensional
conductors should show a dip in the density of states at the Fermi level
as predicted by the interaction model, while the same measurements on
dirty conductors might not show a change in the density of states.
Magnetoresistance measurements might be able distinguish between the two
effects, but preliminary measurements of our copper samples in a small
(<10kG) magnetic field showed little field dependence. In this case,
noise problems prevented us from taking quantitative data, but if this
experiment could be repeated at higher fields and in a quieter
environment, one might have hope of learning something. Hall effect
measurements might also be able to distinguish between the two effects,
but these would be technologically difficult.

Another tack to take in verifying the relative importance of the
two effects is to independently determine $\widetilde{G}_{in}$, as was attempted by
Chaudhari and coworkers (1980). This has already been done in two
dimensions by analyzing magnetoresistance data from Si MOSFETs (Dynes,
1982). In addition, by systematically varying the cross-sectional
dimensions in a set of wires, one might observe cross-over behavior from
one to two dimensions, perhaps providing a clue about the relevant
length scale.

Although our measurements on nickel wires showed that magnetic
field effects dominated interaction effects at low fields, it would be
interesting to investigate the interplay between these two effects in

more detail. A possible approach to this problem is to add small amounts of copper to the nickel in order to suppress the ferromagnetism of the nickel. Similarly, it would be interesting to study the relation between interaction effects and superconductivity near the superconducting transition of a material.

The fabrication techniques that we have developed are versatile enough to explore many of these ideas. Using the shadowing technique, ultrathin wires can be formed from any metal that can be evaporated, including the high T_c A-15 superconductors. Furthermore, samples made on silicon substrates can be thinned for observation in a TEM, enabling one to characterize them extremely well. It might even be feasible to completely remove the substrate from under a small section of a wire. This suggests the possibility of doing noise measurements on such samples to study the importance of the substrate and of boundary scattering on 1/f noise.

In summary, we hope that this project will stimulate further work in the field of conduction in lower-dimensionality samples, and that we have provided a solid technological base for such work.

Appendix A: Substrate Cleaning Procedure

Before any microstructure fabrication is attempted, the substrates must be free of all organic and particulate contamination. The cleaning procedure that we used is outlined here:

1. Immerse for 10 min. in trichloroethylene (TCE).

2. Immerse for 10 min. in acetone.

3. Immerse for 10 min. in methanol.

4. Rinse in flowing de-ionized (DI) water.

5. Immerse in concentrated sulfuric acid (H_2SO_4) for 10 min.

6. Rinse in flowing DI water.

7. Ultrasonically agitate in a 0.14% solution of metal-free, nonionic Acationox detergent in DI water.

8. Rinse in flowing DI water.

9. Immerse in hot circulating particle-free DI water for 60 min.

These are explained in more detail below.

The first three steps in the cleaning procedure are solvent stages to dissolve any organic films on the substrate. TCE is an excellent solvent for most organic materials, but it leaves a residue on the

wafer. If the wafer is moved directly without drying into the acetone, the remaining TCE is dissolved. Acetone is notorious for leaving a particularly stubborn residue (which, once dried, resists dissolution in even acetone) so the still-wet wafer is moved immediately to a bath of methanol that dissolves the acetone and is miscible with water. Any additional organic and many inorganic contaminants are then removed by soaking in H_2SO_4, which is a strong oxidizing agent. After a thorough rinse in DI water, the substrate is ultrasonically agitated in the detergent solution. This serves to further eliminate organic films and also to dislodge particles (such as pieces of dust or pieces of metal) from the substrate surface. Another rinse in DI water to remove the detergent and a long soak in a flowing 18MΩ DI water bath complete the procedure. The latter has proved very effective in eliminating ionic impurities and is an excellent place for overnight storage for most substrates; however, it has been found that the DI water leaches ions out of some glass substrates.

We usually blow the substrates dry with filtered dry nitrogen gas. At this point, a good operational test for the presence of contamination on all substrates except silicon is to observe the water wetting angle, θ:
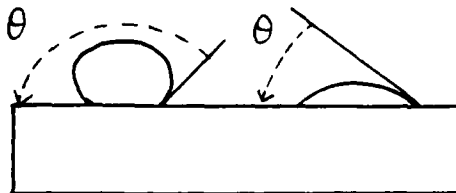
Since many organic films are hydrophobic, if θ is small, the surface is presumably clean.

Appendix B: Magnetoresistance of Nickel

This appendix contains a brief summary of the results of measurements on a set of nickel samples in a magnetic field. We are including them for completeness and also because they are potentially very interesting, but we have found them difficult to interpret.

The field-dependent resistance changes, $R(H)$, that we describe here are not directly related to the interaction effects which form the basis for this thesis. In particular, the magnetic effects occur at room temperature as well as at liquid helium temperature, with only a weak temperature dependence. In addition, it is hard to distinguish the behavior of the film from the behavior of the wires, although the magnitude of the resistance change and the saturation field seem to be generally larger in the film.

To illustrate the sort of behavior that we observed, in Figs. B.1 and B.2 we show data from a representative nickel sample in an applied magnetic field which is oriented parallel to the direction of current flow and perpendicular to the substrate, respectively. In both cases, there is a large suppressed zero on the resistance axis. We have defined ΔR for each of the orientations in such a way that it gives an indication of the magnitude of the resistance change caused by application of the field. H_{S1} and H_{S2} are the two saturation fields which are usually not equal because of the hysteresis. In Table B.1, we list the values of ΔR and H_{sat} (the arithmetic mean of $|H_{S1}|$ and H_{S2}) for the three nickel wire arrays and the 350Å nickel film at room
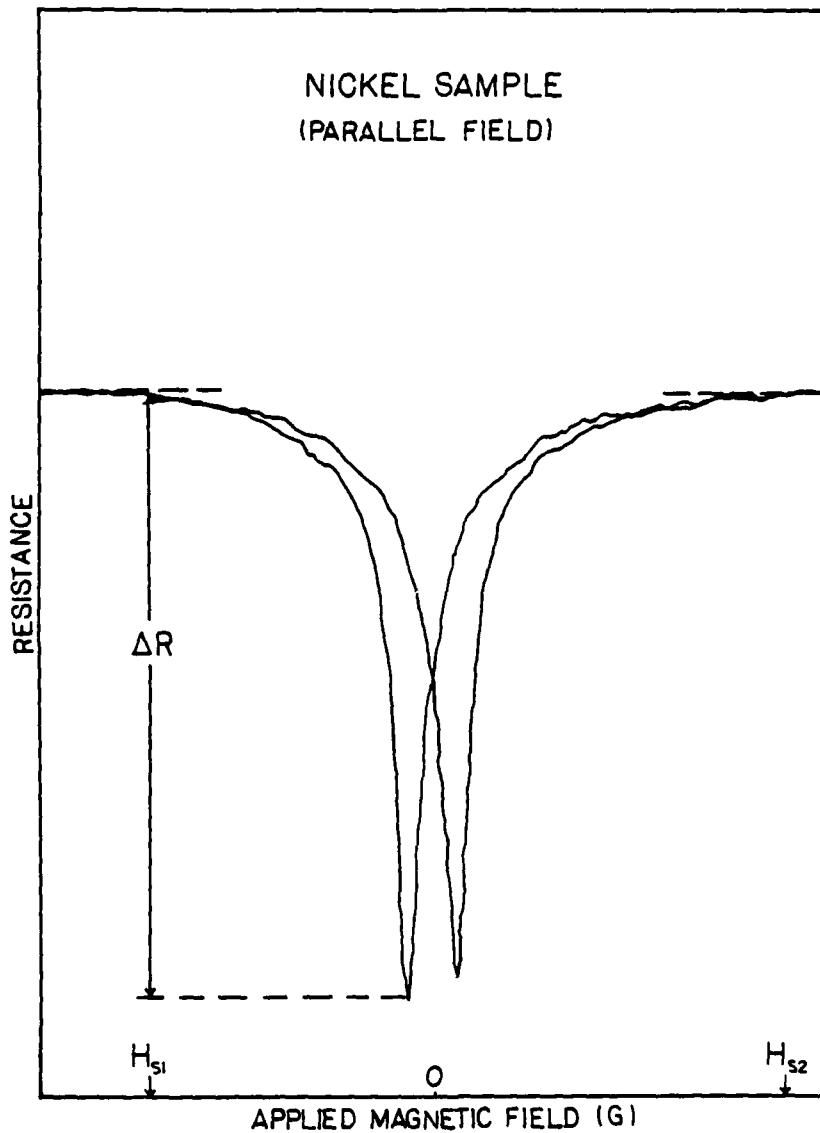
Fig. B.1: R(H) curve for a representative nickel sample in a magnetic field parallel to the direction of current flow, illustrating the meaning of ΔR, H_{S1}, and H_{S2} for this orientation. There is a suppressed zero on the resistance axis in this figure.
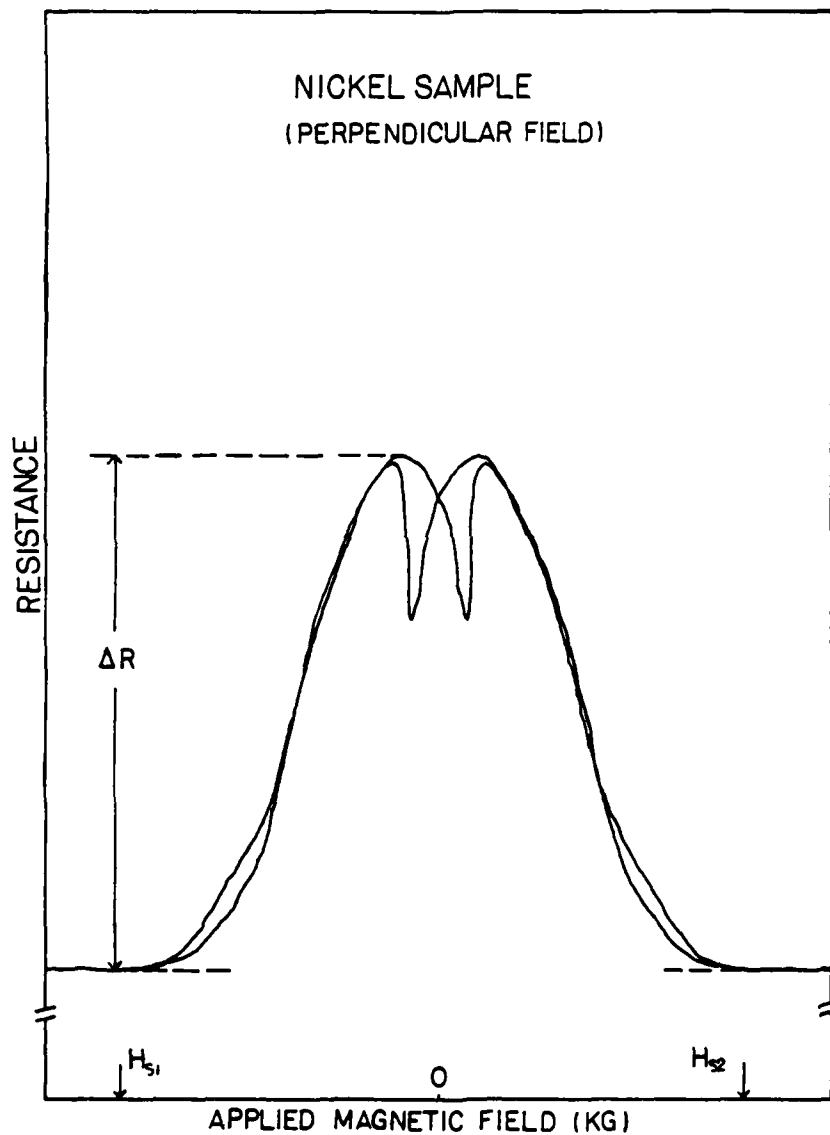
Fig. B.2: R(H) curve for a representative nickel sample in a magnetic field perpendicular to the plane of the substrate, defining ΔR, H_{S1}, and H_{S2} for this orientation. Again, there is a suppressed zero on the resistance axis.

Table B.1: Magnetoresistance of Nickel Samples

Summary of the data on the magnetoresistance, R(H), of 4 different nickel samples at 3 different temperatures. The "parallel" orientation of the magnetic field is parallel to the direction of current flow and the "perpendicular" orientation is normal to the plane of the substrate in all the samples. The definitions of the quantities tabulated here are illustrated in Figs. B.1 and B.2. $\Delta R/R$ gives an indication of how large a resistance change (relative to the total sample resistance) is caused by application of a magnetic field. H_{sat} is the arithmetic mean of $|H_{S1}|$ and H_{S2} and is included to show how large a field is required to saturate the magnetoresistance.

Temp.	Sample	parallel field		perpendicular field	
		H_{sat}(kG)	$|\Delta R|/R$	H_{sat}(kG)	$|\Delta R|/R$
~300°K	350Å film	1.00	1.58×10^{-3}	8.00	8.47×10^{-3}
	350Åx1000Å	no H dep.	0	1.65	1.38×10^{-2}
	350Åx500Å	no H dep.	0	2.35	1.35×10^{-2}
	350Åx250Å	no H dep.	0	3.7	9.31×10^{-3}
~77°K	350Å film	2.65	3.39×10^{-3}	5.95	7.41×10^{-3}
	350Åx1000Å	2.25	1.11×10^{-2}	1.00	4.41×10^{-3}
	350Åx500Å	2.1	2.8×10^{-3}	2.75	1.29×10^{-2}
	350Åx250Å	1.05	2.10×10^{-3}	3.20	7.81×10^{-3}
~4.2°K	350Å film	1.70	4.17×10^{-3}	6.05	6.78×10^{-3}
	350Åx1000Å	1.90	1.17×10^{-2}	0.38	2.74×10^{-3}
	350Åx500Å	3.00	3.73×10^{-3}	1.75	1.10×10^{-2}
	350Åx250Å	0.85	1.83×10^{-3}	2.05	8.05×10^{-3}

temperature (~300°K), liquid nitrogen temperature (~77°K), and liquid helium temperature (~4.2°K). Since the properties of these samples depend to a large extent on their magnetic history, it is complicated to find systematic trends in their behavior.

In general, ferromagnetic materials are expected to display a negative magnetoresistance due to suppression of spin fluctuations (Ueda, 1976). This was observed in our nickel samples in perpendicular fields (Fig. B.2) above ~200 gauss, but, at lower fields, an unexpected small positive magnetoresistance was observed. Even more puzzling was the parallel field behavior of our samples, where the samples exhibited a rising magnetoresistance up to a saturation value. Although single crystal nickel and polycrystalline nickel films which are evaporated in a magnetic field are known to display a magnetic anisotropy (Wako, Saheki, and Moriyama, 1963), it is hard to imagine that our films are oriented enough so that this magnetic anisotropy could account for the different sample behavior in perpendicular and parallel fields.

The hysteresis in the R(H) curves of all our nickel samples is reminiscent of the hysteresis in the induced magnetization (I) versus applied magnetic field (H) curves of a typical ferromagnet (shown in Fig. B.3). In fact, Ueda (1976) suggests that there is a complex relation between the magnetization and the magnetoresistance of a ferromagnetic metal. As manifested by the hysteresis in the R(H) curves, the remnant magnetization (I_R) in a sample depends on its (usually not well known) field history. Furthermore, an applied magnetic field (and, by inference, the remnant field) strongly
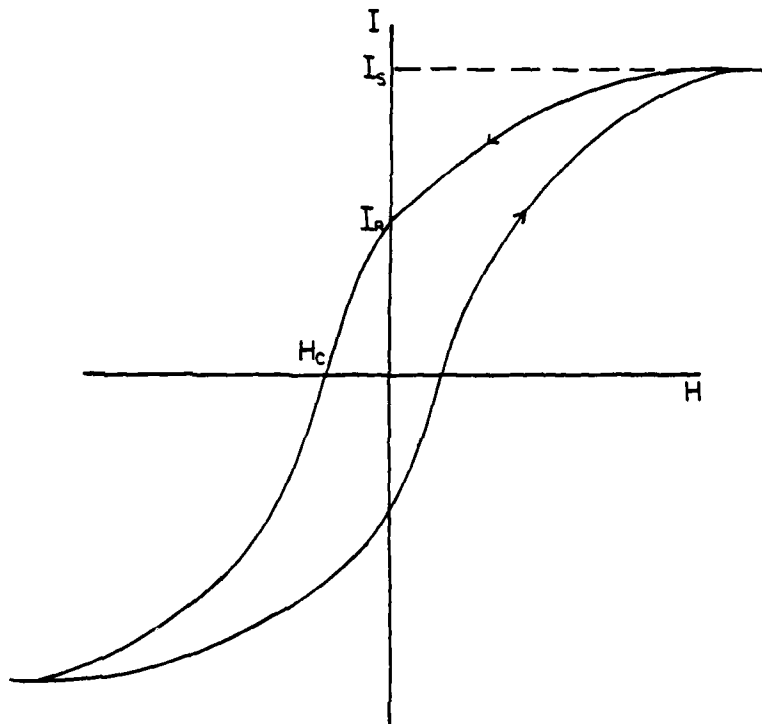
Fig. B.3: A schematic I/H or hysteresis loop for a ferromagnetic
material defining the following:

I_S = saturation magnetization

I_R = remnant magnetization

H_C = coercive field

(from Craik, 1971).

influences the R(T) behavior of the samples as shown in Fig. B.4, making measurements to search for interaction effects impractical.

In conclusion, we have observed interesting effects in the behavior of three nickel wire arrays and a nickel film in an applied magnetic field. Some of them can be attributed to the ferromagnetic properties of nickel, but much is unexplained. In particular, we are not sure to what extent the small dimensions of our samples influence their behavior in a magnetic field.
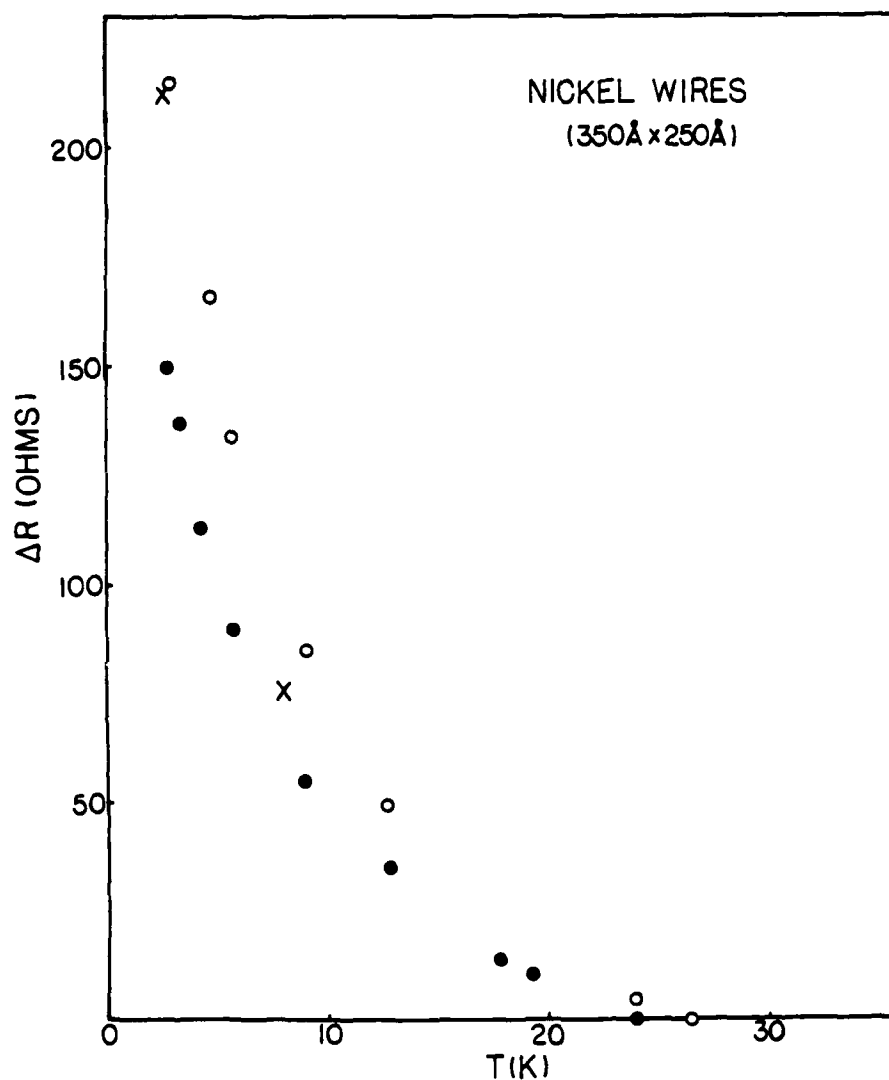
Fig. B.4: Data on the low-temperature resistance rise, R(T), in an
array of nickel wires showing the effect of an applied
magnetic field on the magnitude of the rise. The field was
oriented normal to the plane of the substrate and was varied
from 60 gauss (closed circles), to 500 gauss (open circles),
to 1652 gauss (crosses).

REFERENCES

Abrahams, E., P. W. Anderson, D. C. Licciardello, and
T. V. Ramakrishnan, 1979, Phys. Rev. Lett. 42, 673.

Abrahams, Elihu, and T. V. Ramakrishnan, 1980, J. Noncrys. Sol. 35, 15.

Abrahams, E., P. W. Anderson, P. A. Lee, and T. V. Ramakrishnan, 1981,
Phys. Rev. B24, 6783.

Altshuler, B. L., and A. G. Aronov, 1979, Zh. Eksp. Teor. Fiz. 77, 2028
[Sov. Phys.-JETP 50, 968].

Altshuler, B. L., A. G. Aronov, and P. A. Lee, 1980a,
Phys. Rev. Lett. 44, 1288.

Altshuler, B. L., D. Khmel'nitzkii, A. I. Larkin, and P. A. Lee, 1980b,
Phys. Rev. B22, 5142.

Anderson, A. C., and R. E. Peterson, 1970, Cryogenics 10, 430.

Anderson, P. W., 1958, Phys. Rev. 109, 1492.

Anderson, P. W., E. Abrahams, and T. V. Ramakrishnan, 1979, Phys. Rev.
Lett. 43, 718.

Anderson, P. W., D. J. Thouless, E. Abrahams, and D. S. Fisher, 1980,
Phys. Rev. B22, 3519.

Anderson, P. W., 1981, Phys. Rev. B23, 4828.

Ashcroft, Neil W., and N. David Mermin, 1976, Solid State Physics,
(Holt, Rinehart and Winston, New York).

Bean, K. E., 1978, IEEE Trans. Elec. Dev. ED-25, 1185.

Bevk, J., 1973, Phil. Mag. 28, 1379.

Bird, George R., and Maxfield Parrish, Jr., 1960, J. Opt. Soc. Am.
50, 886

Bishop, D. J., D. C. Tsui, and R. C. Dynes, 1980, Phys. Rev. Lett. 44,
1153.

Black, J. L., B. L. Gyorffy, and J. Jäckle, 1979, Phil. Mag. B40, 331.

Blatt, Frank J., 1968, Physics of Electronic Conduction in Metals,
(McGraw-Hill, New York).

Bradley, D. E., 1956, J. Appl. Phys. 27, 1399.

148

Chaudhari, P., and H.-U. Habermeier, 1980a, Phys. Rev. Lett. 44, 40.

Chaudhari, P., and H.-U. Habermeier, 1980b, Sol. St. Comm. 34, 687.

Chaudhari, P., A. N. Broers, C. C. Chi, R. Laibowitz, E. Spiller, and
    J. Viggiano, 1980, Phys. Rev. Lett. 45, 930.

Chopra, K. L., 1969, Thin Film Phenomena, (McGraw-Hill, New York).

Cochrane, R., R. Harris, J. Ström-Olson, and M. Zuckerman, 1975,
    Phys. Rev. Lett. 35, 676.

Craik, D. J., 1971, Structure and Properties of Magnetic
    Materials, (Pion Ltd., London).

Deutscher, G., H. Fenichel, M. Gershenson, E. Grunbaum, and Z. Ovadyahu,
    1973, J. Low Temp. Phys. 10, 231.

Dodson, B. W., W. L. McMillan, J. M. Mochel, and R. C. Dynes, 1981,
    Phys. Rev. Lett. 46, 46.

Dolan, G. J., and D. D. Osheroff, 1979, Phys. Rev. Lett. 43, 721.

Dynes, R. C., J. P. Garno, and J. M. Rowell, 1978, Phys. Rev.
    Lett. 44, 479.

Dynes, R. C., and J. P. Garno, 1981, Phys. Rev. Lett. 46, 137.

Dynes, R. C., 1982, Surf. Sci. 113, 685.

Edwards, L. R., C. W. Chen, and S. Legvold, 1970, Sol. St.
    Comm. 8, 1403.

Flanders, D. C., 1978, MIT Ph.D. thesis; published as Technical Report
    533, Lincoln Laboratory, MIT.

Flanders, D. C., 1979, J. Vac. Sci. Technol. 16, 1615.

Flanders, D. C., 1980, Appl. Phys. Lett. 36, 93.

Flanders, D. C. and Alice E. White, 1981, J. Vac. Sci.
    Technol. 19, 892.

Forster, D., 1975, Hydrodynamic Fluctuations, Broken Symmetry
    and Correlation Functions, (Benjamin, New York).

Fowler, A. B., F. F. Fang, W. E. Howard, and P. J. Stiles, 1966,
    Phys. Rev. Lett. 16, 901.

Fuchs, K., 1938, Proc. Camb. Phil. Soc. 34, 100.

Fukuyama, H., 1980, J. Phys. Soc. Jap. 49, 644.

Giordano, N., W. Gilson, and D. E. Prober, 1979, Phys. Rev. Lett. 43, 725.

Giordano, N., 1980, Phys. Rev. B22, 5635.

Giordano, N., Proc. Int. Conf. on Physics in One Dimension, edited by J. Bernasconi and T. Schneider, (Springer-Verlag, Berlin), p. 310.

Grimvall, G., 1976, Phys. Scr. 14, 63.

Herrod, R. A., and R. G. Goodrich, 1970, Phys. Lett. 33A, 331.

Ioffe, A. F., and A. R. Regel, 1960, Prog. Semiconductors 4, 237.

Ishii, K., 1973, Theor. Phys., Suppl. 53, 77.

Jansen, A. G. M., A. P. van Gelder, and P. Wyder, 1980, J. Phys. C 13, 6073.

Kahn, F. J., G. N. Taylor, and H. Schonhorn, 1973, Proc. IEEE 61, 823.

Kahn, F. J., 1973, Appl. Phys. Lett. 22, 386.

Kaplan, Steven B., 1979, J. Low Temp. Phys. 37, 343.

Kittel, C., 1971, Introduction to Solid State Physics, (Wiley, New York), 4th ed.

Knapp, G. S., and R. W. Jones, 1972, Phys. Rev. B6, 1761.

Knapp, G. S., R. W. Jones, and B. A. Loomis, 1974, Proc. of the 13th Int. Conf. on Low Temp. Phys. 3, edited by K. T. Timmerhaus, W. J. O'Sullivan, and E. F. Hammel, (Plenum, New York), p. 611.

Landauer, R., 1970, Phil. Mag. 21, 863.

Lee, P. A., 1981, lecture notes, unpublished.

Lehmann, H. W., and R. Widmer, 1978, Appl. Phys. Lett. 32, 163.

MacDonald, D. K. C., and K. Sarginson, 1950, Proc. Roy. Soc. A 203, 223.

Maissel, Leon I., and Reinhard Glang, 1970, Handbook of Thin Film Technology, (McGraw-Hill, New York).

Maldague, Pierre F., Phys. Rev. B23, 1719, sec. III.

Markiewicz, R. S., and L. A. Harris, 1981, Phys. Rev. Lett. 46, 1149.

Masden, J. T., and N. Giordano, 1981, Physica 107B, 3.

Montgomery, H., G. P. Pells, and E. M. Wray, 1967,
     Proc. Roy. Soc. (London) A301, 261.

Mott, N. F., 1949, Proc. Phys. Soc. A62, 416.

Mott, N. F., and W. D. Twose, 1961, Adv. Phys. 10, 107.

Mott, N. F., 1966, Phil. Mag. 13, 989.

Mott, N. F., 1974, Metal-Insulator Transitions, (Taylor and Francis,
     London).

Overcash, D. R., B. A. Ratnam, M. J. Skove, and E. P. Stillwell, 1980,
     Phys. Rev. Lett. 44, 1348.

Pliskin, W. A., and E. E. Conrad, 1964, IBM Jour. of Res. and Dev. 8,
     48.

Prange, Richard E., and Leo P. Kadanoff, Phys. Rev. 134, A566.

Raffy, H., R. B. Laibowitz, J. Graczyk, and P. Chaudhari, 1982, Bull. of
     the Am. Phys. Soc. 27, 161.

Rosenbaum, T. F., K. Andres, G. A. Thomas, and P. A. Lee,
     Phys. Rev. Lett. 46, 568.

Sacharoff, A. C., R. M. Westervelt, and J. Bevk, 1982a, Bull. of the
     Am. Phys. Soc. 27, 161.

Sacharoff, A. C., R. M. Westervelt, and J. Bevk, 1982b, submitted for
     publication.

Santhanam, P., 1981, unpublished.

Shapiro, Boris, and Elihu Abrahams, 1981, Phys. Rev. B24, 4889.

Skocpol, W. J., M. R. Beasley, and M. Tinkham, 1974, J. Low
     Temp. Phys. 16, 145.

Skocpol, W. J., A. M. Kadin, and M. Tinkham, 1978, Jour. de Phys. C6,
     1421.

Skocpol, W. J., L. D. Jackel, E. L. Hu, R. E. Howard, and L. A. Fetter,
     1982, submitted for publication.

Smith, Henry I., 1980, in Proceedings of Microcircuit Engineering '80,
     Amsterdam, 30 Sept. - 2 Oct., 1980.

Thouless, D. J., 1977, Phys. Rev. Lett. 39, 1167.

Thouless, D. J., 1980, Sol. St. Comm. $\underline{34}$, 683.

Tinkham, M., 1975, Introduction to Superconductivity, (McGraw-Hill, New York).

Tsuei, C. C., 1978, Sol. St. Comm. $\underline{27}$, 691.

Ueda, K., 1976, Sol. St. Comm. $\underline{19}$, 965.

Uren, M. J., R. A. Davies, and M. Pepper, 1980, J. Phys. C $\underline{13}$, L985.

Uren, M. J., R. A. Davies, M. Kaveh, and M. Pepper, 1980, J. Phys. C $\underline{14}$, L395.

Van den dries, L., C. Van Haesendonck, Y. Bruynseraede, and G. Deutscher, 1981, Phys. Rev. Lett. $\underline{46}$, 565.

Wako, T., M. ⁀heki, and T. Moriyama, 1963, Japan. J. Appl. Phys. $\underline{2}$, 584.

Wheeler, R. G., 1981, Phys. Rev. B$\underline{24}$, 4645.

White, Alice E., M. Tinkham, W. J. Skocpol, and D. C. Flanders, 1982, submitted for publication.

White, Guy K., 1979, Experimental Techniques in Low-Temperature Physics, (Clarendon Press, Oxford), 3rd ed.

Wigner, E., 1938, Trans. Farad. Soc. $\underline{34}$, 678.

Williams, Robley C., and Robert C. Backus, 1949, J. Appl. Phys. $\underline{20}$, 98.

ACKNOWLEDGEMENTS

During the course of my graduate work, I have benefited from my associations with many people. It is a pleasure to acknowledge their contributions here.

Even though I ended up doing a project that was somewhat tangential to the direction of the superconductivity group at Harvard, I am glad to have been a part of the tradition. I am especially grateful to my advisor, Prof. Tinkham, for his keen insights during all stages of this work and for his help in pulling things together over the past several months. In addition, Bill Skocpol has made many useful suggestions and has always been willing to discuss my work, even after his departure from Harvard.

The graduate students and post-doctoral assistants in the group, past and present, have been generous with their time, providing help with experimental problems and moral support when nothing else seemed to work. In particular, Chris Lobb and David Abraham both read early drafts of this manuscript and offered constructive criticism. Chris also gave me a lot of encouragement during my first two years of graduate school and David has always come through when I needed him. Fawwaz Habbal has shared his knowledge of magnetism with me and Juan Aponte has shared his technical expertise and his love of music. Greg Blonder's and Dave Frank's calm approaches to crises (especially of the computer variety) have also been a great asset.

Over the past three years, I have also had the opportunity to work in the submicrometer group at Lincoln Laboratory. Without the expert guidance of Dale Flanders and access to the facilities, this project would have been impossible. I am very grateful to Dale for introducing me to the field of microfabrication and for taking an active interest in my work.

The technical support both at Harvard and at Lincoln Laboratory has been outstanding. In particular, I thank Louis DeFeo for precise machining (even on short notice!), Dave Astolfi for help in all aspects of sample preparation, Lewis Stern for SEM work, Peter DeGraff for IBE, and Keith Krohn for RIE. All of these people somehow managed to squeeze my work orders into their busy schedules, and I've enjoyed sharing the lab with them.

Last, but definitely not least, I'd like to thank my whole family, especially my mother and father, for their constant love, moral support, and encouragement. They have helped me through the difficult times.

DISTRIBUTION LIST FOR ONR ELECTRONIC AND SOLID STATE SCIENCES

Director
Advanced Research Projects Agency
Attn: Technical Library
1400 Wilson Boulevard
Arlington, Virginia 22209

Office of Naval Research
Electronics Program Office (Code 427)
800 North Quincy Street
Arlington, Virginia 22217

Office of Naval Research
Code 105
800 North Quincy Street
Arlington, Virginia 22217

Director
Naval Research Laboratory
4555 Overlook Avenue, S.W.
Washington, D.C. 20375
Attn: Technical Library (6 cps)
Code 5200 (1 copy)
5210 (1 copy)
5270 (1 copy)
6400 (1 copy)

Office of the Director of Defense
Research and Engineering
Office of the Assistant Director
Electronics & Physical Sciences
The Pentagon, Room 3D1079
Washington, DC 20301

Defense Documentation Center (12 cps)
Cameron Station
Alexandria, Virginia 22314

Commanding Officer
Office of Naval Research Branch Office
536 South Clark Street
Chicago, Illinois 60605

San Francisco Area Office
Office of Naval Research
50 Fell Street
San Francisco, California 94102

Commanding Officer
Office of Naval Research Branch Office
1030 East Green Street
Pasadena, California 91101

Commanding Officer
Office of Naval Research Branch Office
495 Summer Street
Boston, Massachusetts 02210

New York Area Office
Office of Naval Research
115 Broadway 5th Floor
New York, New York 10003

ODDR&E Advisory Group on Electron Devices
201 Varick Street
New York, New York 10014

Naval Air Development Center
Attn: Technical Library
Johnsville
Warminster, Pennsylvania 18974

Naval Weapons Center
China Lake, California 93555
Attn: Technical Library (1 copy)
Code 6010 (1 copy)

Naval Research Laboratory
Underwater Sound Reference Division
Technical Library
P.O. Box 8337
Orlando, Florida 32806

Navy Underwater Sound Laboratory
Technical Library
Fort Trumbull
New London, Connecticut 06320

Commandant, Marine Corps
Scientific Advisor (Code AX)
Washington, D.C. 20380

Naval Ordnance Station
Technical Library
Indian Head, Maryland 20640

Naval Postgraduate School
Monterey, California 93940
Attn: Technical Library (1 copy)
Elect. Engin. Depart. (1 copy)

Naval Missile Center
Technical Library (Code 5632.2)
Point Mugu, California 93010

Naval Electronics Laboratory Center
San Diego, California
Attn: Technical Library (1 copy)
Code 2300 (1 copy)
2600 (1 copy)
4800 (1 copy)

Naval Undersea Center
Technical Library
San Diego, California 92132

Naval Weapons Laboratory
Technical Library
Dahlgren, Virginia 22448

Naval Ship Research and Development Center
Central Library (Codes L42 and L43)
Washington, D.C. 20007

Naval Surface Weapons Center
White Oak Laboratory
Silver Spring, Maryland 20910
Attn: Technical Library (1 copy)
Code 200 (1 copy)
212 (1 copy)

Deputy Chief of Naval Operations
(Development)
Technical Analysis and Advisory Group
(Code NOP-077D)
Washington, D.C. 20350

Commander
Naval Air Systems Command
Washington, D.C.
ATTN: Code 310 (1 copy)
360 (1 copy)

Commander
Naval Electronics Systems Command
Washington, D.C. 20360
Attn: Code 304 (1 copy)
310 (1 copy)

Commander
Naval Sea Systems Command
Washington, D.C. 20360

Naval Surface Weapons Center
Attn: Library
Dahlgren, Virginia 22448

Air Force Office of Scientific Research
Attn: Electronic and Solid State
Sciences Division
Department of the Air Force
Washington, D.C. 20333

Air Force Weapon Laboratory
Technical Library
Kirtland Air Force Base
Albuquerque, New Mexico 87117

Air Force Avionics Laboratory
Air Force Systems Command
Technical Library
Wright-Patterson Air Force Base
Dayton, Ohio 45433

Air Force Cambridge Research Laboratory
L.G. Hanscom Field
Technical Library
Cambridge, Massachusetts 02138

Harry Diamond Laboratories
Technical Library
Connecticut Avenue at Van Ness, N.W.
Washington, D.C. 20438

U.S. Army Research Office
Box CM, Duke Station
Durham, North Carolina 27706

Director
U.S. Army Engineering Research
and Development Laboratories
Fort Belvoir, Virginia 22060
Attn: Technical Documents Center

Director National Bureau of Standards
Attn: Technical Library
Washington, D.C. 20234

Naval Research Laboratory
4555 Overlook Avenue, S.W.
Washington, D.C. 20375
Attn: Code 5300 (1 copy)
7100 (1 copy)
7900 (1 copy)

Naval Electronics Laboratory Center
San Diego, California 92152
Attn: Code 2100 (1 copy)
2200 (1 copy)

C.C. Klick
Superintendent
Materials Sciences Division
Naval Research Laboratory
4555 Overlook Avenue, S.W.
Washington, D.C. 20375

Naval Research Laboratory
4555 Overlook Avenue, S.W.
Washington, D.C. 20375
Attn: Code 5220 (1 copy)
5230 (1 copy)
5250 (1 copy)
5260 (1 copy)
5270 (copy)
5500 (. copy.

Naval Electronics Laboratory Center
San Diego, California 92152
Attn: Code 2500 (1 copy)
4000 (1 copy)

Office of Naval Research (2 cps)
800 N. Quincy Street
Arlington, Virginia 22217
Attn: Code 430 (2 copies)

Naval Research Laboratory
4555 Overlook Avenue, S.W.
Washington, D.C. 20375
Attn: Code 5400

Naval Electronics Laboratory Center
San Diego, California 92152
Attn: Code 3000 (1 copy)
5000 (1 copy)
5600 (1 copy)

Air Force Office of Scientific Research
Mathematical and Information Sciences
Directorate
1400 Wilson Blvd.
Washington, D.C. 20333

N

DATE
ILME